UC San Diego
UC San Diego Electronic Theses and Dissertations

Title

From nano to micro: activity-driven self-organization of interphase chromatin

Permalink

https://escholarship.org/uc/item/6dm3s4m0

Author

Mahajan, Achal

Publication Date

2021

Peer reviewed|Thesis/dissertation

UNIVERSITY OF CALIFORNIA SAN DIEGO

From nano to micro: activity-driven self-organization of interphase chromatin

A dissertation submitted in partial satisfaction of the
requirements for the degree
Doctor of Philosophy

in

Engineering Sciences (Engineering Physics)

by

Achal Mahajan

Committee in charge:

Professor David Saintillan, Chair
Professor Elena F. Koslover
Professor Stephanie E. Lindsey
Professor Padmini Rangamani
Professor Douglas E. Smith

2021

The dissertation of Achal Mahajan is approved, and it is acceptable in quality and form for publication on microfilm and electronically.

University of California San Diego

2021

To my family, the science fraternity for their pursuit of truth and the people who lost their lives during the pandemic.

EPIGRAPH

There is grandeur in this view of life, with its several powers, having been originally breathed into a few forms or into one; and that, whilst this planet has gone cycling on according to the fixed law of gravity, from so simple a beginning endless forms most beautiful and most wonderful have been, and are being, evolved.

– Charles Darwin, The Origin of Species

TABLE OF CONTENTS

LIST OF FIGURES

ACKNOWLEDGEMENTS

This thesis not only represents the work on a computer but a five year long roller coaster ride filled with ups and downs. My experience at University of California of San Diego is perhaps nothing short of amazing. The stimulating environment to learn and grow both intellectually and philosophically has made me a responsible researcher. I welcome this opportunity to thank all those people who helped me in pursuing my dissertation with their valuable comments and ideas. I would like to express my special appreciation and thanks to my advisor Professor David Saintillan, who has been a tremendous mentor for me. He fostered my development both as a scientist giving me the full autonomy to ask fundamental questions on different research problems; and as an individual by showing me the way to always keep my curiosity alive. A great teacher himself, I learnt the art of conveying scientific ideas from him and imparting the knowledge as a fundamental responsibility of a scientist. Thank you for everything!.

I would also like to thank my committee members: Prof. Padmini Rangamani for mentoring and providing career advice whenever needed, Prof. Elena Koslover and Prof. Douglas Smith for giving the encouragement, sharing insightful suggestions, and critically questioning important aspects of the modeling. Special thanks to Prof. Juan Lasheras who was present during the initial phase of my dissertation committee and had a profound impact on all of us. Prof. Stephanie Lindsey for agreeing to serve on the committee at the last moment, and useful corrections for my thesis.

Welcome to sunny San Diego

As I moved to San Diego in pursuit of science and great weather, my first impression was that there is no way that you cannot fell love with this city. Met some of the brightest minds, get to experience a completely different culture and abundance of literally everything. This was my home away from home. When everything is almost ~ 15 mins

drive from you, how can you not feel excited but also fortunate at the same time. Even though I would love to take a dip in the ocean everyday, sometimes the season, most of the times its research would not let that happen. I joined the Saintillan lab in the fall of 2016, and had a wonderful experience largely due to the lab members. First, and foremost I would like to thank Brato Chakrabarti [1] for his friendship and help on research. The passion he carries for research is addictive and inspiring. If I had a list of people I admire on ethics, motivation and sheer curiosity, he would definitely make it in the top 5. Roberto for being the supportive labmate during the early phase of my thesis and numerous trips for dinners. I would also like to thank Hossein for being the sane one in the lab, and for all the fun lunch/dinner conversation. I will never forget the Persian tea, dessert and bread that you introduced me to. I would also like to thank Akhil, Arijit, Luca, Piyush, Tanumoy, Maxime, Antoine, Charles, Pedro, Yuzhu, and Deba for a cherished time spent together in the lab, and in social settings. All of you have contributed immensely to my personal and professional development at U.C. San Diego. Outside the research group, the biomechanics corridor space was kept alive by Ernesto, Gopesh, Aditya, Ashish, Jennifer.

Lastly, a support system can make a great difference for your mental and emotional health during the trying times. The wonderful folks in the dance group whom I had the chance to dance away my worries. Baffling to see so many people from different parts of the world connecting to the tune of music, and knows just one language, *Dance*. I tried learning different styles but nothing would match my love for "Bhangra", a traditional folk dance of Punjab. Nirjhar, Abhishek and Anay for making my everyday life infinitely better than it could be. San Diego would have been much rougher without you guys. Todd and Sam for hosting all the fun game nights, coffee conversations on modern science: its flaws and beauty in it's entirety. I cannot mention everyone here but I am extremely

---

[1]Credits to you for introducing me to this long form of acknowledgment. It takes time but I think its worth the effort.

Namma Bengaluru

Before my journey began to the west in pursuit of scientific knowledge, I spent three years in Bengaluru for my masters. The time I spent there was the most influential in

developing my scientific curiosity and temperament. I also realised the sheer importance of staying physically active, and taking care of your health. I picked up habits of exercising everyday and found my lost love for basketball which to this day is still alive. I had the opportunity to interact with some of the best intellectual minds both in and out of lab. I still miss the breadth of conversation we use to have over long coffee breaks and lunches. I will always cherish the wonderful memories that I had with Aditya, Manjeet and Raaghesh. From long hikes to long drives, the sudden plans and squeezing time in a busy schedule, the stories are never ending. I wish I had the inner zen of you, Adma! A shout to the EMU family especially Ronak, TSunil, Nakul, Sankalp and Kanwar for keeping me sane through the tough pandemic via long sessions of video calls and supporting my failed idea of starting a podcast. The number of times I have asked Ronak to proofread every article that I have written is uncountable. Thank you for being so patient, and providing me with an honest feedback. A simple phrase, "thank you", cannot present how much their friendship means to me. This place is also special because this is where I met Jigyasa (please refer to *Finally, the family* for more details).

Where it all started, NITK Surathkal

I can never forget my buddies from NITK Surathkal whom I had the chance to reconnect during the pandemic. Special thanks to Shubhashish, Mayur, Newton and Ritesh for their mental support and stimulating conversations. Thank you for lending me your ears to listen to my consistent rants, and venting out frustration especially during the job search. Because of you guys, I am better at my geography than I was before. I also want to recognize the impact of Prof. Sreekumar (NITK) on my life. His three years of teaching and mentoring shone the first glance of research and sustainabile living that has led to where I am. He will always be a source of inspiration to me in my pursuit to have even a minuscule (perhaps profound) impact on the community through my work,

and optimal use of finite resources.

All heroes don't wear capes

This section is for all the anonymous dark knights or the true heroes who were there in comments, and discussions on numerous QnA websites like stack-overflow and stack-exchange. Providing wisdom without any reward and making life easier for the people whom they have never met. It always boggles my mind that there is a solution to almost every small problem that I had faced, and someone was kind enough to post it. Also, a big shout out to all the open source developers involved in python, octave and inkscape for making my life a tad bit easier.

As they say PhD is a tough gamble. There are a lot at stakes. Sometimes the stress can be hard to handle, sometimes the excitement too. I owe a lot to the people at UCSD Counseling and Psychological Services (CAPS). I want to really call out to someone who is reading this and probably going through a rough phase, lease take care of your mental health, nothing is and nothing will be more important than your happiness. I know it's underrated but please do it. Now enough of sentiments, I would like to express my sincere gratitude to the people at CAPS who helped me through the difficult times. Thankful to Julie Colene Badaracco for being there on zoom calls throughout the pandemic.

Finally, the family

I thank my family for their support who never questioned my ability and pursuit of knowledge. Words cannot express how grateful I am to my mother (Neeru), sister (Shavi) and father (Chander Mohan) for all of the sacrifices that they have made on my behalf. Both my parents' struggles and values they uphold, have made me into the person I am.

A special thanks to Jigyasa who has been my mentor, my therapist, and for her support even though she was managing her own thesis experiments. "Kaise kar lete ho aap".

Thanks to her unconditional love and presence, I have been able to cruise through my good and bad times. These past several years have not been an easy ride, both academically and personally. I truly thank her for sticking by my side, and instilling confidence in me. I feel that what we both learned a lot about life and hope to live it to the fullest.

Last but not the least

As they say we are an average of 5 most influential people in our life. In my case there were 100. Listing out each one of them would take pages. I am grateful to all of them. I hope this brings smile to everyone's face who were rooting for my success since the beginning, and I hope to use whatever I have gained for the improvement of the society and its people. This is only way I can give back to everyone who is struggling out there in one form or the other. Cheers to new beginnings!

This dissertation is a collection of multiple problems borrowed in large parts, as listed below, from published or prepared manuscripts.

- Chapter 3 is largely based on the material that is submitted to Physical Review E. (2021), authored by Achal Mahajan and David Saintillan. The dissertation author was the primary researcher and author of this work.

- Chapter 4 is largely based on the material that is submitted to Physical Review X (2021), authored by Achal Mahajan, Wen Yan, Alexandra Zidovska, David Saintillan and Michael J. Shelley. The dissertation author was the primary researcher and author of this paper.

- Chapter 5 in part is a manuscript in preparation authored by Achal Mahajan, Luca Scotzniovsky, Michael J. Shelley and David Saintillan. The dissertation author was the primary researcher and author of this paper.

VITA

2013	B.Tech in Chemical Engineering National Institute of Technology Karnataka, Surathkal (India)
2016	M. S. (Engg.) in Engineering Mechanics Jawaharlal Nehru Center for Advanced Scientific Research, Karnataka (India)
2021	PhD in Engineering Sciences (Engineering Physics) University of California San Diego

ABSTRACT OF THE DISSERTATION

From nano to micro: activity-driven self-organization of interphase chromatin

by

Achal Mahajan

Doctor of Philosophy in Engineering Sciences (Engineering Physics)

University of California San Diego, 2021

Professor David Saintillan, Chair

The central theme of the dissertation is to understand physical principles underlying the dynamical self-organization of the genome in the cell across different length and time scales. The inherently multiscale and out-of equilibrium nature of chromatin dynamics and compaction in the strongly heterogeneous nucleus has been addressed in this work. The large-scale organization of chromatin – the functional form of DNA – is critical to transcription during which ATP-powered enzymes such as RNA polymerases must physically access specific genes within a tightly-packed, micron-scale nucleus. In differentiated cell nuclei, two major chromatin compartments – heterochromatin and euchromatin – are spatially segregated, with transcriptionally active euchromatin loosely packed while mostly silent genes are compacted into heterochromatin. Through the lens of an active

polymer model of chromosomes using Brownian dynamics simulations based on a boundary integral formulation, along with a kernel-independent fast multipole method, we investigate how large heterochromatic regions form and segregate through complex interactions with euchromatin. Our model consists of a system of long flexible bead-spring polymers representing chromosomes, which are confined to a spheroidal nucleus and composed of alternating segments of active euchromatin and silent heterochromatin immersed in a viscous solvent. Our simulations are applied to analyze the role of euchromatic activity on nuclear dynamics and pattern formation, and demonstrate that active stresses and resulting nucleoplasmic flows serve to enhance heterochromatin segregation and compaction by promoting interactions and subsequent crosslinking between distant genomic segments.

Moving to nano-scale organization, we also analyzed the dynamics of DNA loop extrusion in the presence of the active motor proteins known as structural maintenance of chromosomes (SMC) complexes, of which condensin and cohesin are two important examples. These complexes have been observed to translocate along chromatin in a force-dependent directed manner to form loops via a process known as "loop extrusion" using the energy obtained from the hydrolysis of ATP. In this work, we elucidated the role played by hydrodynamic interactions, the active response of the motors and chain mechanics in assisting loop extrusion under different parameter regimes. The model accounts for the structural features and dynamics of the motor proteins. Futhermore, studies with active polymer in an unconfined environment elucidated the role of activity and hydrodynamics in the self induced coil-stretch transition. This 'active coil–stretch transition' is reminiscent of the transition exhibited by passive flexible polymers in externally applied extensional flows, but is internally driven by dipolar activity in the present case. Discussions of the simulation findings are complemented with a simple kinetic model for an active trimer. Our modeling efforts complemented and informed some of the experimental observations

providing deeper insight into the mechanisms behind the genome organization.

Chapter 1

Introduction

The first sequence of human genome, completed in 2003 under the human genome project, uncovered the genetic building blocks of human genome, and opened up the doors for what some predicted would be the 'century of biology' [1]. Specifically, a DNA molecule consists of two polynucleotide strands (or chains) wounded in the shape of a double-helix. Each nucleotide sequence is made of a sugar and one of the four bases: adenine (A), thymine (T), guanine (G) and cytosine (C). The sugars are bound together by covalently bonds and form the DNA "backbone". In addition, the two strands are held together by hydrogen bonds between the bases on the different strands, resulting in a double-helical structure. At the heart of the entire sequence is the pair complementarity of each base: A with T and G with C. The complete sequence of base pairs determines the genetic information of each individual or species. It is called the genome. The corresponding sequence of letters is enormous. For instance, in the *Escherichia coli* bacterium, it contains 4.6×10^6 letters, and more than 3.3×10^9 in humans. Besides, specific DNA sequences, the genes, are encountered in the genome. Their number ranges from less than a hundred in simple bacteria to several tens of thousands in higher organisms. For example, approximately 4600 genes are found in *E. coli* and more than $30,000$ in humans. The genes

encode macromolecules such as ribonucleic acids (RNA), or polypeptides which are chains of amino-acids more commonly known as proteins. [2]. Painstakingly cataloguing the basic constituents of our DNA ('genome sequencing') took ten years, over three billion dollars and was a highly collaborative endeavor. Since then, we have been able to reduce the cost so much that by 2020 it is possible to explore the 20,000 or so human genes for under $1000, in a matter of hours to days. Imagine genes as sentences and genomes as entire books consisting of tens of thousands of chain of words. There have been estimates that between 100 million and as many as 2 billion human genomes could be sequenced by 2025, representing four to five orders of magnitude growth. Aberrant epigenetic modifications of genome and consequent changes in DNA binding and expression may lead to many long term diseases including diabetes, hypertension, coronary heart disease and genetic disorders [3]. Biological systems such as the one described above are notoriously known for their complexity and quantitative understanding of it requires fundamental equations from first principles similar to Newton's laws of motion that holds true even for interplanetary motions. While it is true that all biological processes result from the superimposition of many processes abiding by the laws of physics, the resulting system can be of a daunting complexity. Added to that is that vast separation in length and time scales between the two limits of single-molecule biophysics at the resolution of few nanometers to micron scale whole-cell dynamics which has historically hindered formation of mechanistic connections between atomistic-scale processes and whole-cell functions.

Nonetheless, a strategy to increase our understanding of chromatin biology and still retain a reasonable amount of complexity is to resort to biophysical modeling and computational approaches using ideas from polymer physics and hydrodynamics. Even then, it is not possible in general to perform simulations at the atomic resolution and produce trajectories corresponding to time scales compatible with biological time scales (of the order

of seconds). Instead, coarse-grained approaches are preferred where emergent phenomena and structures occur on length and timescales many orders of magnitude larger than those pertaining to their constituent atoms. This simplification results in drastically decreasing the degrees of freedom and has been extremely successful in predicting the dynamical behavior of different biological systems. Polymer physics and statistical mechanics have proven to be successful in capturing genome phase separation where polymer simulations shows segregation of compartments in which regions of the same type attract each other. These simulations successfully reproduced the checkerboard pattern that were observed in a type of chromosome configuration capture (Hi-C) experiments [4–6]. From equilibrium polymers perspective, Spakowitz and co-workers have successfully integrated polymeric forces into their models to demonstrate the dynamic coupling between chromosomal loci [7], diffusion of DNA-binding proteins to target sites [8], and chromatin segregation due to epigenetic modifications [5]. The importance of hydrodynamic or solvent-mediated interactions, which are neglected in the Brownian dynamics studies above, have been shown in a number of intracellular processes. Specifically, Saintillan et. al. developed a computational model of active chromatin hydrodynamics that accounts for the role of ATP-driven processes [9]. The force exerted by the motor proteins which were modeled as force dipoles generated fluid flows in the nucleoplasm, which in turn drove local nematic alignment of the chain resulting in large-scale coherent motions. Similarly, Shelley and co-workers have shown that hydrodynamic interactions in membrane confinement of cells plays a crucial role in the positioning of the mitotic spindle via different force transduction mechanisms that produce distinct intracellular flow profiles. From those observations one can infer that these flows exert influence on the dynamics at the cellular and sub-cellular level [10, 11]. Other microscopic phenomena where the flow is critical to whole-cell-scale function, as evidenced by the phenomenon of cytpolasmic streaming in cells first charac-

3

terized by Goldstein et. al. [12,13].

A key aspect of all the above examples is the mechanical coupling between the bio-polymer (DNA/chromatin) and the surrounding solvent incorporating motor induced microscopic forces in describing the emergent behavior. This central idea is explored in all the problems presented in this thesis in the spirit of pointing out the systematic links between first principle physics (including physical laws such as conservation of mass, momentum and energy), and first principles biology (including the central dogma, natural selection, and homeostasis). This thesis is an effort to develop such an approach borrowing ideas from soft-matter, biological physics and hydrodynamics in the low-Reynolds-number regime to address a collection of problems related to **chromatin dynamics** across a wide range of size and time scales. The rest of this chapter outlines the foundational principles which will be recurrent themes throughout the work. We will start with a multiscale tour of the genome followed by foundational principles of Stokes flow and briefly review Brownian motion. In the next chapter, we will delve into the detailed hydrodynamic framework using polymer dynamics and the boundary integral formulation. We will also explore some of the existing biophysical models of chromatin.

1.1 Chromatin dynamics and organization

Eukaryotic genomes are organized via several ubiquitous architectural features as shown in figure 1.1. The basic organizational elements of the genome are the fibers, loops, domains, and compartments that chromatin forms, as well as chromosomes. These features organize genomes at multiple levels and length scales. The chromatin fiber is made up of units of 146 base pairs (bp) of **DNA** wrapped around octamer histone proteins to form a bead-on-a-string like structure known as **nucleosomes**. These polymers are folded inside nuclei five to six orders of magnitude smaller than their linear length, and many facets

of this folding correlate with or are causally related to transcription and other cellular functions.

The DNA double helix has a diameter of $\sim$ 2 nm, and in human cells, its total length if stretched out would be $\sim$ 2 m, but it is folded inside a nucleus $\sim$ 10 μm in diameter, roughly five orders of magnitude smaller [14]. Despite this tight folding, the genome needs to remain accessible to key biological processes, including DNA replication and gene expression. How genome architecture and biological processes intertwine has puzzled generations of biologists, and a more comprehensive picture of the key determinants of these interactions is just starting to be unraveled. The DNA double helix contains approximately three base pairs per nanometer of length and has a persistence length of $\sim$ 50 nm, i.e., 150 bp, as estimated in in vitro experiments [15]. The first level of genome folding is achieved by nucleosomes, histone octamers which are short cylinders of 10 nm diameter and 5 nm in height. Despite the comparable persistence length at this scale, 147 bp of DNA wrap around each nucleosome, taking 1.7 turns. The electrostatic interaction between positively charged histones and negatively charged DNA forces the above compaction. Nucleosomes are spaced by 20-40 bp of linker DNA, such that a stretched array of nucleosomes appears as beads on a string in electron micrographs. Nucleosomes are dynamic and can be repositioned by ATP-dependent chromatin remodelers which have been captured by several equilibrium and nonequilibrium models [16–18]. Unfortunately, modeling at the length scale of individual nucleosomes to understand bulk or global dynamics can be computationally expensive. Therefore, a more coarse grained approach is required to make some progress. The further arrangement of nucleosomes into $\sim$ 30 nm higher chromatin fiber has come under a lot of controversy as this characteristic structure has not been confirmed in vivo [19–21]. Recent 3D high resolution electron microscopy (EM) data [22] revealed a more complex and irregular folding of the DNA, without 30-nm

fiber but with various diameters ranging from 5 nm to 24 nm.
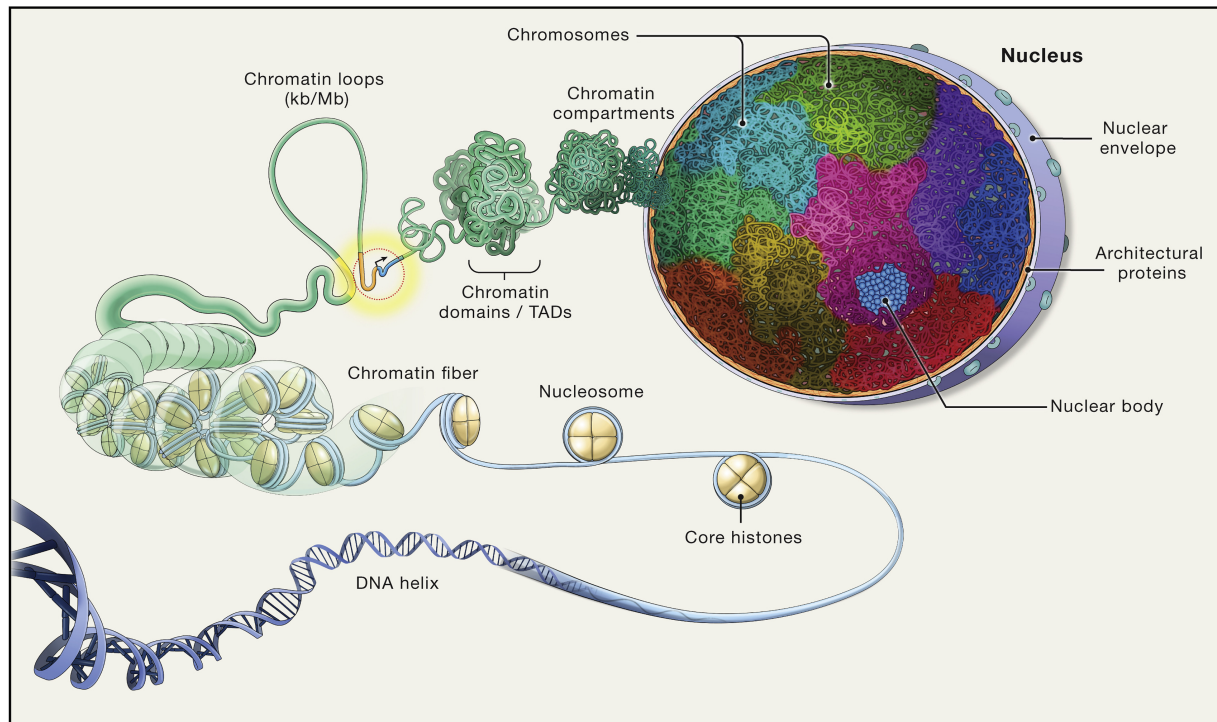
Figure 1.1: Figure shows the organization of genomes at different scales. DNA is wrapped around octamer of core-histones, forming the chromatin fiber which folds into loops, often bringing upstream gene regulatory elements (yellow), such as enhancers, into proximity to promoters of genes (gold/blue) to control their transcription (black arrow). The fiber then folds into chromatin domains, referred to as TADs, which associate with each other to create chromatin compartments. The DNA of each chromosome occupies a distinct volume, or chromosome territory (multiple colors), within the cell nucleus, generating non-random patterns of chromosome and genes. In the DNA-free space, the nucleus also contains RNA and proteinaceous protein aggregates which form nuclear bodies (blue). Image borrowed from [23].

While EM and light microscopy have allowed insights into the structure of chromatin and chromosomes at small (nuclesome-level) and large (nuclear) scales, intermediate scales were made accessible by Hi-C. It provided information that intrachromosomal contact frequency matrices display squared blocks of higher frequency along the diagonal, reflecting regions within which contacts occur more frequently than with any other parts

of the genome, and where the average contact frequencies decay slower than genome-wide averages [24,25]. These domains are called **topologically associated domains (TADs)** with a median size of ~ 200 kb in human cells. Another prominent feature uncovered by Hi-C are chromatin **loops** shown as peaks in the contact maps with enhanced frequency of interactions. A large fraction of TADs have such peaks at their corners and conversely, many loops are associated with TADs [26]. A simplest mechanism that can explain the contacts between distant sites is due to random collisions occurring from Brownian thermal fluctuations most of which will be short lived. However, if two colliding loci are bound by molecular motors that can form longer-lived interactions, these will stabilize contacts and create local peaks in the Hi-C maps. The TAD boundaries are also strongly enriched in specific proteins like CTCF and cohesin. The random collision model also fails to explain the strong correlation of TAD boundaries with converging CTCF sites, i.e., motifs oriented towards each other, while the three possible orientations of these motifs are strongly disfavored. A notable mechanism that has gained a lot attraction in recent years is the loop extrusion [26–31]. In this model, loop extruding factors (LEFs), which come under the family of structural maintenance of chromosome (SMC) complexes, bind to the chromatin (or DNA) fiber and actively pull out (extrude) the DNA until they unbind (or stall) or encounter the boundaries marked by CTCF bound sites or other cohesin complexes. The Langevin simulations considering a simple model of DNA as a linear polymer with active extrusion mechanism of the motor based on the experimentally obtained parameters were successful at explaining most of the experimental evidence as well as several experimental perturbations. While some models assume extrusion as an active ATP driven mechanism of SMC complexes as molecular motors [28,31], others propose extrusion without activity, powered by either transcriptionally induced supercoiling and thermal fluctuations [32,33]. An important experimental evidence in favor of the active extrusion model comes from

in vitro single-molecule imaging experiments showing that these specialised protein complexes can translocate on DNA [34–37] and bypass single nucleosomes and DNA-bound proteins, but not CTCF [38]. The dynamic nature of loops is also supported by single-molecule tracking of cohesin and CTCF in vivo [39]. The TADs and the associated domains is highly conserved across different cell types and species and therefore must play a crucial role in several biological processes. In terms of gene expression, alterations of TADs can lead to abnormal expression patterns. For instance, disruption of a single TAD boundary in mice leads to polydactyly, a severe developmental malformation [40]. Similarly, the loss of CTCF at a TAD boundary in patient-derived cells was shown to cause hyperactviation of an oncogene's expression, resulting in cell proliferation [41]. TADs have also been shown to affect replication where TADs have been shown to perfectly coincide with replication domains. DNA polymerases initiate replication in parallel at multiple locis along the length of the chromosome, leading to replication domains [42].

EM images have also unraveled the presence of highly dense, transcriptionally silent heterochromatic regions near the nuclear envelope and surrounding the nucleoli, with less compact, highly active euchromatin at the center of the nucleus with some exceptions of retinal cells of nocturnal mammals, which display an inverted architecture [6, 43]. The partition of the domains based on their activity appears as checkerboard pattern on the Hi-C maps [44]. This pattern based on eigen vector analysis suggests that the entire genome is partitioned in alternating regions of a few megabases belonging to **compartments (A and B)**. Comparison with ChIP-Seq (chromatin immunoprecipitation and sequencing) data shows a strong correlation of A regions with transcriptionally active histone markers and decondensed chromatin, while B regions correlate with inactive histone marks and dense regions. The biochemical basis of heterochromatin condensation is understood to be linked to the methylation of histone tails and binding of heterochromatin protein 1

(HP1) to nucleosomes. Bound HP1 further oligomerizes and bridges nucleosomes from chromatin regions in close spatial proximity, resulting in the compaction and repression of silent genes [5, 45–49]. This compaction has also been hypothesized to involve liquid–liquid phase separation by HP1 [50, 51]. In recent studies, chromosomes were modeled as block heteropolymers divided into three compartments (A, B and C). The simulations recovered the inverted nuclear architecture as well as the compartment organization by assigning same attractive interactions between different types of monomers depending on the chromatin type [6]. Subsequent studies based on the same models [52, 53] showed that non-specific attractive interactions with the nuclear envelope result in preferential accumulation of heterochromatin in the nuclear periphery consistent with observations in conventional nuclei, confirming that binding to the nuclear lamina plays a key role in the spatial organization of heterochromatin.

Further in the hierarchy at the nuclear-scale chromatin organization are the **chromatin territories**. Microscopy has shown that interphase nuclei of many mammalian cells are partitioned into largely disjoint chromosome territories [54] whose radial positions display statistical preferences. This organization is not very intuitive from the polymer physics models where the territories would be expected to intermingle and fill out the entire nucleus. One plausible explanation would be the timescale needed for chromosomes to relax after mitosis. The relaxation time of polymers increases as the third power of their length in the presence of topological constraints. Thus, human chromosomes might simply not have enough time to mix, and this could reflect the individuality of interphase territories [55]. The out-of-equilibrium argument is also supported by the Hi-C study in mammalian chromosomes where genome-wide average contact frequency is inversely proportional to the genomic distance ($P_c(s) \propto s^{-1}$) (between ~ 500 kb and ~ 5 kb), in contrast to ($P_c(s) \propto s^{3/2}$) scaling for equilibrium polymers [44]. A fractal globule model,

where the polymer remains unentangled in contrast to an equilibrium model, was proposed to explain this scaling [56]. As highlighted in the above sections, the dynamics of the chromatin organization occurs at small length scales and highly viscous environment. Now that we understand the system well, the next is to outline the set of equations that governs the dynamics of fluid flows inside the cell. Most of the models for the chromatin polymer have neglected hydrodynamic interactions (or fluid flows) so that the novelty of the present work is precisely to consider it.

1.2 Low Reynolds number hydrodynamics: Stokes flow

As the problems of interest involve extremely small length scales $L \sim \mathcal{O}(\mu m - nm)$ typically in a fluid of viscosity $\mu \sim \mathcal{O}(100 - 10000 \text{ times of water})$, the governing Navier-Stokes equations describing the motion of a fluid element can be further simplified to a set of linear equations in specified regimes characterized by the zero limit of two dimensionless numbers. This regime of creeping flow where the inertia of both the fluid and particles can be neglected is known as Stokes flow regime (also known as non-inertial or viscous flows) such that,

$$Re = \frac{\rho U L}{\mu} \to 0, \quad \text{Reynold's number} = \frac{\text{Inertial forces}}{\text{Viscous forces}}, \tag{1.1}$$

and

$$St = \frac{\rho L^2}{T \mu} \to 0, \quad \text{Stokes number} = \frac{\text{time scale for viscous diffusion}}{\text{instrinsic time scale}}, \tag{1.2}$$

where ρ and μ are the density and viscosity of the suspending fluid, L and U are the particle size and the characteristic velocity scale of the particle with respect to the fluid respectively. In the absence of an intrinsic time-scale differing from L/U, $Re << 1$ allows

10

neglect of the acceleration term as well. However, if this is not the case and the motion has an intrinsic time-scale T, then the time scale $(\rho L^2/\mu)$ for momentum transport by the viscous diffusion should be much smaller than the intrinsic time scale. But the length and velocity scale do not have to be small for the low Reynolds number approximation to hold true. For example, flow in glaciers due to their sheer size have large length scales $\sim \mathcal{O}(m)$, extremely slow motions $\sim \mathcal{O}(years)$, and high viscosity μ, yet the dynamics of their flow still works well with creeping flow approximation.

1.2.1 Stokes equation

If both Re and St are small, then we can neglect the inertial and acceleration terms in the Navier-Stokes equations, which gives the following set of equations,

$$\boldsymbol{\nabla} \cdot \boldsymbol{u} = \boldsymbol{0}, \qquad \text{continuity equation,} \tag{1.3}$$

$$\boldsymbol{\nabla} \cdot \boldsymbol{\sigma} = -\boldsymbol{\nabla} p + \mu \boldsymbol{\nabla}^2 \boldsymbol{u} = \boldsymbol{0}, \qquad \text{momentum equation,} \tag{1.4}$$

where $\boldsymbol{u}(\boldsymbol{x})$ and $p(\boldsymbol{x})$ are the velocity and pressure fields respectively. The first equation describes the conservation of mass for incompressible fluids and the second equation states the balance of forces in a non-accelerating fluid. We assume the constitutive equation for a Newtonian fluid which implies the symmetric stress tensor $\boldsymbol{\sigma}$ is given by,

$$\boldsymbol{\sigma} = -p\mathbf{I} + \mu \left[\boldsymbol{\nabla} \boldsymbol{u} + \boldsymbol{\nabla} \boldsymbol{u}^T \right]. \tag{1.5}$$

Due to the linearity of the Stokes equations, it enjoys some additional perks which could be useful in present context [57]. Because of the **linearity**, a change in the magnitude of the forcing is linearly reflected in the fluid velocity. A direct mathematical consequence of the linearity of the Stokes equations is that the principle of superposition of solutions may be applied. The upside to this is that the individual solutions do not affect one another,

and are coupled only through boundary conditions. Linearity of the governing equations also implies that the motions are **reversible** in the driving force. This is meticulously illustrated in a short film by Taylor [58] where a colored drop is introduced into a viscous liquid contained in the annular region of two concentric cylinders. The colored drop partially mixes upon the rotation of the inner cylinder which on reversing the direction of rotation reforms its original spherical droplet shape with only a slight blurring due to molecular diffusion. Another important property is **instantaneity**. The absence of the time in the Stokes equations renders a quasi–static nature to the motion. There is no history dependence of the fluid motion captured by these equations which means, that the boundary motion is communicated to the entire fluid instantly. This is due to the harmonic properties of the Stokes equations which have instantaneous propagation of the information. Of course this is physically unrealistic and it should be kept under consideration that there is actually a finite propagation time for the information. Hence, motions caused by the particle are well–approximated by the Stokes equations out to distances $L < \mathcal{O}(\sqrt{\mu t / \rho})$. Another useful property is the ability to determine results for one Stokes flow field based upon the solution of another Stokes flow in the same geometry, also known as the reciprocal theorem. For an extensive discussion on the aforementioned topic, the readers are pointed to the book on suspension dynamics [57].

1.2.2 Resistance matrix

Now we wish to consider the motions caused by immersing a particle or collection of particles in a viscous fluid flow. The particle is subjected to a fluid stress field which results in the hydrodynamic force on the particle,

$$\mathbf{F}^{\mathrm{h}} = \int_S \boldsymbol{\sigma} \cdot \mathbf{n} \, \mathrm{d}S. \tag{1.6}$$

A simple interpretation of the total hydrodynamic force is that it is a sum of differential forces $\boldsymbol{\sigma} \cdot \mathbf{n} dS$ on the particle surface where $\mathbf{n}$ is the outward normal from the particle surface, and $\boldsymbol{\sigma} \cdot \mathbf{n}$ is called the traction force on the surface of the particle. We next consider the torque on the particle resulting from the fluid traction on the surface written as,

$$\mathbf{T}^{\mathrm{h}} = \int_S \mathbf{x} \times (\boldsymbol{\sigma} \cdot \mathbf{n}) \, \mathrm{d}S. \tag{1.7}$$

We can also point out that it is a first moment of the traction distribution. For intertialess motion, it is valuable to note that the resultant force and torque on the particle must go to zero, so that $\mathbf{F}^{\mathrm{h}} + \mathbf{F}^e = \mathbf{0}$ and $\mathbf{T}^{\mathrm{h}} + \mathbf{T}^e = \mathbf{0}$ where $\mathbf{F}^e$ and $\mathbf{T}^e$ is the sum of all external forces and torques respectively acting on the system. The linearity of the Stokes equations implies that there exists a relationship between the particle dynamical variables (force and force moment) and kinetic variables (velocity and velocity gradient) which is linear with respect to the motion.
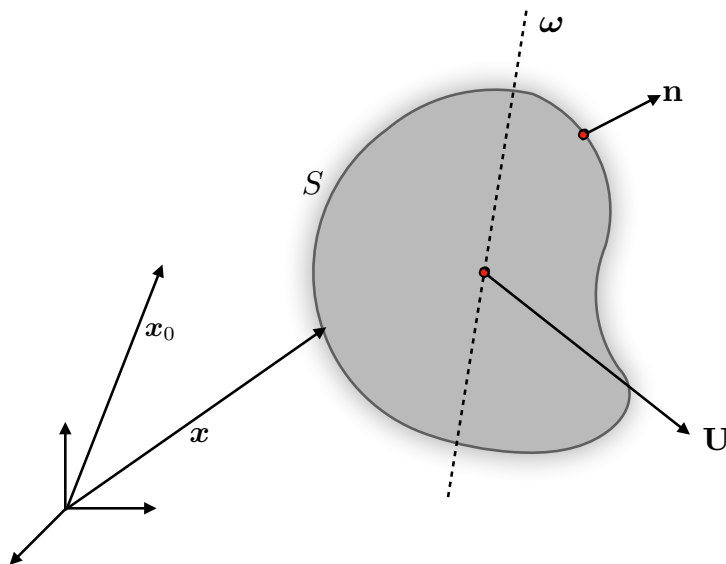
Figure 1.2: Particle translating at $\mathbf{U}$ and rotating at $\boldsymbol{\omega}$ in a stationary viscous flow.

We can illustrate this using an example of rigid particle translating at a velocity

U in a fluid at rest at large distance from the particle such that $\boldsymbol{u} = \mathbf{U}$ at the surface as shown in figure 1.2. Now the hydrodynamic drag ($\mathbf{F}^{\mathrm{h}}$) force depends linearly on stress $\boldsymbol{\sigma}$ as given in equation 1.6 which itself is linear $\mathbf{U}$. Hence the force $\mathbf{F}^{\mathrm{h}}$ depends linearly on $\mathbf{U}$. The scaling of viscous drag $F^{\mathrm{h}} \sim -(\mu U/L)L^2 = -\mu UL$ implies that the linearity can be expressed in a more general relation in the following manner,

$$\mathbf{F}^{\mathrm{h}} = -\boldsymbol{\mathcal{R}}^{\mathrm{FU}} \cdot \boldsymbol{u}, \tag{1.8}$$

where $\boldsymbol{\mathcal{R}}^{\mathrm{FU}}$ is the resistance tensor which couples velocity to force. Just as the force is related to translation, there is a hydrodynamic function relating rotation to torque,

$$\mathbf{T}^{\mathrm{h}} = -\boldsymbol{\mathcal{R}}^{\mathrm{T\omega}} \cdot \boldsymbol{\omega}. \tag{1.9}$$

Putting the above results together, we consider a rigid particle that is translating at a velocity $\boldsymbol{u}$ and rotating with an angular velocity $\boldsymbol{\omega}$ through a stationary fluid. The general linear relationship between the velocities and the hydrodynamic force and torque can be written as,

$$\begin{pmatrix} \mathbf{F}^{\mathrm{h}} \\ \mathbf{T}^{\mathrm{h}} \end{pmatrix} = \begin{pmatrix} \boldsymbol{\mathcal{R}}^{\mathrm{FU}} & \boldsymbol{\mathcal{R}}^{\mathrm{F\omega}} \\ \boldsymbol{\mathcal{R}}^{\mathrm{TU}} & \boldsymbol{\mathcal{R}}^{\mathrm{T\omega}} \end{pmatrix} \cdot \begin{pmatrix} \boldsymbol{u} \\ \boldsymbol{\omega} \end{pmatrix} = \boldsymbol{\mathcal{R}} \cdot \begin{pmatrix} \boldsymbol{u} \\ \boldsymbol{\omega} \end{pmatrix}, \tag{1.10}$$

where the resistance matrices $\boldsymbol{\mathcal{R}}^{\mathrm{FU}}$, $\boldsymbol{\mathcal{R}}^{\mathrm{F\omega}}$, $\boldsymbol{\mathcal{R}}^{\mathrm{TU}}$, and $\boldsymbol{\mathcal{R}}^{\mathrm{T\omega}}$ are determined by the geometry of the particle and are proportional to the fluid viscosity μ. $\boldsymbol{\mathcal{R}}$ is a $6N \times 6N$ matrix termed the resistance tensor where N is the number of particles present in the system ($N = 1$ in the present example). This relationship is useful when the translational and rotational velocities of the particle are specified and the force and torque have to be determined (the resistance problem). However, it is more common to have the opposite case in which the force and/or torque is specified where the relationship can be inverted to yield

$$\begin{pmatrix} \boldsymbol{u} \\ \boldsymbol{\omega} \end{pmatrix} = -\boldsymbol{\mathcal{M}} \cdot \begin{pmatrix} \mathbf{F}^{\mathrm{h}} \\ \mathbf{T}^{\mathrm{h}} \end{pmatrix}, \tag{1.11}$$

where $\boldsymbol{\mathcal{M}} = \boldsymbol{\mathcal{R}}^{-1}$ referred to as mobility matrix. We can obtain a simple expression for a sphere of radius a translating with velocity $\boldsymbol{u}$, the hydrodynamic force on the particle is $\mathbf{F}^{\mathrm{h}} = -6\pi\mu a\boldsymbol{u}$ where the resistance matrix is expressed as $\boldsymbol{\mathcal{R}}^{\mathrm{FU}} = 6\pi\mu a\mathbf{I}$, whereas the hydrodynamic torque on the same particle rotating with angular velocity $\boldsymbol{\omega}$ can be shown as $\mathbf{T}^{\mathrm{h}} = -8\pi\mu a^3\boldsymbol{\omega}$, and $\boldsymbol{\mathcal{R}}^{\mathrm{T}\omega} = 8\pi\mu a^3\mathbf{I}$. One important aspect is that unlike $\boldsymbol{\mathcal{R}}^{\mathrm{FU}}$ which scales linearly with the body size, $\boldsymbol{\mathcal{R}}^{\mathrm{T}\omega}$ depends on its cube.

1.2.3 Fundamental singularities and integral formulation

In Stokes regime, it is useful to express the flow field created by a particle motion in terms of driving external force ($\mathbf{F}^e$) from resistance matrix formulation in the above section such that,

$$\boldsymbol{u} = \left(\frac{\mathbf{I}}{r} + \frac{\boldsymbol{x}\boldsymbol{x}}{r^3}\right) \cdot \frac{\mathbf{F}^e}{8\pi\mu}. \tag{1.12}$$

The derivation of the above expression can be found in classical textbooks [57,59]. This velocity field retains only the most slowly decaying portion (r^{-1}) in the limit $a \to 0$ for a point size particle. We can also obtain $\boldsymbol{u}$ in a rather simple fashion by the device of shrinking the sphere. The idea is that if we are very far from the sphere, this is the dominant effect. Equivalently, we can show that this result is the flow induced by a "point force" of magnitude F^e, which is formally the solution to the problem,

$$-\boldsymbol{\nabla}p + \mu\boldsymbol{\nabla}^2\boldsymbol{u} = -\mathbf{F}^e\delta(\boldsymbol{x}), \qquad \boldsymbol{\nabla}\cdot\boldsymbol{u} = 0, \tag{1.13}$$

where $\delta(\boldsymbol{x})$ is the Dirac delta function. This velocity may be interpreted as the "impulse response" of these equations where the solution has been referred to as the *Stokeslet* written as

$$\boldsymbol{u} = \mathbf{G} \cdot \frac{\mathbf{F}^e}{8\pi\mu}, \tag{1.14}$$

15

in terms of the Oseen-Burgers tensor given by

$$\mathbf{G} = \left(\frac{\mathbf{I}}{r} + \frac{\boldsymbol{x}\boldsymbol{x}}{r^3} \right). \tag{1.15}$$

In more mathematical terms, $\mathbf{G}$ is the Green's function for the Stokes equations; because of the linearity of the Stokes equations, the Green's function may be used to construct the solution for a distribution of forces as can be seen in the upcoming discussions, but before that we can also construct a similar formulation for the torque rotating in a quiescent fluid with velocity $\boldsymbol{\omega}$. The flow field generated by this sphere is given by

$$\boldsymbol{u} = \frac{\mathbf{T}^e}{8\pi\mu} \times \frac{\boldsymbol{x}}{r^3}. \tag{1.16}$$

We obtain the fundamental solution for a point torque from the above expression, often called as *rotlet*. This idea of a Green's function is very useful because the flow solution for a distribution of forces may be obtained as a superposition of the flow fields generated independently by each of the forces. Now consider a rigid with a surface S particle immersed in a flow and exerting a surface traction on the surrounding fluid. The flow resulting from the surface traction can be written in integral form such that

$$u_j(\boldsymbol{x}_0) = -\frac{1}{8\pi\mu} \int_S G_{ji}(\boldsymbol{x}_0, \boldsymbol{x}) f_i(\boldsymbol{x}) \mathrm{d}S(\boldsymbol{x}) + \frac{1}{8\pi} \int_S u_i(\boldsymbol{x}) T_{ijk}(\boldsymbol{x}, \boldsymbol{x}_0) n_k \mathrm{d}S(\boldsymbol{x}), \tag{1.17}$$

where $f_i(\boldsymbol{x})$ is the traction on S and $\mathbf{T}$ is the associated stress tensor $T_{ijk}(\boldsymbol{x}) = -3x_i x_j x_k / r^5$. The first integral on the right hand side is called the *single layer potential* which describes the contribution by forces distributed on the surface of the particle. The second term is called the *double layer potential* and describes the contribution for deformable particles such as a drop. The usefulness of the integral representation can be corroborated from the reduction in dimensionality of the problem by one where the field variables can be computed by solving problems on two dimensional surfaces rather than three dimensional volume problem. In the next chapter 2, we will focus primarily on the ways to solve these

integral equations along with benchmarking and error analysis of the numerical methods for the problem of interest.

1.2.4 Brownian motion

At small length scales, as elaborated by the English botanist Robert Brown, a particle will undergo irregular, jittery motion when suspended in a solvent. Einstein reasoned on this observation that if tiny but visible particles were suspended in a liquid, the invisible atoms in the liquid would bombard the suspended particles and cause them to jiggle. He later explained the motion in detail, accurately predicting the irregular, random motion of the particles where the trajectories were uncorrelated and with no mean transport. These fluctuations incited by the fluid molecules enters in the form of thermal bath providing $0.5k_BT$ of energy for each degree of freedom. Keeping track of individual water molecules can prove to be computationally expensive as there are 6.02×10^{23} water molecules in a mole of water or more famously known as Avogadro's number. On the contrary, one can also resort to a continuum approach where a collection of water molecules moving irregularly with thermal entropic energy are treated as a single entity (or continuum) and exert a net force on the macroscopic particle. Einstein, Smoluchowski and Sutherland independently derived a relation between molecular movement and diffusion in a liquid relating the diffusivity of the particle and frictional resistance of the molecules,

$$\mathbf{D} = k_BT\boldsymbol{\mathcal{M}}, \tag{1.18}$$

where k_B is the Boltzmann constant and T is the absolute temperature of the suspending fluid bath. In modern language, equation (1.18) simply expresses the fluctuation-dissipation theorem. On the other hand, Stokes provided a hydrodynamic relation relating the frictional resistance and the properties of the particle and the medium in which it is suspended. Combining the two gives the well celebrated Stokes-Einstein-Sutherland

17

relation that relates the diffusivity $\mathbf{D}$ of a spherical particle to it's size a suspended in a fluid medium of viscosity μ,

$$\mathbf{D} = \frac{k_B T}{6\pi\mu a}\mathbf{I}, \tag{1.19}$$

where the diffusion tensor is isotropic for a spherical particle to account for its symmetry. Mathematically, the Brownian force $\mathbf{F}_i^{br}(t)$ are represented as follows

$$\langle\mathbf{F}^{br}(t)\rangle = \mathbf{0}, \quad \langle\mathbf{F}^{br}(t)\mathbf{F}^{br}(t')\rangle = 2k_B T\boldsymbol{\mathcal{M}}\delta(t-t'), \tag{1.20}$$

where $\boldsymbol{\mathcal{M}}$ denotes the grand mobility tensor that captures viscous resistance on the chain as well as long-ranged hydrodynamic interactions. $\langle..\rangle$ represents the ensemble average. The random fluctuations bombarded on a particle over a multiple ensembles will average out to zero, and the second moment correlates the variance of the fluctuations with the mobility. In the coming chapters, we will see the expression for mobility adapted for suitable problems and different strategies employed to calculate the Brownian displacements of a particle numerically.

1.3   Overview of the current thesis

The central theme of the dissertation is to understand physical principles underlying the dynamical self-organization of the genome in the cell across different length and time scales using theoretical and computational approaches. Specifically, we have explored the complex interplay between chain mechanics, hydrodynamic interactions and active response of the biological motors in the underlying physical mechanism leading to non-trivial dynamics in genome compartmentalization during cell differentiation that scales over a few microns and loop extrusion process that occurs on a nanometer scale. The non-equilibrium nature of the system in a highly heterogeneous environment (nucleus) poses a formidable mathematical and computational challenge which has been systematically addressed in

the present work. The current modeling effort complemented and informed some of the experimental observations which are useful to gain insight behind the physical mechanisms. The problem solving approach typically involves biophysical modeling, Brownian dynamics simulations, sophisticated computational and analytical techniques from active matter and fluid mechanics. The simulations presented in the upcoming chapters are highly optimized and have been performed on super computers to elucidate aforementioned problems of biological and physical significance. Through this work, we aim to provide physical explanation behind some of the peculiar observations that have been reported in the experiments and also possibly discover novel features which will assist the future experiments to a useful direction that can have broader applications in epigenetic functions across organisms and species.

Chapter 2 revolves around the biophysical modeling approaches in the context to DNA and chromosomes specifically at the interphase stage of the cell cycle. In this chapter, we develop much of theoretical and computational framework in a systematic manner for reader with little to no biology background. We outline the polymer modeling principles used in context to chromatin biology both for equilibrium and non-equilibrium processes. Finally, we also summarize the importance of the numerical modeling tool by highlighting the performance and scaling of the underlying computational algorithm.

Chapter 3 deals with the conformational dynamics of active flexible bead-rod polymer chains subjected to active force dipoles that drive fluid disturbances in the suspending solvent via numerical simulations. In this chapter, we explore the active coil–stretch which is internally driven by dipolar activity and make a comparison with the classical case exhibited by passive flexible polymers in externally applied extensional flows. We also present a simple kinetic model for an active timer based on the Fokker-Planck formulation to understand the stretching transition.

Chapter 4 is centered on activity induced segregation and compactness of the heterochromatin at a resolution of few microns or the size of the nucleus. Here, we use computational modeling based on a coarse-grained Langevin description of the whole nucleus to illuminate the biophysical principles and mechanisms underlying this complex spatial organization. We specifically analyze the role of euchromatic activity on nuclear dynamics and pattern formation, and demonstrate that active stresses and resulting nucleoplasmic flows serve to enhance heterochromatin segregation and compaction by promoting interactions and subsequent crosslinking between distant genomic segments.

Moving on to the length scales of a few nucleosomes at the nanometer resolution, chapter 5 focuses on the active dynamics of DNA loop extrusion. We present a microscopic bottom-up model for the dynamics of active loop extrusion that accounts for the structural features and dynamics of the motor proteins. Combining modeling and Brownian dynamics simulations, we demonstrate the roles played by hydrodynamic interactions, the active response of the motors and chain mechanics in assisting loop extrusion under different parameter regimes.

Concluding remarks and future work is discussed in depth in chapter 6.

Chapter 2

Biophysical modeling of DNA and chromatin

2.1 Introduction

Numerous biological polymers are characterized by myriad complex dynamical processes, and are driven out-of-equlibrium by continuous supply of energy in the form of ATP. Different types of molecular machines (like proteins) and ribosomes undergo structural and conformation changes which provide functional support to numerous processes inside the cell. This gives rise to plethora of dynamical processes and movements, including transport within the cell and the body, such as self-organization and spontaneous motion, with intriguing collective phenomena emerging by migration and locomotion also on scales much larger than individual cells. This assigns a very special status to the nature of living-and active-matter systems with characteristic features that separate it from passive systems like non-thermal fluctuations, broken detailed balance, and violation of the dissipation-fluctuation relation. This highly non-equilibrium makes it challenging for the development of theoretical/analytical ideas. Biological polymers and other filamentous structures are

an integral part of biological systems, and their conformational and dynamical properties are substantially affected by the active processes to a yet unresolved extent. This chapter primarily discusses various aspects of biophysical modeling and computational tools relevant for studying the class of active biopolymers, specifically DNA and chromatin, in a pedagogical manner. The discussion is divided in three main aspects. First, we will focus on modeling of biopolymers with special focus on chromatin (or DNA) as a soft polymer. Then we will move on to discuss hydrodynamics of polymers in viscous flow where we will outline the underlying governing physical principles and discuss associated numerical methods. Discussions from this chapter will help us to develop physical intuitions of several phenomena which will facilitate discussion in the upcoming chapters. There is a rich history of polymer literature that deals with dynamics of biopolymers. However, there are a very few pedagogical notes or books that develop the theory of mechanics and their interesting behaviors in a self-contained way. We start by a brief review of polymer models and highlight the differences between models used historically in the context of studying chromatin dynamics and organization. We then derive the governing equations used in the present study, and briefly discuss the associated terms in the equations.

2.2 Polymer models for the mechanisms of chromatin organization

Theoretical and computational approaches provide a support to experiments to dissect and improve our understanding of three dimensional structure of chromosomes and their organization. To make sense of increasingly large and complex mechanisms as explained in the earlier sections, first-principle models have been developed that try to explain the variety of chromatin patterns at different length scales in a coherent and mechanistic

framework. The genome is modeled as a polymer fiber, and its folding is guided by principles of polymer physics [60]. From the dynamics point of view, various computational chromatin-polymer models have been developed, and they quite accurately recapitulate many features of genome organization, pointing to polymer-polymer self-interactions as a major organizer of the genome [61]. The human chromosome consists of millions of base pairs bounded together by covalent bonds with a backbone of sugar-phosphate. This makes the DNA a perfect model that fits the description of a polymer, as a molecule built from many similar elements (called monomers) bonded together. This universality means that many concepts and results from polymer theory [62, 63] can be applied to understand the structure and dynamics of DNA and chromatin in cells.

An important property to model the dynamics of a polymer depends on it's flexibility, also represented mathematically as persistence length (ℓ_p). For a polymer of contour length L, on short length scales $\ell_p/L << 1$, it behaves as a rigid rod, while on larger ($\ell_p/L >> 1$) scales it can bend in arbitrary directions due to thermal fluctuations. As a consequence of this, polymers can have an infinite number of three dimensional orientations, or conformations. This is where some of the concepts of polymer theory can be used to predict statistical quantities, such as mean distance between the two ends of a polymer or the frequency with which two monomers contact each other. These quantities obey certain scaling laws, which is highly dependent on the numbers of monomers N for a discrete version of the polymer, or the contour length of the chain in the case of a continuum approach. There are myriad number of approaches that can be used depending on the regime of ℓ_p/L, and discussing each one of them is outside the scope of this study. Therefore, for linear chromatin fiber with persistence length 30 nm [64, 65], we will restrict ourselves to the case of loosely packed polymers with zero bending rigidity or resistance ($\ell_p/L << 1$) for the case of floppy polymers. In the simplest model, the ideal chain, bonds between

monomers have arbitrary orientation. At equilibrium, in the absence of external forces, the root mean squared end-to-end distance increases as $\sqrt{s}$ or $\sqrt{N}$ while contact frequency decay as $s^{-3/2}$. The more realistic chain model accounts for the fact that a polymer cannot self-intersect or self avoiding polymer. This will lead to expansion of the polymer accounting for excluded volume interactions and higher exponent (3/5) for end-to-end distance. In confined volumes such as the nucleus, however, this swelling can be counterbalanced by the presence of other chains (and other segments of the same chain). In that case, the scaling laws become similar to the ideal chain up to a distance where monomers behave as if they were no longer part of the same chain, at which point they level off. Equilibrium polymer models can also predicts the properties of polymer motions. For instance, the Rouse model describes the motion of a single monomer influenced by the presence of other monomers connected with each other by a linear spring. The mean-square displacement of a monomer grows as the square root of time over short timescales ($\langle r^2(t) \rangle \propto t^{1/2}$), unlike a free particle, for which the MSD is proportional to time ($\langle r^2(t) \rangle \propto t$) [62, 66].

There are primarily two major coarse-grained polymer model approaches to understand chromatin folding, one is the data-driven approach and the other is the bottom-up approach. In the data-driven approach, the chromatin interactions fitted or iterated from 5C or Hi-C matrices are used to reconstruct the spatial arrangement of the chromosome in 3D. These are also known as inverse (or fitting-based) models [67]. In this approach, the chromatin is modeled as a chain of interacting monomers connected by entropic constraints [4, 68]. The interaction parameters are then fitted using an iterative procedure generating a population of 3D conformations. As the genomic data sets are large, these approaches are useful, and often successfully reproduce Hi-C interactions maps but they often reveals little about the physical mechanisms behind the observed structures. On the contrary, the bottom-up approaches offers a systematic way to understand the mechanism

24

behind an observation which can be developed further to offer a unified approach that could consistently work for different cell types and species. A common approach is to write a simple model equation describing the bio-mechanics of the system, and then systematically improve it further until the model is able to predict the experimental observations. Some of the model parameters can also be obtained from the experimental data, and further insight is obtained from the output data. Even though the accuracy of the bottom-up approaches may not be as good as that of a fitting-based model with many parameter, they offer important understanding of molecular mechanisms. In this thesis, we will focus on models derived from polymer physics and Langevin simulations [62, 69]. The principle is as follows: the monomers of chromatin move according to Newton's second law, which states that the force exerted on a body is equal to its mass multiplied by its acceleration. This equation can be solved numerically to march in time to understand the dynamics of the system. After assigning an initial configuration, rest depends on the forces that each monomer experiences. This could be challenging as each monomer will experience forces like Coulomb charge interactions, van der Waals interactions etc. from the surrounding monomers. Such atomic level molecular dynamics simulations have been applied to proteins, as well as DNA and DNA-protein interactions [70]. However, calculating these forces at a resolution of individual atoms/proteins is computationally expensive.

To simulate large systems at the resolution of single chromosome territory or nucleus, one needs to resort to coarse-grained approaches. Instead of explicitly treating each water molecule, we can introduce a continuum approach and hydrodynamic theory for the interaction of the polymer with the surrounding fluid solvent using Brownian dynamics simulations. Furthermore, collections of proteins/nucleosomes are treated as a single unit, and the force exerted on them is written in the force balance equation. Consider a Brownian particle of mass M, the instantaneous general Langevin equation of motion

write:

$$M\frac{\mathrm{d}^2\mathbf{r}_i}{\mathrm{d}t^2} = -\boldsymbol{\nabla}U(\mathbf{r}) - \zeta\frac{\mathrm{d}\mathbf{r}_i}{\mathrm{d}t} + \zeta\boldsymbol{\kappa}\cdot\mathbf{r} + \mathbf{F}^{br}, \tag{2.1}$$

where $\mathbf{r}$ is the position of the particle, ζ is the specific friction coefficient, U is the sum of all the particle interaction potentials (e.g. mechanical, active, excluded volume etc.), and $\mathbf{F}^{br}$ captures Brownian displacements and is calculated to satisfy the fluctuation–dissipation theorem. This term provides a stochastic nature to the equation, and is originated from independent thermal collisions with the fluid molecules as described in Chap 1. For a uniform velocity gradient with zero velcoity at the origin, $\boldsymbol{u}(\mathbf{r}) = \boldsymbol{\kappa}\cdot\mathbf{r}$, where $\boldsymbol{\kappa}$ is the transpose of the velocity gradient tensor; i.e. $\boldsymbol{\kappa} = (\nabla\boldsymbol{u})^T$. Brownian dynamics is a limit case of Langevin dynamics framework. In this case, inertial effects are neglected with no average acceleration on the Brownian particle, and eventually results in a balance of the external forces to the viscous hydrodynamic drag [69]

$$\mathbf{0} = -\boldsymbol{\nabla}U(\mathbf{r}) - \zeta\frac{\mathrm{d}\mathbf{r}_i}{\mathrm{d}t} + \zeta\boldsymbol{\kappa}\cdot\mathbf{r} + \mathbf{F}^{br}(t). \tag{2.2}$$

Defining $\zeta = 6\pi\eta r_h$ as the friction coefficient and $D_b = k_B T/\zeta$ as the diffusion coefficient of the particle, the instantaneous velocity of the Brownian particle is written as follows:

$$\frac{\mathrm{d}\mathbf{r}_i}{\mathrm{d}t} = \boldsymbol{\kappa}\cdot\mathbf{r} + \frac{1}{\zeta}\Big(-\boldsymbol{\nabla}U(\mathbf{r}) + \mathbf{F}^{br}(t)\Big). \tag{2.3}$$

For the present study, interactions could include a potential to keep beads connected in a chain, and a potential preventing beads from overlapping in space. Another important component could come from the interaction of the polymer with other molecular motor proteins/enzymes which continuously inject energy into the system. Other important terms would include the interactions of one bead with the other via the solvent, and is captured by adding hydrodynamic interactions. As this is an important constituent in the present thesis, we will explore it in great depth in the following sections. All these interaction

potentials are extremely difficult to obtain from underlying physical principles or molecular mechanisms, and mostly rely on modeling insights from structural and functional information. While a chain of beads might look like a crude model for chromatin, it has been remarkably successful in explaining many of the observations such as Hi-C. Brownian dynamics simulations have also been used to study other kinds of soft matter systems [71], as for example, the rheological behavior of polymers [72], the dynamics of proteins and DNA [73–75] etc. Here, we will summarize some of the important polymer models, most of which do not account for hydrodynamic interactions, developed for understanding genome folding.

2.2.1   The fractal globule model

The first model to predict the (-1) power law decay of contact probability with genomic distance in the Hi-C experiments [44]. The fractal globule (FG) model, also known as the "crumpled globule" model, was introduced as a model for the 3D structure of DNA by Grosberg et. al. [76]. In this model, the chromatin folds into a hierarchical and unentangled structure by crumpling into small globules. Smaller globules then further crumple into larger globules. Apart from the -1 power-law decay in contact probability, another feature that makes it a good candidate is the unknotted behavior of the polymer which is essential for fast folding and hence transcription [77]. The fractal nature also explains the formation of territorial domains of individual chromosomes compared to well mixed state of equilibrium globule. The FG model also remains stable on the same time scale as that of the cell's lifespan while being in a non-equilibrium state of polymer folding. Finally, it was also observed that the diffusion of proteins in FG is comparatively faster compared to equilibrium globule, which facilitates the search for interacting loci of DNA binding proteins [78]. However, there are other observations which the FG model could

27

not explain.
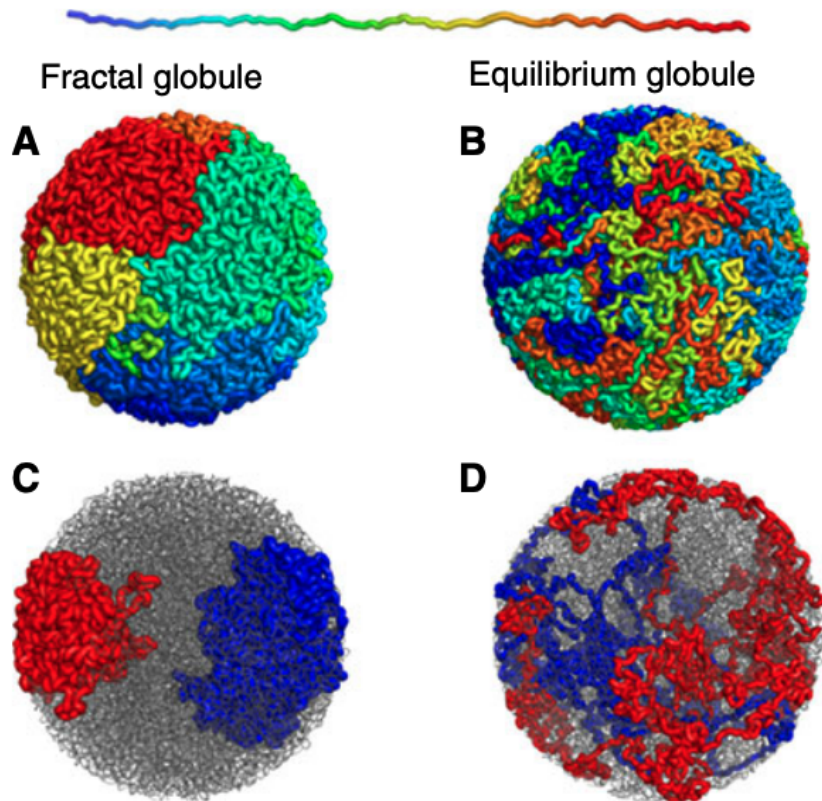
Figure 2.1: Conformations of the fractal (*a*) and equilibrium (*b*) globules. The presence of territorial domains in fractal globule strongly contrasts with the mixing observed in the equilibrium globule. Territorial organization of the fractal globule (*c*) is evident when two chains of 1,000 monomers (red, blue) each are outlined. The equilibrium globule (*d*), in contrast, has two chains mixed together in space. Compartmentalization means that parts of the chromatin stay near other parts with the same color. Figure borrowed from [77].

For instance, Hi-C experiments suggest the compartmentalization of the chromatin [44]. The homogeneous FG occupy the entire space without forming localised clusters and thus it does not show promoted segregation between compartments. Also, the decay in contact probability is not consistent across different species and tissues and does not always follow -1 power law [79, 80].

2.2.2 Strings and binders switch model

In this model, a combination of bead-chain polymer with generalized binders was used [81]. A single bead representing chromatin-binding protein complexes that can form bridging binders can generate chromatin interactions with the right scaling as a function of genomic separation and provide an understanding of the observation that there are different levels of compaction in different chromatin regions. The model is composed of a self-avoiding polymer chain with binding sites, to simulate the chromatin, and free beads (binders) of concentration c can attach to the binding sites [81–84]. Generally, the potential in such a model is written as,

$$U = U_{\text{backbone}} + U_{\text{ev}} + U_{\text{B}-\text{S}}, \tag{2.4}$$

in which U_{ev} is a repulsive interaction between a pair of beads and $U_{\text{B}-\text{S}}$ describes attractive interactions between binders and binding sites. The performance of the SBS model was examined with polymers and binders with different properties. At the same time, bead-chain model with diffusion bridges were also developed [85], and simulations of large chromosome regions at a resolution of $1-3$ kbp of DNA per bead were performed. Protein complexes that can form molecular bridges between multiple regions of DNA or chromatin have a tendency to cluster together, even in the absence of interactions between complexes. It is possible to predict Hi-C maps by using experimental data to infer the positions of the binding sites. Also, the factors were assumed to be generic chromatin binders, and data such as those from chromatin immunoprecipitation and sequencing (ChIP-seq) for different histone modifications are used to identify broad regions of binding. The model was able to predict the locations of a majority of chromatin domain boundaries. It also provided predictions on the protein clusters that arise in the simulations which look similar to some of the phase-separated membraneless organelles that are shown to be a key mechanism for formation of many nuclear structures [86]. When there are multiple bind-

ing sites, more complex patterns such as loops and rosettes appear along with formation of TADs [87]. Even though the bridging mechanism can readily explain compartment formation, however, it cannot generate loops with motif direction basis.

2.2.3 Loop extrusion model

Models based on loops have a relatively long history starting [88], and chromatin loops are an essential component of chromosome compaction and organization.
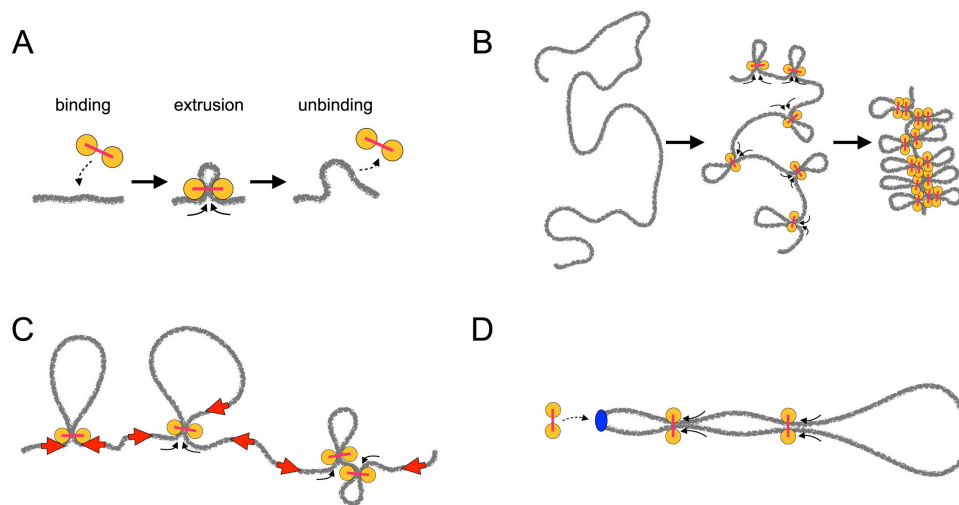
Figure 2.2: (*a*) Loop-extruding protein complexes, such as condensin and cohesin (yellow dumbbells), stochastically bind to chromatin/DNA (gray) and extrude chromatin loops until stochastically unbinding from chromatin. Here, a loop extruder is 'two-sided', so that it reels in chromatin both upstream and downstream of the extruder. (*b*) During prophase and prometaphase, a chromatin fiber (left and center) is progressively compacted by loop-extruding condensins into a dense brush of reinforced chromatin loops, forming a mitotic chromosome (right). (*c*) During interphase, loop-extruding cohesins can form topologically associating domains (TADs) by extruding loops until encountering a CTCF protein (red) oriented in the correct direction (i.e., an arrow pointing toward cohesin). (*d*) In bacteria, structural maintenance of chromosomes (SMC) complexes are loaded by ParB protein at parS sites near the origin of replication (blue). Extrusion proceeds across the circular chromosome, progressively juxtaposing the chromosomal arms. Figure taken from [88].

Loop extrusion is a motor-driven process by which a protein complex gradually

grows and enlarges chromatin/DNA loops by reeling in the chromatin fiber or DNA. This unsual motor activity is primarily ascribed to a widely conserved class of protein complexes known as structural maintenance of chromosomes (SMC) complexes, which include cohesin and condensin. Active loop extrusion by condensin was modeled such that the loop-extruding complexes could bind to and unbind from chromatin stochastically, and they contained two motor sub-units that could translocate in opposite directions, thus extruding the intervening DNA as a loop; extrusion continues until encountering another condensin or unbinding from DNA [27, 88]. Subsequent theory and simulations were able to show that a linearly ordered 'brush' of consecutive polymer loops could reproduce Hi-C maps for metaphase chromosomes [89]. Furthermore, it also showed that an array of consecutive loops can emerge from the collective activity of many loop extruders that dynamically exchange with the solvent in steady state [90]. Finally, 3D simulations showed that loop extrusion leads to compact morphologies and spatial resolution of sister chromatids [91]. While extrusion can explain looping, it does not provide a mechanism for compartment formation. In particular, the fact that compartment patterns remain but loop-mediated TADs are lost from Hi-C maps when cohesin is removed suggests that these features arise from different mechanisms [92, 93]. More details on the loop extrusion model can be seen in chapter 5.

2.3 Hydrodynamics of flexible active biopolymers

Biological polymers and other filamentous structures are involved in a myriad of complex dynamical processes essential for the functioning of the cell. In many cases, these polymers are subject to out-of-equilibrium microscopic stresses driven by ATP-powered active processes [94], resulting in unexpected emergent properties such as self-organization and spontaneous motion. These biological polymers and molecular motors have also been

extracted and utilized in vitro, for instance in motility assays [95] or as building blocks for active materials with various self-emergent properties [96–98]. A wide variety of other theoretical and computational models for active polymers have been proposed in recent years [99], guided by some of the experimental systems discussed above. Some these models have focused on semiflexible polymer chains, actuated by random correlated velocities [100] or composed of connected active Brownian particles (ABPs) [101–103], either with or without hydrodynamic interactions. Other models have considered free-draining flexible Rouse chains, either composed of ABPs [104], subjected to correlated fluctuating forces [105] or dipoles [106], or to active isotropic extensive or contractile forces [107]; these latter models, however, all neglected hydrodynamic interactions. The dynamics of soft flexible polymers in a Stokesian fluid has been the object of numerous mathematical and computational tools including the present one. Examples include the classical immersed-boundary-method (IBM) [108, 109], bead-rod and bead-spring models [110, 111], regularized Stokeslet formulation [112–114] and mesoscale methods such as dissipative particle dynamics or multi-particle collision dynamics [115]. A discussion and review of all such methods and formulation is beyond the scope of this thesis. Here we will outline the hydrodynamics of flexible polymers traditionally described by bead-rod/bead-spring models.

2.3.1   Bead-rod model

The most common coarse-grained models for polymers are the bead-rod chains, and were proposed to describe the structure of linear polymer chains. The spirit of these mesoscopic models is to coarse-grain out molecular details smaller than the finest length scale in the given model. Physically, the rod in a bead-rod chain corresponds to a Kuhn length ℓ_k (twice of persistence length). Mathematically, the rod acts as a constraint on

the system which ensures that adjacent beads in the chain are maintained at a constant separation length at all times. In practice, this constraint of maintaining the constant length of the polymer is handled using the method of Lagrange multipliers which results in an additional force in the form of tension in the chain. A simple coarse-grained model neglects any bending resistance or rotational constraints between adjacent rods known as the *freely jointed bead-rod chain* or *Kramers chain* [116]. In this case, beads do not represent central chain atoms, but a portion of the polymer chain. In short, a Kramers chain can be described as an ensemble of N_k beads linked by $N_k - 1$ rods of length ℓ, where each bead is characterised by a drag coefficient ζ. The general Langevin equation shown in equation (2.3) in the absence of hydrodynamic interactions can be reduced to,

$$\frac{\mathrm{d}\mathbf{r}_i}{\mathrm{d}t} = \boldsymbol{\kappa} \cdot \mathbf{r}_i + \frac{\mathbf{F}_i^c}{\zeta} + \boldsymbol{\xi}_i(t), \qquad i = 1, 2, ..., N_k \tag{2.5}$$

where the second terms captures motion under the internal constraint forces $\mathbf{F}_i^c$ ensuring inextensibility and the last term captures Brownian displacements and satisfies the fluctuation-dissipation theorem:

$$\langle \boldsymbol{\xi}_i(t) \rangle = \mathbf{0}, \quad \langle \boldsymbol{\xi}_i(t)\boldsymbol{\xi}_j(t') \rangle = 2D_b \mathbf{I}\, \delta_{ij}\delta(t - t'). \tag{2.6}$$

An important point to note is that we haven't considered the effects of other external forces that could affect the dynamics of the system. The effect of active forces will be discussed in the next section. The above set of equations have to be solved subject to constraints that the distance of separation between any two adjacent beads at any instant of time is fixed at ℓ, or

$$(\mathbf{r}_{i+1} - \mathbf{r}_i) \cdot (\mathbf{r}_{i+1} - \mathbf{r}_i) - \ell^2 = \phi^2, \qquad i = 1, 2, ...N_k - 1 \tag{2.7}$$

where ϕ^2 is a specified tolerance (typically $10^{-6} - 10^{-8}$). Equation (2.7) results in $2N_k - 1$ equations for N_k position variables $\mathbf{r}_i$ and $N_k - 1$ tensions T_i. We will now discuss the

integration scheme and subsequently, the algorithm to solve it. Specifically, we express the constraint forces in terms of scalar tensions T_i, which are Lagrange multipliers:

$$\mathbf{F}_i^c = T_i \mathbf{n}_i - T_{i-1} \mathbf{n}_{i-1}. \tag{2.8}$$

The two ends of the polymer are force free, which reflects in the boundary conditions $T_0 = T_N = 0$. To solve for the tensions, we use the algorithm of Liu [117], which uses a semi-implicit predictor-corrector scheme to ensure that the length of each link is preserved at the end of every time step. The first step in the time-marching scheme is an unconstrained explicit Euler step for the bead positions, in which the constraint forces are omitted:

$$\tilde{\mathbf{r}}_i^{n+1} = \mathbf{r}_i^n + \Delta t \left[\boldsymbol{\kappa} \cdot \mathbf{r}_i^n + \boldsymbol{\xi}_i(t) \right]. \tag{2.9}$$

The second step corrects the position $\tilde{\mathbf{r}}_i^{n+1}$ to account for the tensions, which are evaluated implicitly at time t_{n+1}:

$$\mathbf{r}_i^{n+1} = \tilde{\mathbf{r}}_i^{n+1} + \zeta^{-1} \Delta t \left[T_i^{n+1} \mathbf{n}_i^n - T_{i-1}^{n+1} \mathbf{n}_{i-1}^n \right]. \tag{2.10}$$

Eq. (2.10) can be further recast in terms of the unit directors $\mathbf{n}_i = (\mathbf{r}_{i+1} - \mathbf{r}_i)/\ell$ between beads as

$$\mathbf{n}_i^{n+1} = \tilde{\mathbf{n}}_i^{n+1} + \frac{\Delta t}{\zeta \ell} \left[T_{i+1}^{n+1} \mathbf{n}_{i+1}^n - 2 T_i^{n+1} \mathbf{n}_i^n + T_{i-1}^{n+1} \mathbf{n}_{i-1}^n \right]. \tag{2.11}$$

Applying the inextensibility constraint $|\mathbf{n}_i^{n+1}|^2 = 1$ then leads to an equation for the tensions:

$$\frac{2 \Delta t}{\zeta \ell} \left[T_{i+1}^{n+1} \mathbf{n}_{i+1}^n - 2 T_i^{n+1} \mathbf{n}_i^n + T_{i-1}^{n+1} \mathbf{n}_{i-1}^n \right] \cdot \tilde{\mathbf{n}}_i^n = 1 - |\tilde{\mathbf{n}}_i^n|^2 - \frac{\Delta t^2}{\zeta^2 \ell^2} \left| T_{i+1}^{n+1} \mathbf{n}_{i+1}^n - 2 T_i^{n+1} \mathbf{n}_i^n + T_{i-1}^{n+1} \mathbf{n}_{i-1}^n \right|^2. \tag{2.12}$$

The above set of non-linear equations can be solved by using Picard's method. The non-linear terms in tensions appearing are assumed to be small in comparison to the linear terms. Therefore, the set of equations is rewritten in terms of a linear set of equations

34

and solved iteratively by evaluating the non-linear part from the previous iteration. This results in a tridiagonal system of equations for the $N_k - 1$ tensions which can be solved until convergence. Besides Picard's method, an iterative Newton's method can provide faster convergence, but involves the calculation of a Jacobian matrix at every time step [110].

2.3.2 Bead-spring model

Owing to the fact that the DNA is an elastic filament, the bead-spring model is another candidate for modeling the dynamics of DNA. Let's consider the bead-spring chain model which constitutes of N_k beads joined by $N_k - 1$ freely rotating entropic springs. While the beads serve as interaction points with the solvent, the springs represent entropic effects due to the internal degrees of freedom. The governing equation retains the same structure as for the case of the bead-rod model, and is given by,

$$\frac{\mathrm{d}\mathbf{r}_i}{\mathrm{d}t} = \boldsymbol{\kappa} \cdot \mathbf{r}_i + \frac{\mathbf{F}_i^c}{\zeta} + \boldsymbol{\xi}_i(t), \qquad i = 1, 2, ..., N_k \tag{2.13}$$

where $\boldsymbol{\xi}_i$ represents the Brownian fluctuations as shown above, $\mathbf{F}_i^c$ is the effective spring force. The effective spring force on a bead i is given as,

$$\mathbf{F}_i^c = \begin{cases} \mathbf{F}_i^s & \text{if} \quad i = 1, \\ \mathbf{F}_i^s - \mathbf{F}_{i-1}^s & \text{if} \quad 1 < i < N, \\ \mathbf{F}_{N-1}^s & \text{if} \quad i = N, \end{cases} \tag{2.14}$$

where $\mathbf{F}_i^s$ is the spring force associated with spring i. Depending on the force law used for the springs, one can have different models for the spring. In this work, we have used primarily two different nonlinear spring force laws to model the springs, i.e. *finitely extensible nonlinear elastic* (FENE) force law and the *worm-like chain* (WLC) force law [73]. The force laws are given by,

$$\mathbf{F}_i^s = \frac{H_c \mathbf{Q}_i}{1 - Q^2/Q_0^2}, \qquad \text{FENE force law,} \tag{2.15}$$

$$\mathbf{F}_i^s = \frac{k_B T}{\ell_k} \left[\frac{1}{2} \frac{1}{(1 - (Q/Q_0)^2)} - \frac{1}{2} + \frac{2Q}{Q_0} \right] \frac{\mathbf{Q}_i}{Q_0}, \qquad \text{WLC force law,} \qquad (2.16)$$

where $\mathbf{Q}_i = \mathbf{r}_{i+1} - \mathbf{r}_i$ is the connector vector of the *ith* spring, H_c is the spring constant, Q is the magnitude of $\mathbf{Q}_i$ and Q_0 is the maximum extensibility of each spring. Finally, note that all spring force laws follow Hookean spring force law (linear spring or $\propto \mathbf{Q}$) in the small deformation limit. Now, we will illustrate the algorithms for the bead-spring model for the case of FENE chains realizing that extensions to other non-linear bead-springs can be similarly accomplished as can be seen in chapter 5 for worm like chains. Since the spring forces can be written in terms of orientation vector of the spring, it will be convenient to write the differential equation describing the dynamics in terms of the connector vectors $\mathbf{Q}_i$ rather than the bead positions $\mathbf{r}_i$.

$$\frac{d\mathbf{Q}_i}{dt} = \boldsymbol{\kappa} \cdot \mathbf{Q}_i + \zeta^{-1}(\mathbf{F}_{i+1}^c - \mathbf{F}_i^c) + (\boldsymbol{\xi}_{i+1} - \boldsymbol{\xi}_i), \qquad i = 1, 2, ..., N_k \qquad (2.17)$$

Equation (2.17) can be integrated utilizing various techniques. The simplest procedure involves marching in time using explicit forward Euler integration scheme. The next improvement to this method is the Picard's method, in which the explicit solution procedure is iterated at every time step until the residual of the solution falls below a pre-specified tolerance. However, the explicit schemes could lead to aphysical bond lengths which can exceed the maximum permissible value Q_0. Care should be taken such that the length of the connector vector $\mathbf{Q}$ does exceed the maximum limit. One can use Newton's method to solve the set of nonlinear equations at every time step until convergence is achieved. Furthermore, the resulting set of linear equations at every iteration in the Newton's method within a time step can be either solved using a direct solver, or an iterative solver. Here, we will outline a semi-implicit predictor-corrector method to integrate the above set of equations [110]. Given a bead-spring configuration at the time t, $\mathbf{Q}_i^n$, the configuration after one time step is generated as follows,

- *Predictor step*: In this step, $\mathbf{Q}_i^n$ is explicitly updated to obtain $\mathbf{Q}_i^*$ as,

$$\mathbf{Q}_i^* = \mathbf{Q}_i^n + \left[\boldsymbol{\kappa} \cdot \mathbf{Q}_i^n + \zeta^{-1}(\mathbf{F}_{i+1}^{c,n} - \mathbf{F}_i^{c,n}) + (\boldsymbol{\xi}_{i+1}^n - \boldsymbol{\xi}_i^n) \right].\Delta t \qquad (2.18)$$

- *Corrector step I*: Now we need to rewrite the spring potential forces in terms of the connector forces. In the this step, the spring forces for segments i and $i-1$ are treated implicitly when solving for $\bar{\mathbf{Q}}_i$ such that

$$\bar{\mathbf{Q}}_i + 2\zeta^{-1}\bar{\mathbf{F}}_i^s \Delta t = \mathbf{Q}_i^n + \left[\frac{1}{2}(\boldsymbol{\kappa} \cdot \mathbf{Q}_i^n + \boldsymbol{\kappa} \cdot \mathbf{Q}_i^*) + \zeta^{-1}(\bar{\mathbf{F}}_{i-1}^s + \mathbf{F}_{i+1}^{s,n}) + (\boldsymbol{\xi}_{i+1}^n - \boldsymbol{\xi}_i^n) \right]\Delta t. \quad (2.19)$$

Rearrangement of equation generates a cubic equation for the magnitude of $\bar{\mathbf{Q}}_i$ such that,

$$|\bar{\mathbf{Q}}_i|^3 - R|\bar{\mathbf{Q}}_i|^2 - Q_0^2(1 + \frac{1}{2}\Delta t)|\bar{\mathbf{Q}}_i| + Q_0^2 R = 0, \qquad (2.20)$$

where R is the magnitude of the right-hand side vector of equation (2.19). This equation has one unique root between 0 and Q_0, and thus choosing this root ensures that $|\bar{\mathbf{Q}}_i|$ is less than Q_0

- *Corrector step II*: In the final corrector step, the spring forces between for segments i and $i-1$ are treated implicitly, while the spring forces for segment is obtained from the previous corrector step

$$\mathbf{Q}_i^{n+1} + 2\zeta^{-1}\bar{\mathbf{F}}_i^{s,n+1}\Delta t = \mathbf{Q}_i^n + \left[\frac{1}{2}(\boldsymbol{\kappa} \cdot \mathbf{Q}_i^n + \boldsymbol{\kappa} \cdot \bar{\mathbf{Q}}_i) + \zeta^{-1}(\mathbf{F}_{i-1}^{s,n+1} + \mathbf{F}_{i+1}^s) + (\boldsymbol{\xi}_{i+1}^n - \boldsymbol{\xi}_i^n) \right]\Delta t.$$

$$(2.21)$$

The above equation also results in a cubic equation similar to (2.20), which can be solved to obtain a root for $|\mathbf{Q}_i|$ that lies between 0 and Q_0. Once every $\mathbf{Q}_i^{n+1}$ is known, the residual ϵ is calculated as the difference between the solutions $\bar{\mathbf{Q}}_i$ and $\bar{\mathbf{Q}}_i^{n+1}$

$$\epsilon = \sqrt{\sum_i^{N_k-1} (\mathbf{Q}_i^{n+1} - \bar{\mathbf{Q}}_i)^2}. \qquad (2.22)$$

If the residual is greater than a specified tolerance (10^{-6}), $\mathbf{Q}_i^{n+1}$ is copied onto $\overline{\mathbf{Q}}_i$ and step 3 is repeated until convergence. The overarching premise of this method is that the $\overline{\mathbf{F}}_i^s$ for any spring in the chain, is either written explicitly or solved implicitly through the cubic equation. This also ensures that no Brownian step is rejected at any time during the entire simulations as were performed in other studies [118]. Finally, the scaling (or non-dimensionalization) of the Langevin equation has been looked at in detail in individual chapters.

2.3.3   Hydrodynamic interactions

In this section, we focus on the treatment of the hydrodynamic interactions between monomers of the chain. As a particle moves along its trajectory, it exerts a force on the solvent which changes the velocity field. The disturbance velocity changes the viscous drag force exerted on the other particles. These interactions are included in Brownian dynamics through the use of an interaction tensor $\mathbf{G}_{ij}$. In the presence of hydrodynamic interactions, the Langevin equation becomes,

$$\frac{d\mathbf{r}_i}{dt} = \boldsymbol{\kappa} \cdot \mathbf{r}_i + \sum_{j=1}^{N_k} \mathbf{M}_{ij} \cdot \mathbf{F}_j^c(t) + \boldsymbol{\xi}_i(t). \tag{2.23}$$

$\mathbf{M}_{ij}$ denotes the grand mobility tensor that captures viscous drag on the beads as well as long-ranged hydrodynamic interactions:

$$\mathbf{M}_{ij} = \frac{\mathbf{I}}{\zeta}\delta_{ij} + \mathbf{G}(\mathbf{r}_i; \mathbf{r}_j)\left(1 - \delta_{ij}\right), \tag{2.24}$$

where $\mathbf{G}$ is the Oseen tensor introduced in chapter 1 (equation 1.15). Furthermore, the fluctuation-dissipation theorem governing the statistics of Brownian displacements becomes:

$$\langle \boldsymbol{\xi}_i(t) \rangle = \mathbf{0}, \quad \langle \boldsymbol{\xi}_i(t)\boldsymbol{\xi}_j(t') \rangle = 2k_B T \mathbf{M}_{ij}\delta(t - t'), \tag{2.25}$$

In practice, $\boldsymbol{\xi}_i$ is calculated as

$$\boldsymbol{\xi}_i(t) = \sum_{j=1}^{N} \mathbf{B}_{ij} \cdot \mathbf{w}_j, \qquad (2.26)$$

where $\mathbf{w}_j$ is an uncorrelated Gaussian white noise with zero mean and unit variance, and the tensor $\mathbf{B}_{ij}$ is related to the grand mobility tensor as

$$\sum_{p=1}^{N} \mathbf{B}_{ip} \cdot \mathbf{B}_{jp}^{T} = 2k_B T \mathbf{M}_{ij} . \qquad (2.27)$$

The standard technique for computing $\mathbf{B}_{ij}$ is to convert it into a lower triangular Cholesky factor of $\mathbf{M}_{ij}$, with an expensive cost of $O(N^3)$. A computationally cheaper approach is to use the iterative Lanczos method [119]. An additional complication arises from the calculation of tensions/spring forces when hydrodynamic interactions are included: indeed, Eq. (2.12), and Eq. (2.20) now involves a full matrix instead of a tridiagonal system, which we solve using LU decomposition. The interaction tensor in an unbound solvent is taken as the RPY tensor, which is non-positive-definite tensor when compared to Oseen tensor. This positive-definite form is important while evaluating Brownian fluctuations if particle separations are comparable to the particle radius. The RPY tensor modifies the small separation disturbance such that the diffusion tensor is always positive-definite.

2.3.4 Origin of sub-cellular activity

Cells and tissues provide extraordinarily complex examples for active matter far from thermodynamic equilibrium. Cells are inherently dynamic, and has long been the inspiration for studying how actively driven structures interact with the surrounding environment. Centrally involved in all the active processes are various molecular motor proteins that harness chemical energy derived from ATP hydrolysis to carry out directed mechanical function inside the cell. These motors have nanoscale dimensions, and are made of proteins and nucleic acids. Well studied examples of ATP-driven linear molecular

motors include myosins, kinesins, and dyneins responsible for cellular activities such as muscle contraction and active transport of most proteins and vesicles in the cytoplasm. In all three motor classes, ATP hydrolysis causes a small conformational change in a globular motor domain that is amplified and translated into movement with the aid of accessory structural motifs. Because the net force on the system containing nuclear components (or nucleus) is zero, the forces that act on the domains are equal in magnitude and opposite in direction (often referred to as *dipoles*), in order to conserve momentum. This creates a force dipole.

Contrary to cytoplasmic motors, the nuclear enzymes are functionally adapted to interact with chromatin (and DNA) (commonly referred to as nuclear enzymes), and play a significant role in genome organization and function inside the nucleus. They perform numerous site-specific functions such as transcription, replication and DNA repair, and are expected to significantly affect the local and global dynamics of chromosomes. In the present work, we have focused on both the dynamics and statistics of these specialized enzymes.
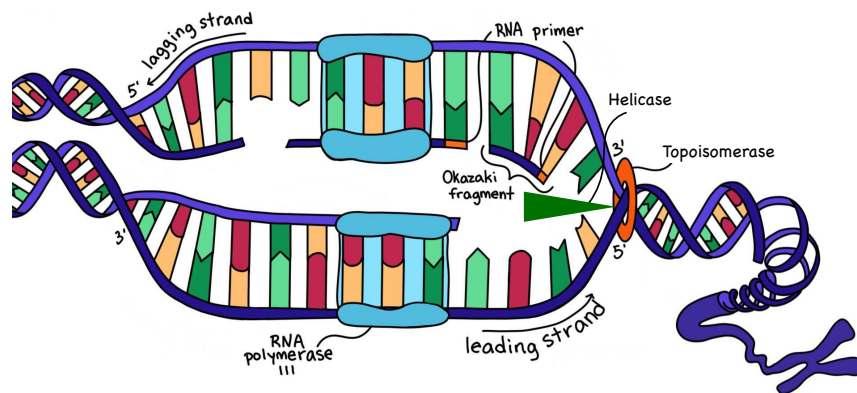
Figure 2.3: Figure illustrating the DNA replication process. Three nuclear enzymes RNA polymerase, Helicase and Topisomerase walks/slides along the DNA to perform mechanical function important during the during cell division for the DNA to make its copy. While doing the biomechanical function, the enzymes exert stresses on the chromatin fiber which goes into the solvent via the viscous hydrodynamic drag.

To understand how the active response of the motors contribute to the dynamics at different length and time scales, we will focus on the microscopic origin of an active process known as DNA replication [2]. This process involves three different nuclear enzymes working together to accomplish a process necessary for the transfer of the genetic information from one generation to the other. In the process, the parent DNA is copied to produce two identical DNA molecules and is essential process during the cell division because the two daughter cells must contain the same genetic material of the parent cell. It starts with helicase enzyme binding to the DNA and unzipping the double helix to divide it into two parent strands by breaking the bonds between them followed by action of polymerase which walks along the unzipped DNA to synthesize complementary sequences by matching bases into the original. During the entire process, topoisomerase consistently releases the tension created during the replication by opening up the DNA and unwinding it at the leading front. This entire sequence involves direct interaction of the motor with the chromatin fiber as they slide/walk along the chromatin and they tend to exert forces which go into the nucleoplasm via the viscous drag force and it can also affect the surrounding chromosomes (or nuclear components). We can motivate this active mechanism on a macroscopic level by arguing in terms of forces without the detailed microscopic description. This balance of forces can be simply described as dipoles which can be added as an additional term in the Langevin equation. Again, the collective mechanical response of the multiple motors in the presence of ATP can lead to emergent phenomena on a macroscopic scale, which is very typical of active matter problems and in doing so drives the system away from equilibrium.

While these active motions take place at the molecular scale, more recent work has shown that these motions can also lead to coherent behavior at micron scale (or nucleus size). The highlight of it is the work on chromatin dynamics by Zidovska *et*

41

al. [120], who used displacement correlation spectroscopy to quantify chromatin positional dynamics simultaneously across the entire nucleus in live cells by imaging of histones H2B-GFP. These observations revealed that chromatin moves coherently within large regions of 3–5 μm in size and lasting over several seconds. These correlated motions were found to be ATP-dependent and independent of the cytoplasmic cytoskeleton. Perturbation of major nuclear ATPases such as DNA polymerase, RNA polymerase II and topoisomerase II caused local displacements to increase, but completely blocked coherence. Although very few experiments have directly addressed the role of active processes on chromosome dynamics, many polymer models have been introduced to hypothesize their dynamical consequences.

Zidovska *et al.* [121] then proposed a hydrodynamic theory of chromatin dynamics that coarse-grained the action of ATPases into two basic types of active events: vector events that describe force dipoles generated by nuclear enzymes such as polymerases and helicases, and scalar events corresponding to the local de/condensation of chromatin caused by chromatin remodelers. This mean-field continuum theory predicts that dipolar activity is responsible for large-scale coherent motions [120, 121]. Alternative hydrodynamics-free approaches to modeling activity have also been developed, which use a 3D-conformational space of the chromatin fiber emerging from a quasi-equilibrium energy landscape [122]. Such an energy landscape was generated by Langevin dynamics at an effective temperature, implicitly capturing the chromatin activity. Another hydrodynamics-free model explored the spatiotemporal dynamics of interphase chromosomes describing chromatin as a heteropolymer informed by the HiC data of human chromosomes [123, 124], with chromatin activity also mimicked by an isotropic noise. Both of these models successfully recapitulated large-scale coherency of chromatin motions.

More recent work has shown that these motions can propagate via solvent-mediated

interactions. The highlight of it is the work by Saintillan, Shelley and Zidovska [9] built upon the concept of vector events to develop a computational model of active chromatin hydrodynamics that accounts for the role of ATP-driven processes. A long flexible polymer confined inside a spherical cavity and subjected to stochastic force dipoles was simulated. These force dipoles generated fluid flows in the nucleoplasm, which in turn drove local nematic alignment of the chain. This positive feedback occurred only for extensile dipoles and resulted in large-scale coherent motions by a mechanism similar to the generic bend instability of extensile active nematics [125–127]. These simulations assumed a homopolymer chain, thus no macroscopic self-organization was observed beyond the alignment induced by hydrodynamic interactions. These simulation studies reflected the importance of hydrodynamic interactions in driving large scale coherent structures. Building upon the numerical and theoretical ideas shown in this chapter, we can now probe some of the problems in context to genome organization in the upcoming chapters.

2.4 Conclusions

In this chapter, we have outlined the fundamentals that governs the dynamics and equilibrium properties of chromatin organization using framework of polymer physics. Although a general model linking all four levels of chromatin organization, from nucleosomes to the entire nucleus, is still lacking, the present work is an attempt to provide a holistic approach to a unifying framework. The tools summarized in this chapter formed the backbone of the upcoming topics related to chromatin dynamics and organization at different length scales ranging from bp at a resolution of few nucleosomes to chromatin territories and nucleus of the size of microns. This chapter will serve as a guiding tool for the non-biologists to develop an intuition on bio-mechanical aspects of a complex and multi-scale problem of chromatin organization.

Chapter 3

Self-induced hydrodynamic coil-stretch transition of active polymers

3.1   Introduction

Biological polymers and other filamentous structures are involved in a myriad of complex dynamical processes essential for the functioning of the cell. Examples of such systems abound and include: the coordinated action of dynein motors along the microtubule bundle comprising eukariotic cilia and flagella, where active sliding forces exerted by the motors result in spontaneous beating and locomotion [139, 140]; the unidirectional transport of cargo by kinesin and dynein motors along tracks of microtubules in the cell cytoskeleton [141, 142]; the contraction of the actin cortex under the action of myosin motors during various processes such as cytokinesis [143] and platelet formation [144]; and the generation of cytoplasmic streaming flows by dynein motors marching along microtubules during oocyte development [145, 146]. These biological polymers and molecular motors

have also been extracted and utilized in vitro, for instance in motility assays [95] or as building blocks for active materials with various self-emergent properties [96–98].

In this work, we analyze the conformational dynamics of an active flexible bead-rod linear polymer chain subjected to active force dipoles that drive fluid disturbances in the suspending solvent. The model is based on the past work of Saintillan *et al.* [9], but we provide here a more systematic characterization of the role of activity and hydrodynamic interactions on chain dynamics and conformations in unconfined dilute systems. Our numerical simulations demonstrate that extensile dipolar activity results in the spontaneous stretching of the chains above a critical level of activity by driving a coherent long-ranged extension-dominated flow that overcomes thermal fluctuations and unravels the polymer. This 'active coil–stretch transition' is reminiscent of the transition exhibited by passive flexible polymers in externally applied extensional flows [147], but is internally driven by dipolar activity in the present case.

3.2 Active polymer model

3.2.1 Langevin formulation

We study the dynamics and conformations of active flexible polymer chains in an unconfined environment. Figure 3.1 shows a graphical representation of the polymer model, which consists of a linear chain of N beads of radius a connected by $N - 1$ freely jointed inextensible rods of length ℓ with no bending resistance or rotational constraints. The chain is subject to tension forces, thermal fluctuations and excluded volume interactions. In addition, we model activity in terms of force dipoles (pairs of equal and opposite forces) that are applied to the solvent and drive hydrodynamic disturbances as we explain in Sec. 3.2.2 [9, 121]. We denote by $\mathbf{r}_i(t)$ the position of bead i, and by $\mathbf{n}_i(t) = |\mathbf{r}_{i+1} - \mathbf{r}_i|/\ell$

the unit vector pointing from bead i to bead $i + 1$. At low Reynolds number, the motion of the chain is overdamped and satisfies the Langevin equation [69]:

$$\frac{\mathrm{d}\mathbf{r}_i}{\mathrm{d}t} = \mathbf{u}^a(\mathbf{r}_i, t) + \frac{1}{\zeta}\left[\mathbf{F}_i^c(t) + \mathbf{F}_i^e(t)\right] + \boldsymbol{\xi}_i(t). \tag{3.1}$$

The first term on the right-hand side describes advection by the active fluid flow $\mathbf{u}^a$ induced by ATP-powered molecular motors, which we discuss in Sec. 3.2.2.
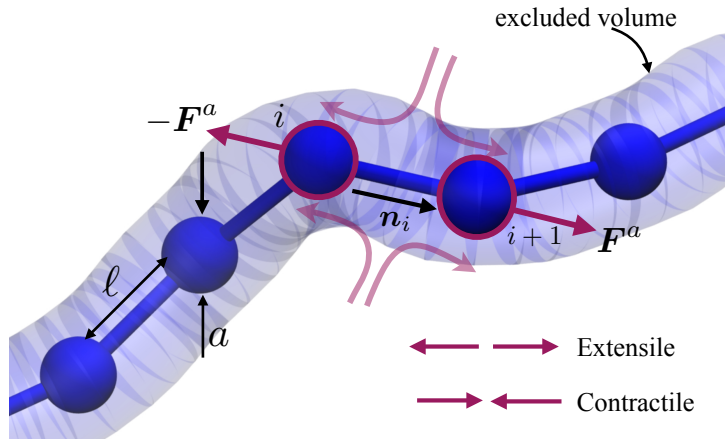
Figure 3.1: Coarse grained active polymer: The chain is modeled as a long freely-jointed chain of N beads each with hydrodynamic radius a and connected by rigid links of length ℓ. Active dipoles (extensile or contractile) bind stochastically to individual links, with forces applied directly on the suspending fluid.

The second term captures motion under the internal constraint forces $\mathbf{F}_i^c$ ensuring inextensibility (see Sec. 3.2.3) and under excluded volume forces $\mathbf{F}_i^e$ acting on bead i, with hydrodynamic friction coefficient $\zeta = 6\pi\eta a$. Excluded volume interactions are captured by a soft repulsive potential:

$$\mathbf{F}_i^e = -\sum_{j \neq i} \nabla_i \Phi(\mathbf{r}_i - \mathbf{r}_j), \quad \text{with} \quad \Phi(\mathbf{r}) = \frac{\Phi_0}{r^n}, \tag{3.2}$$

with $n = 3$. The parameter Φ_0 is ad hoc and selected to ensure that the chain does not cross itself. Finally, the last term in Eq. (3.1) captures Brownian displacements and

satisfies the fluctuation-dissipation theorem:

$$\langle \boldsymbol{\xi}_i(t) \rangle = \mathbf{0}, \quad \langle \boldsymbol{\xi}_i(t)\boldsymbol{\xi}_j(t') \rangle = 2D_b \mathbf{I}\, \delta_{ij}\delta(t-t'), \tag{3.3}$$

where $D_b = k_{\mathrm{B}}T/\zeta$ is the Brownian diffusivity of an isolated bead. We note that the Langevin equation (3.1) models the polymer as a freely draining chain. Constraint and excluded volume forces are applied locally on each bead and do not drive any hydrodynamic interactions: the only flow in the solvent is assumed to be that induced by active dipoles. We note that this is an approximation that is convenient computationally. This description can be improved by accounting for hydrodynamic interactions between distant chain segments: we consider this more general case in Appendix A, where we find that hydrodynamic interactions tend to damp the effect of activity due to the enhanced viscous drag on the chain.

3.2.2 Active forces and hydrodynamic flow

A key feature of our model is the inclusion of active forces and flows, which model of the effects of the activity of ATP-powered motor proteins performing work along the polymer chain. The stresses exerted by these motors are coarse grained in the form of active dipolar force pairs that occur on the scale of one chain link and drive fluid disturbances (Fig. 3.1). As the motors bind and unbind stochastically along the chain, we assume that each link can be either active (dipole on) or inactive (dipole off), and the time in a given state is drawn from an exponential distribution with two distinct rates k_{on} and k_{off}. These rates set the probability $p_a = k_{\mathrm{on}}/(k_{\mathrm{on}} + k_{\mathrm{off}})$ that any given link is active at a point in time. Note that p_a can also be interpreted as the mean fraction of active links in the system. When a link is in the active state, two equal and opposite forces are applied to the viscous surrounding fluid at the positions of the two end beads:

$$\mathbf{F}_i^a = -F_0\mathbf{n}_i(t), \quad \mathbf{F}_{i+1}^a = F_0\mathbf{n}_i(t), \tag{3.4}$$

47

where F_0 is the strength of the active force, assumed to be constant. This effectively describes a force dipole with magnitude $F_0\ell$, which can be either extensile ($\leftarrow\rightarrow$) or contractile ($\rightarrow\leftarrow$) as shown in Fig. 3.1. In the present model, we assume that these two forces are applied directly to the solvent, where they drive an active hydrodynamic flow that can be obtained as

$$\mathbf{u}^a(\mathbf{r}_i) = \sum_{j=1}^{N} \mathbf{G}(\mathbf{r}_i; \mathbf{r}_j) \cdot \mathbf{F}_j^a, \tag{3.5}$$

where $\mathbf{G}$ denotes the Oseen tensor in free space:

$$\mathbf{G}(\mathbf{r}_i, \mathbf{r}_j) = \frac{1}{8\pi\mu r_{ij}} \left[\mathbf{I} + \hat{\mathbf{r}}_{ij}\hat{\mathbf{r}}_{ij}\right], \tag{3.6}$$

where $r_{ij} = |\mathbf{r}_i - \mathbf{r}_j|$ is the distance between beads i and j, and $\hat{\mathbf{r}}_{ij} = (\mathbf{r}_i - \mathbf{r}_j)/r_{ij}$ is the unit vector pointing from bead j to bead i.

3.2.3 Constraint forces and numerical algorithm

Chain inextensibility is imposed by means of the constraint forces $\mathbf{F}_i^c$ in Eq. (3.1), which are calculated to ensure that the length of each link remains constant and equal to ℓ. Specifically, we express these constraint forces in terms of scalar tensions T_i, which are Lagrange multipliers:

$$\mathbf{F}_i^c = T_i\mathbf{n}_i - T_{i-1}\mathbf{n}_{i-1}. \tag{3.7}$$

The two ends of the polymer are force free, which reflects in the boundary conditions $T_0 = T_N = 0$. To solve for the tensions, we use the algorithm of Liu [117], which uses a semi-implicit predictor-corrector scheme to ensure that the length of each link is preserved at the end of every time step. The first step in the time-marching scheme is an unconstrained explicit Euler step for the bead positions, in which the constraint forces are omitted:

$$\tilde{\mathbf{r}}_i^{n+1} = \mathbf{r}_i^n + \Delta t \left[\mathbf{u}^a(\mathbf{r}_i^n) + \boldsymbol{\xi}_i^n + \zeta^{-1}\mathbf{F}_{i,n}^{ev}\right]. \tag{3.8}$$

48

The second step corrects the position $\tilde{\mathbf{r}}_i^{n+1}$ to account for the tensions, which are evaluated implicitly at time t_{n+1}:

$$\mathbf{r}_i^{n+1} = \tilde{\mathbf{r}}_i^{n+1} + \zeta^{-1}\Delta t \left[T_i^{n+1}\mathbf{n}_i^n - T_{i-1}^{n+1}\mathbf{n}_{i-1}^n\right]. \tag{3.9}$$

Eq. (3.9) can be further recast in terms of the unit directors between beads as

$$\mathbf{n}_i^{n+1} = \tilde{\mathbf{n}}_i^{n+1} + \frac{\Delta t}{\zeta\ell} \left[T_{i+1}^{n+1}\mathbf{n}_{i+1}^n - 2T_i^{n+1}\mathbf{n}_i^n + T_{i-1}^{n+1}\mathbf{n}_{i-1}^n\right]. \tag{3.10}$$

Applying the inextensibility constraint $|\mathbf{n}_i^{n+1}|^2 = 1$ then leads to an equation for the tensions:

$$\frac{2\Delta t}{\zeta\ell} \left[T_{i+1}^{n+1}\mathbf{n}_{i+1}^n - 2T_i^{n+1}\mathbf{n}_i^n + T_{i-1}^{n+1}\mathbf{n}_{i-1}^n\right] \cdot \tilde{\mathbf{n}}_i^n = 1 - |\tilde{\mathbf{n}}_i^n|^2$$
$$- \frac{\Delta t^2}{\zeta^2\ell^2} \left|T_{i+1}^{n+1}\mathbf{n}_{i+1}^n - 2T_i^{n+1}\mathbf{n}_i^n + T_{i-1}^{n+1}\mathbf{n}_{i-1}^n\right|^2. \tag{3.11}$$

This system of quadratic equations can be solved iteratively, where each iteration involves inverting a linear tridiagonal system corresponding to the left-hand side in Eq. (3.11). A small number of iterations (typically ≤ 10) is sufficient to achieve convergence.

3.2.4 Scalings and parameters

In the following, we present results in dimensionless form, where all the variables are scaled using the following characteristic time, length and force scales:

$$t_c = \frac{\zeta\ell^2}{k_B T}, \qquad \ell_c = \ell, \qquad F_c = \frac{k_B T}{\ell}. \tag{3.12}$$

With this choice, the dimensionless active dipole strength becomes

$$\sigma_0 = \frac{F_0\ell}{k_B T}, \tag{3.13}$$

where $\sigma_0 > 0$ and $\sigma_0 < 0$ represent extensile and contractile systems, respectively. We also introduce an activity parameter A, defined as

$$A = p_a\sigma_0 = \frac{k_{on}}{k_{on} + k_{off}}\frac{F_0\ell}{k_B T}, \tag{3.14}$$

which can be viewed an effective active dipole strength corrected for the stochasticity of molecular motors [9].

3.3 Results and discussion

3.3.1 Conformational dynamics and flow fields

We performed simulations of polymer chains composed of $N = 3 - 150$ beads, for varying values of p_a and σ_0.
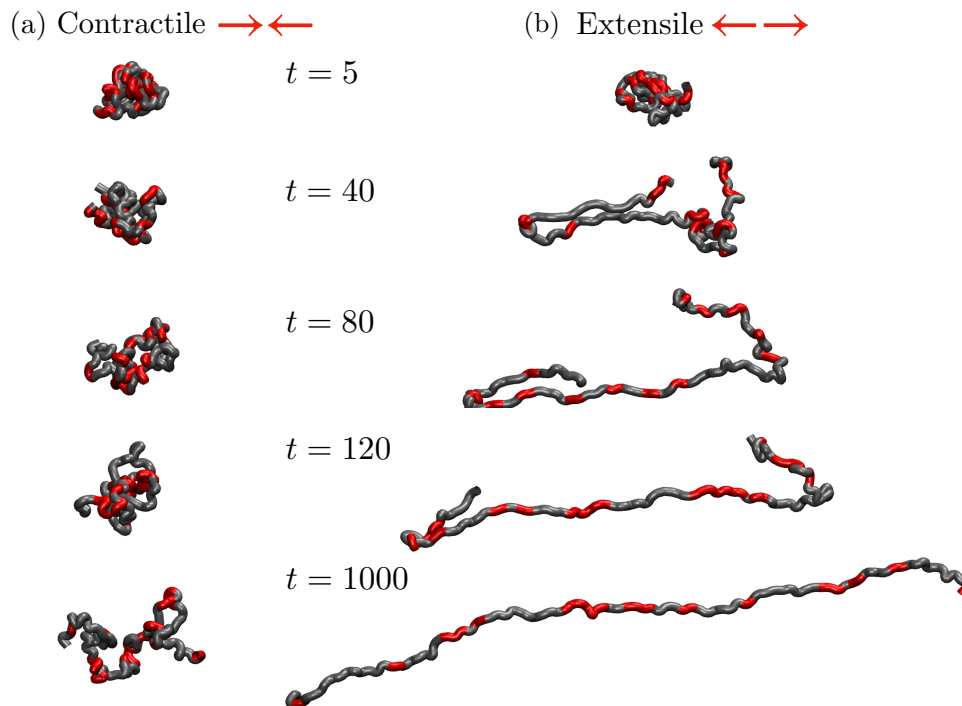
Figure 3.2: Snapshots from two simulations of (a) a contractile system ($A = -10$) and (b) an extensile system ($A = 10$) with $N = 100$, $k_{\text{on}} = 100$ and $k_{\text{off}} = 500$. The chains were initially prepared as random walks. Red segments show in the instantaneous positions of active force dipoles. The contractile chain swells but remains in an isotropic coiled state, whereas the extensile chain progressively unfolds to reach a fluctuating stretched conformation.

Figure 3.2 shows snapshots from simulations of two active chains, one contractile

and one extensile, with $N = 100$ and $A = \pm 10$. Both systems were prepared as random walks at $t = 0$. At short times, excluded volume forces cause both polymers to swell in all directions, while dipolar flows are being driven locally along the chains. In the contractile case, the chain continues to swell slightly as the flows induced by the active dipoles constantly rearrange neighboring links, with no net emergent alignment. At statistical steady-state, the contractile chain remains in an isotropic coiled state, with thermal fluctuations enhanced by the dipolar fluid flows. The case of extensile activity is markedly different. Here, neighboring links align in the dipolar flows, which have extensional symmetry, resulting in long chain segments opening up and stretching, until the chain fully unfolds into a stetched state where activity-induced flow alignments competes against thermal fluctuations, which favor the coiled state. Similar dynamics had previously been observed by Saintillan *et al.* [9]. The mean direction of alignment of the chain is arbitrary, but remains roughly constant over the course of the transient. At steady state, the axis of alignment very slowly diffuses as a result of Brownian motion, which also introduces stochasticity in the flow field by causing fluctuations of the dipole orientations.

These dynamics can be understood based on the flow fields induced by individual dipoles as depicted in Fig. 3.3(a,b). In the contractile case shown in (a), the flow is compressional along the axis of the dipole and extensional in the perpendicular plane, which tends to rotate neighboring chain links so that they align at $\approx 90º$, thus forming kinks in the chain. Conversely, in the extensile case shown in (b), the flow is extensional along the axis of the dipole, which tends to rotate neighboring links so that they align with the dipole, thus unfolding and straightening the chain. This flow-induced alignment observed in extensile systems not only affect nearest neighbors but is long-ranged due to the slow decay as $1/r^2$ of dipolar flows in the Stokes regime. Furthermore, the effect is self-amplifying: as several chain segments carrying dipoles align with each other, their flow

fields superimpose coherently to further enhance alignment.
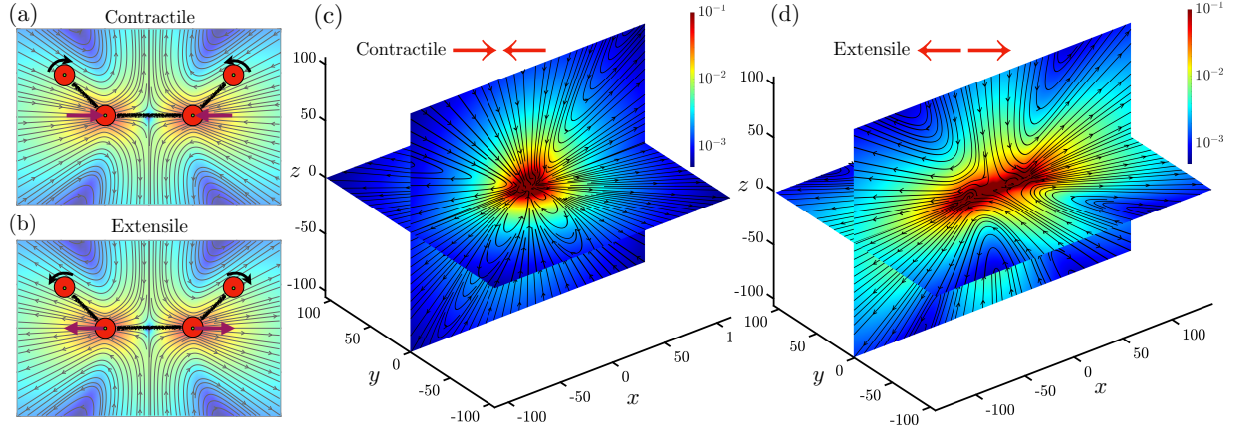
Figure 3.3: (a,b) Flow fields induced by contractile (a) and extensile (b) dipoles, respectively, illustrating their effect on chain dynamics. The purple arrows show the direction of the active forces, whereas the black arrows show the direction of rotation of the neighboring links. (c,d) Time average flow fields induced by (a) a contractile system ($A = -10$) and (b) an extensile system ($A = 10$) with $N = 100$, $k_{\mathrm{on}} = 100$ and $k_{\mathrm{off}} = 500$. In the contractile case, the chain is coiled at the origin. In the extensile case, the coordinate system was rotated to align the principal axis of the chain with the x direction.

This positive feedback loop ultimately results in the full stretching of the chain under its self-induced flow. Time-averaged flow around the two polymer chains of Fig. 3.2 are shown in Fig. 3.3(c,d). The flow in the contractile case in (c) displays extension and compression along various directions but shows not clear large-scale symmetry. On the other hand, dipolar alignment in the extensile case shown in (d) conspires to drive a self-sustained extensional flow on the scale of the polymer chain, which acts to stabilize the unfolded stretched conformation. The observed transition from an initial coiled state to a stretched configuration in extensile systems is reminiscent of the classic coil-stretch transition of flexible polymers in linear extensional flows [147], where the stretching is due to the viscous drag on the polymer by an externally applied flow. Here, the transition is instead an emergent phenomenon resulting from the spontaneous alignment of the chain under the extensile dipoles that it carries. We discuss this analogy in more detail further

below.

3.3.2 Steady-state statistical properties

We now discuss conformational properties at statistical steady-state, which we characterize in Fig. 3.4 shown various structural order parameters as functions of σ_0. Three sets of simulations are shown, two with $N = 50$ and one with $N = 100$. In the case of $N = 50$, two different combinations of on/off rates were used: $(k_{\text{on}}, k_{\text{off}}) = (100, 500)$ and $(10, 50)$, which have the same value of p_a and thus the same mean number of dipoles. All shown quantities were measured after reaching steady state and were averaged over time and over an ensemble of 5 different simulations. We first show in Fig. 3.4(a) the relative end-to-end distance defined as

$$R_n = \frac{|\mathbf{r}_N - \mathbf{r}_1|}{N - 1},\tag{3.15}$$

with maximum value of 1 corresponding to a perfectly straight polymer chain. For a perfect random walk (coiled configuration), the expected value is $R_n = \ell \sqrt{N_k}$ (ℓ is the fixed step size and N_k is the number of steps in a random walk). As shown in Fig. 3.4(a), the end-to-end distance is unaffected by activity in the contractile case ($\sigma_0 < 0$), where it sligthly exceeds the random walk prediction due to excluded volume effects. In the extensile case, however, R_n starts increasing above a critical positive value of σ_0, reaching ≈ 0.6 for the longest chain when $\sigma_0 = 50$. Longer chains tend to stretch more for the same dipole strength, since they are decorated by more dipoles thus enhancing the self-unfolding effect described in Sec. 3.3.1. The two simulations with $N = 50$ provide insight into the role of the on/off rates on the dynamics: the end-to-end distance, as well as the other order parameters we discuss below, is only weakly affected by the actual values of k_{on} k_{off} at a given value of p_a. Stretching is slightly weaker in the case with the large rates (blue triangles), as there is more stochasticity in the dipoles in that case. The unfolding and

stretching of extensile chains under their self-induced flows can also be interpreted as an increase in orientational correlations along the chain, i.e., as an increase in the effective rigidity of the polymer.
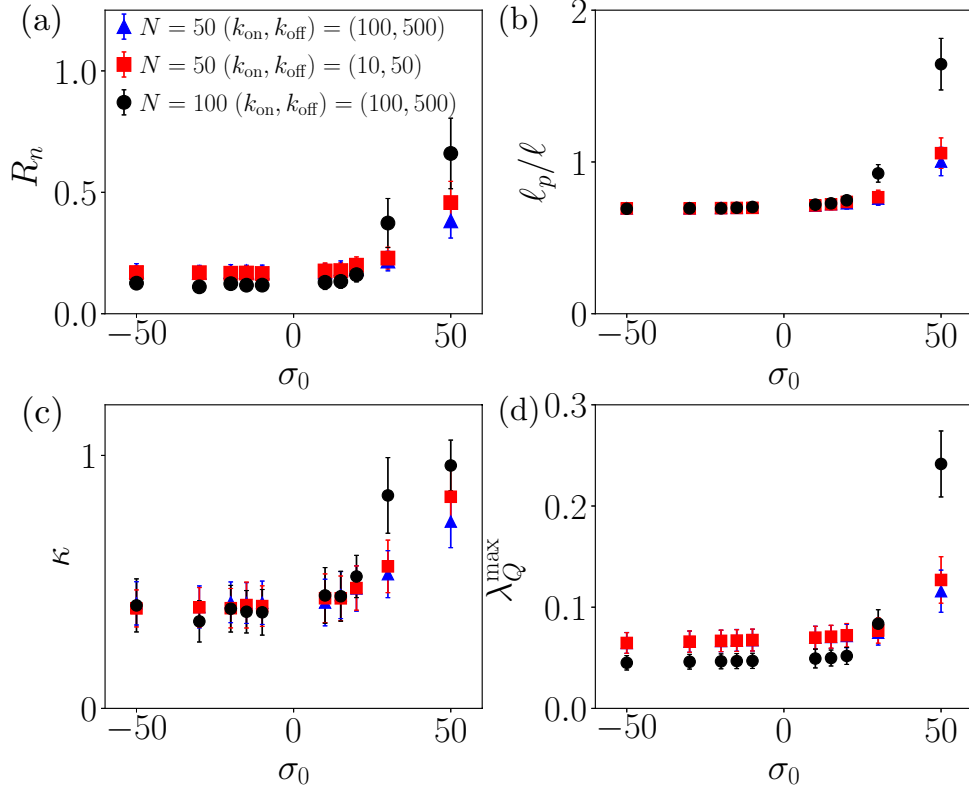
Figure 3.4: Average steady-state values of (a) the scaled end-to-end distance R_n, (b) the effective persistence length ℓ_p/ℓ, (c) the relative shape anisotropic κ, and (d) the nematic scalar order parameter $\lambda_Q^{\max}$ as functions of σ_0 for chains of length $N = 50$ and 100. In the case of $N = 50$, two different combinations of on/off rates giving the same value of $p_a = 1/6$ were used: $(k_{\mathrm{on}}, k_{\mathrm{off}}) = (100, 500)$ (blue triangles) and $(10, 50)$ (red squares). The simulation with $N = 100$ uses $(k_{\mathrm{on}}, k_{\mathrm{off}}) = (100, 500)$ (black circles).

We quantify this using the mean persistence length, which for a bead-rod chain can be defined as [148]

$$\frac{\ell_p}{\ell} = \frac{1}{2}\left(\frac{1+\xi}{1-\xi}\right), \quad \text{where} \quad \xi = \langle \mathbf{n}_i \cdot \mathbf{n}_{i+1} \rangle. \tag{3.16}$$

As shown in Fig. 3.4(b), the persistence length shows similar trends as the end-to-end

distance: it is independent of activity in the contractile systems, but shoots up with activity in extensile systems above the transition to stretched conformations.

Another measure of the mean polymer conformation is provided by the radius of gyration tensor $\mathbf{R}_G$, defined as

$$\mathbf{R}_G = \frac{1}{N} \sum_{i=1}^{N} (\mathbf{r}_i - \mathbf{r}_{cm})(\mathbf{r}_i - \mathbf{r}_{cm}), \tag{3.17}$$

where $\mathbf{r}_{cm}$ is the instantaneous center-of-mass position. Its eigenvalues α_1, α_2 and α_3, characterize the extent of the polymer mass distribution along its eigendirections, with a larger eigenvalue corresponding a net extension of the chain in the corresponding direction. These eigenvalues can be used to define a shape anisotropy parameter κ as

$$\kappa = 1 - 3\frac{\alpha_1\alpha_2 + \alpha_1\alpha_3 + \alpha_2\alpha_3}{(\alpha_1 + \alpha_2 + \alpha_3)^2}, \tag{3.18}$$

A straight linear polymer (e.g., $\alpha_1 = 1$, $\alpha_2 = \alpha_2 = 0$) has an anisotropy of $\kappa = 1$, whereas an isotropic or spherically symmetric configuration ($\alpha_1 = \alpha_2 = \alpha_3$) has an anisotropy of $\kappa = 0$. The dependence of κ on activity is depicted in Fig. 3.4(c). In contractile systems, the mean value of κ is independent of activity and relatively low at ≈ 0.3: this non-zero value is to the fact that instantaneous conformations on which we calculate κ are not perfectly isotropic due to fluctuations, even though on average the system shows no preferred direction. In the presence of extensile activity, anisotropy increase as the chains extend along the principal direction of the gyration tensor, with κ reaching nearly 1 for $N = 100$ at $\sigma_0 = 50$.

Finally, we also characterize global nematic alignment of chain segments by plotting in Fig. 3.4(d) the scalar nematic order parameter λ_Q^{max}, defined as the maximum eigenvalue of the mean nematic order tensor

$$\mathbf{Q} = \frac{1}{N-1} \sum_{i=1}^{N-1} \left(\mathbf{n}_i\mathbf{n}_i - \frac{\mathbf{I}}{3} \right), \tag{3.19}$$

and we note that $\lambda_Q^{\max}$ is in a range of 0 to $2/3$. Once again, we observe similar trends as function of activity, with no discernible effect of σ_0 in contractile systems, but a sharp increase of the maximum eigenvalue above the coil-stretch transition, especially in the case of long chains $(N = 100)$.

3.3.3 Coil-stretch transition: Phase diagram

We further characterize the dependence of the coil-stretch transition on system parameters in Fig. 3.5, where we consider extensile systems only. We systematically determine the location of the transition by considering the time evolution of the nematic scalar order parameter, which exhibits a positive growth only in simulations in which stretching occurs. The time evolution of $\lambda_Q^{\max}$ in one such case is plotted in Fig. 3.5(a), where a regime of linear growth is observed followed by a plateau.
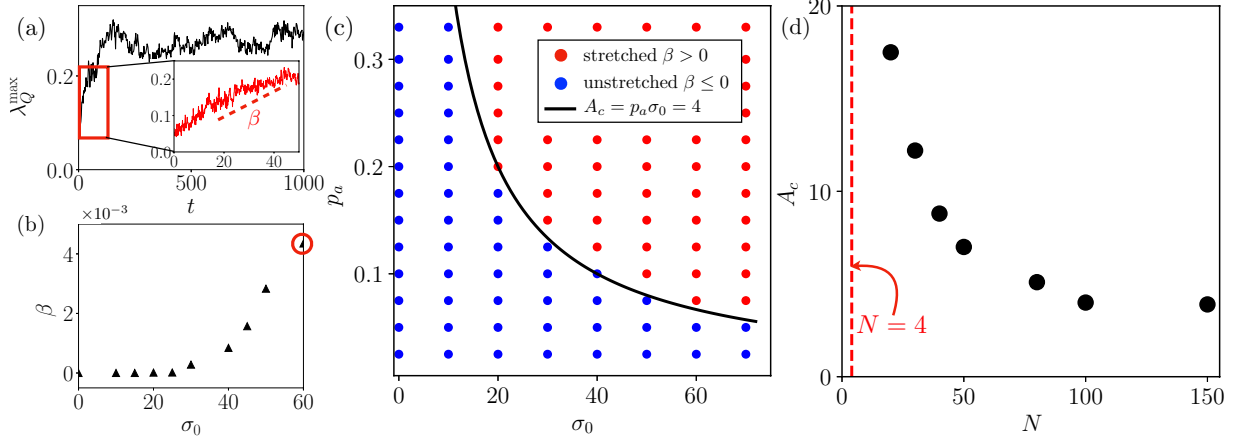
Figure 3.5: (a) Time evolution of the nematic scalar order parameter $\lambda_Q^{\max}$ in a simulation with $N = 100$, $p_a = 0.167$, and $\sigma_0 = 60$. Inset shows the initial regime of linear growth, from which we define the growth rate β. (b) Dependence of growth rate β on activity parameter A, showing the transition to stretching above a critical value. The red circle corresponds to the simulation shown in (a). (c) Phase diagram for coil-stretch transition in the (σ_0, p_a) plane. The boundary between the two domains is well captured by a curve of constant A (black curve). (d) Critical activity level for coil-stretch transition as a function of chain length N. The coil-stretch transition is only observed for chains of length $N \geq 4$.

56

A growth rate β can be computed during the initial regime, which is roughly zero for configurations that stay coiled but becomes positive when stretching occurs. This is illustrated in Fig. 3.5(b), where we plot β as a function of σ_0 for a fixed value of $p_a = 0.167$. The trends are similar to those found in Fig. 3.4, with a clear transition to stretching occurring a critical dipole strength of $\sigma_0 \approx 30$. Similar simulations were performed by varying both σ_0 and p_a, and the results are summarized in a phase diagram in Fig. 3.5(c) in the case $N = 100$, where we highlight parameter regimes where coiled and stretched configurations are observed. Expectedly, we find that the transition to stretching occurs for large values of either p_a (many dipoles) or σ_0 (stronger dipoles). We find that the transition is very well captured by a curve of constant $A = p_a \sigma_0$, with a critical value of $A_c \approx 4$ in the case shown in Fig. 3.5(c). The activity threshold A_c is length dependent, and is found to decay with N as shown in Fig. 3.5(d): indeed, a longer chain will carry more dipoles at fixed value of p_a. For intermediate chain lengths, we observe that $A_c \sim N^{-1}$, followed by apparent plateau for long chains. This suggests a transition governed by the parameter AN, which plays an analogous role as the Deborah number for the classic coil-stretch transition of flexible polymers in extensional flows. Interestingly, we find that the transition to spontaneous stretching only occurs for $N \geq 4$, a result that we explore further using a theoretical model in Sec. 3.3.4.

3.3.4 Theory for an active trimer

As observed in Fig. 3.5(d), $N = 4$ is the lower limit above which the polymer undergoes the coil stretch transition in our simulations. To understand this behavior, we further study the case of a trimer consisting of $N = 3$ beads using a theoretical based on a Fokker-Planck formulation. Denoting by $\mathbf{q}$ the generalized angular coordinates describing the configuration of the chain, the Fokker-Planck equation for the probability density

function $\psi(\mathbf{q}, t)$ is given by [149–151]

$$\frac{\partial \psi}{\partial t} + \frac{\partial}{\partial q_i} \left[\Gamma_{ij} \left(\sum_{n=1}^{N} u_k^a(\mathbf{r}_n) \frac{\partial r_{n,k}}{\partial q_j} \psi - \frac{k_B T}{\zeta} \sqrt{h} \frac{\partial}{\partial q_j} \left(\frac{\psi}{\sqrt{h}} \right) \right) \right] = 0, \qquad (3.20)$$

where index n refers to be bead number, and all other indices denote components of the various vector and tensor quantities, for which the Einstein summation convention applies. In Eq. (3.20), $\mathbf{\Gamma} = \mathbf{H}^{-1}$ and $h = \det(\mathbf{H})$ are defined in terms of the tensor

$$H_{ij} = \sum_{n=1}^{N} \frac{\partial \mathbf{r}_n}{\partial q_i} \cdot \frac{\partial \mathbf{r}_n}{\partial q_j}. \qquad (3.21)$$
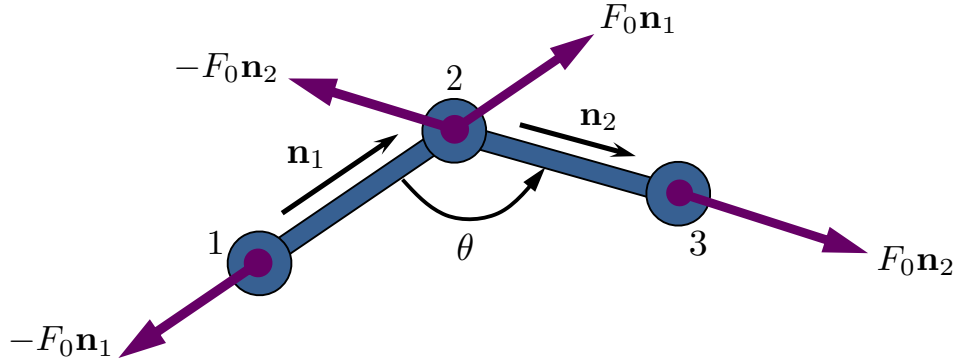
Figure 3.6: Schematic of an active trimer, where the internal coordinate of interest is the bond angle $\theta = \pi - \cos^{-1}(\mathbf{n}_1 \cdot \mathbf{n}_2)$.

In the case of interest where there is no external flow, the mean position and orientation of the chain simply undergo Brownian diffusion, and the only internal coordinate with a non-trivial probability distribution function is the angle $\theta = \pi - \cos^{-1}(\mathbf{n}_1 \cdot \mathbf{n}_2)$ as depicted in Fig. 3.6. Eq. (3.20) can simplified in this case. Setting the orientational flux to zero at steady state yields the simple differential equation

$$\ell^2 \dot{\theta}^a \psi - \frac{k_B T}{\zeta} \sqrt{h} \frac{\mathrm{d}}{\mathrm{d}\theta} \left(\frac{\psi}{\sqrt{h}} \right) = 0. \qquad (3.22)$$

where $\dot{\theta}^a$ is the deterministic angular velocity resulting from the flow induced the active

dipoles, and $h = \ell^4(4 - \cos^2\theta)$. Here, the probability density function is normalized as

$$\int_0^\pi \psi(\theta) \sin\theta \, \mathrm{d}\theta = 1, \tag{3.23}$$

where the factor of $\sin\theta$ comes from the solid angle in three dimensions.

For simplicity, we assume that both links are subject to permanent dipoles ($p_a = 1$). The angular velocity in that case can be calculated as

$$\dot{\theta}^a = \frac{1}{\sin\theta} (\dot{\mathbf{n}}_1 \cdot \mathbf{n}_2 + \mathbf{n}_1 \cdot \dot{\mathbf{n}}_2) = \frac{2}{\sin\theta} \mathbf{n}_1 \cdot \dot{\mathbf{n}}_2 \tag{3.24}$$

where

$$\dot{\mathbf{n}}_2 = \frac{1}{\ell}(\mathbf{I} - \mathbf{n}_2\mathbf{n}_2) \cdot \mathbf{u}^a(\mathbf{r}_3). \tag{3.25}$$

Upon substituting the expression for the active flow velocity at the location of bead 3,

$$\mathbf{u}^a(\mathbf{r}_3) = [\mathbf{G}(\mathbf{r}_3; \mathbf{r}_2) - \mathbf{G}(\mathbf{r}_3; \mathbf{r}_1)] \cdot F_0\mathbf{n}_1, \tag{3.26}$$

with $\mathbf{G}$ the Oseen tensor defined in Eq. (3.6), we obtain after simplifications

$$\dot{\theta}^a = \frac{F_0}{4\pi\mu\ell^2} \sin\theta \left[1 - \frac{3}{2\sqrt{2(1 - \cos\theta)}}\right]. \tag{3.27}$$

Inserting this expression into the flux balance Eq. (3.22) then yields the governing equation for $\psi(\theta)$,

$$\frac{3}{2}\left(\frac{a}{\ell}\right)\sigma_0 \sin\theta \left[1 - \frac{3}{2\sqrt{2(1 - \cos\theta)}}\right]\psi = \sqrt{4 - \cos^2\theta}\frac{\mathrm{d}}{\mathrm{d}\theta}\left(\frac{\psi}{\sqrt{4 - \cos^2\theta}}\right), \tag{3.28}$$

which is written is dimensionless form and involves both the dipole strength σ_0 and ratio a/ℓ of the bead hydrodynamic radius to the bond length.

In the passive case ($\sigma_0 = 0$), Eq. (3.28) is readily integrated as

$$\psi_p(\theta) = \psi_0\sqrt{4 - \cos^2\theta} \qquad (\sigma_0 = 0), \tag{3.29}$$

which is the classic solution for a rigid trimer [149], which peaks at and is symmetric about $\theta = \pi/2$; see Fig. 3.7. The prefactor is obtained from the normalization condition

59
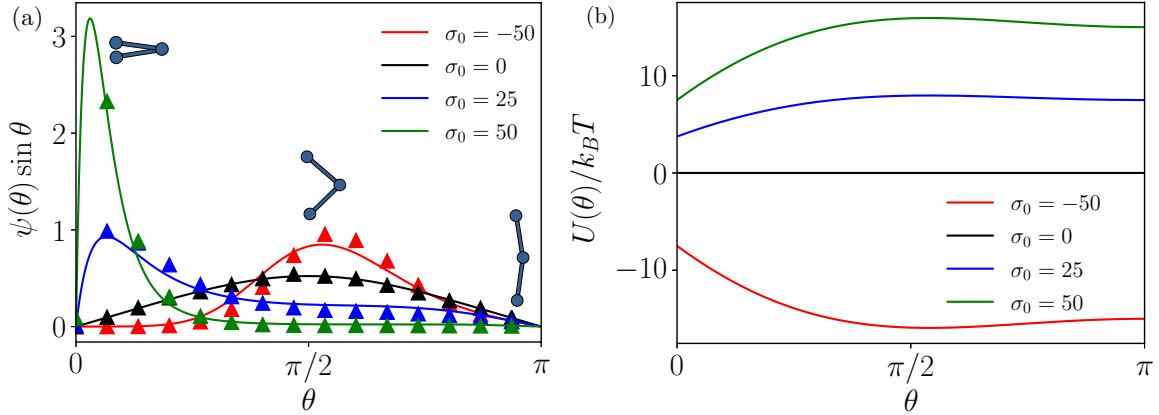
Figure 3.7: Probability density function $\psi(\theta)\sin\theta$ of the bond angle θ for a trimer with different levels of activity and for $a/\ell = 0.1$ (the factor of $\sin\theta$ arises from the solid angle in Eq. (3.23)). The plot compares the analytical solution of Eq. (3.30) (solid lines) with results from Langevin simulations (symbols).

Eq. (3.23) as $\psi_0 = (2\pi/3 + \sqrt{3})^{-1}$. When activity is present ($\sigma_0 \neq 0$), the solution of Eq. (3.28) for the distribution function becomes

$$\psi_a(\theta) = \psi_p(\theta) \exp\left[-\frac{3a\sigma_0}{2\ell}\left(\cos\theta + \frac{3}{2}\sqrt{2(1-\cos\theta)}\right)\right], \tag{3.30}$$

with a new normalization constant ψ_0 that now depends on $(a/\ell)\sigma_0$ and must be determined numerically. We find that dipolar activity modifies the equilibrium distribution $\psi_p(\theta)$ through a Boltzmann factor of the form $\propto \exp(-U(\theta)/k_{\mathrm{B}}T)$ where

$$\frac{U(\theta)}{k_{\mathrm{B}}T} = \frac{3a\sigma_0}{2\ell}\left(\cos\theta + \frac{3}{2}\sqrt{2(1-\cos\theta)}\right) \tag{3.31}$$

can be interpreted as an effective potential energy for self-alignment of the chain under its own active flow.

Figure 3.7(a) shows $\psi(\theta)\sin\theta$ as a function of θ for different values of σ_0, and compares the analytical solution of Eq. (3.30) with results from Langevin simulations. Good agreement is found between the two. As anticipated based on Fig. 3.5(d), we find that the behavior of the trimer is quite unlike that of longer chains: extensile trimers ($\sigma_0 > 0$) tend to remain in a folded configuration with $\theta \approx 0$, whereas contractile trimers

60

tend to stayed kinked with $\theta \approx \pi/2$. The propensity for the extensile trimer to remain folded can be understood by considering the potential energy in Fig. 3.7(b): in extensile cases with $\sigma_0 > 0$, the potential energy displays two minima at $\theta = 0$ and π, which both correspond to configurations with aligned dipoles. However, the minimum at $\theta = 0$ is significantly deeper, since the two dipoles are closer to one another and therefore interact more strongly in the folded state than in the unfolded state. This explains why the folded configuration is preferred in this case as seen in Fig. 3.7(a). This folded state, however, becomes much less likely in longer chains, as the links also experience tension forces from the other parts of the chain. Excluded volume interactions also decrease the likelihood of folded conformations.

3.4 Conclusions

We have performed Langevin simulations of model active polymers consisting of freely-jointed bead-rod chains decorated by stochastic force dipoles that drive long-ranged flows in the viscous suspending solvent. Depending on the type of dipole, significantly different dynamics were observed: fluid flows driven by contractile dipoles tend to create transient kinks in the chain, resulting in coiled conformations with enhanced fluctuations; on the other hand, the flow driven by extensile dipoles tends to align neighboring chains segments, leading to a spontaneous unfolding and stretching of the chain above a critical level of activity. The dynamics in the extensile case are reminiscent of the coil-stretch transition of passive polymer chains in extensional flows [147, 150]. However, the active coil-stretch transition uncovered here is spontaneous and does not require any external flow or forcing. Upon unfolding and stretching of the polymer, the aligned dipoles along the chain drive a macroscopic fluid flow with extensional symmetry that resists relaxation under thermal fluctuations and sustains the stretched conformation along an arbitrary

axis selected by random fluctuations. As demonstrated by our analysis, the transition to stretching occurs above a critical value of $Np_a\sigma_0$, which denotes the product of the mean number of dipoles Np_a along the chain with the dimensionless dipole strength σ_0. While most of our simulations neglected hydrodynamic interactions (other than those directly resulting from dipolar activity), we anticipate that a full characterization of the transition in the presence of hydrodynamic interactions may uncover yet richer behavior, such as conformation hysteresis near the transition point, which is known to occur in the case of the passive coil-stretch transition [152, 153].

The active polymer model used in this work was motivated by interphase chromatin, which is a flexible polymer known to be subject to ATP-powered enzymes such as RNA polymerase [120]. A detailed microscopic model for the local active stresses generated by these enzymes is still lacking, yet we expect to be able to coarse-grain them as dipoles [121], and past work has suggested that fluid-mediated interactions between these dipoles may be responsible for the coherent motions observed inside the cell nucleus during interphase [9]. Chromatin and its associated enzymes, however, cannot be extracted in vitro without major disruption to their structure and function, so that this system is hardly a good candidate for experimental validation of our model. Other synthetic systems, however, would be very well suited for that purpose. One example could consist of a flexible chain composed of bimetallic autophoretic rods [154], which can be designed to drive either extensile or contractile flows [155]. Such a chain of extensile rods should display the active coil-stretch transition, which could be externally controlled by addition or removal of chemical fuel such as hydrogen peroxide to the solution. This suggests novel designs for smart polymeric materials whose effective rheological, optical or thermal properties could be tuned reversibly by triggering the active coil-stretch transition on the microscale.

3.5 Acknowledgements

Chapter 4

Activity in the nucleus enhances segregation and compaction of heterochromatin

4.1 Introduction

Chromatin is the functional form of DNA in cells, and its structure, organization and dynamics control all aspects of DNA biology. The spatiotemporal organization of chromatin in the nucleus plays an essential role in nuclear processes such as gene transcription and genome replication, yet the fundamental biophysical principles and mechanisms underpinning its complex self-organization remain elusive. During interphase in differentiated cells, the genome undergoes large-scale compartmentalization into active and repressed states, thereby altering the availability of genes to transcription factors as a key mechanism for epigenetic gene regulation. Two major compartments of chromatin, heterochromatin and euchromatin, are spatially segregated inside the nucleus, with the transcriptionally active euchromatin remaining loosely packed while predominantly

silent genes are condensed into heterochromatin regions. In conventional nuclei, heterochromatin is distributed throughout the nucleus but concentrates predominantly in the periphery [156, 157], where it tends to bind to the lamin network lining the interior of the nuclear envelope. In the absence of chromatin–lamina interactions, heterochromatin is instead found to concentrate near the center of the nucleus, and this inverted configuration occurs in certain photoreceptor cells of nocturnal mammals [52]. The biochemical basis of heterochromatin condensation is linked to the methylation of histone tails and binding of heterochromatin protein 1 (HP1) to nucleosomes. Bound HP1 further oligomerizes and bridges nucleosomes from chromatin regions in close spatial proximity, resulting in the compaction and repression of silent genes [45–49]. This compaction has been hypothesized to involve liquid–liquid phase separation by HP1 [50, 51].

Recent modeling efforts aimed at explaining chromatin segregation have focused on equilibrium simulations that describe chromatin as a block copolymer, with euchromatin and heterochromatin chain segments exhibiting different affinities. Using Brownian dynamics, Falk *et al.* [6] found that heterochromatin tends to aggregate and compact into a dense region in the center of the nucleus. Similar findings were made by MacPherson *et al.* [5] using Monte-Carlo simulations in which discrete HP1 proteins preferentially bound to heterochromatin and further oligomerized to bridge between nucleosomes. Subsequent studies based on the same models [52, 53] showed that non-specific attractive interactions with the nuclear envelope result in preferential accumulation of heterochromatin in the nuclear periphery consistent with observations in conventional nuclei, confirming that binding to the nuclear lamina plays a key role in the spatial organization of heterochromatin.

These models, however, only considered equilibrium statistics and neglected the role played by ATP-powered active processes in the kinetics of heterochromatin formation and its final morphology. The importance of activity in chromatin dynamics was first dis-

covered in experiments by Zidovska *et al.* [120], who developed displacement correlation spectroscopy to quantify chromatin positional dynamics simultaneously across the entire nucleus in live cells by imaging of histones H2B-GFP. These observations revealed that chromatin moves coherently within large regions of 3–5 μm in size and lasting over several seconds. These correlated motions were found to be ATP-dependent and independent of the cytoplasmic cytoskeleton. Perturbation of major nuclear ATPases such as DNA polymerase, RNA polymerase II and topoisomerase II caused local displacements to increase, but completely blocked coherence.

Motivated by these experiments, Zidovska *et al.* [121] proposed a hydrodynamic theory of chromatin dynamics that coarse-grained the action of ATPases into two basic types of active events: vector events that describe force dipoles generated by nuclear enzymes such as polymerases and helicases, and scalar events corresponding to the local de/condensation of chromatin caused by chromatin remodelers. This mean-field continuum theory predicts that dipolar activity is responsible for large-scale coherent motions [120, 121]. Alternative hydrodynamics-free approaches to modeling activity have been developed which use a 3D-conformational space of the chromatin fiber emerging from a quasi-equilibrium energy landscape [122]. Such an energy landscape was generated by Langevin dynamics at an effective temperature as a model for activity within the nucleus. Another hydrodynamics-free model, informed by Hi-C data of human chromosomes, described chromatin as a heteropolymer to explore the spatiotemporal dynamics of interphase chromosomes [123, 124]. Chromatin activity was also mimicked by an isotropic noise. Both models successfully recapitulated large-scale coherence of chromatin motions.

In recent work, Saintillan, Shelley and Zidovska [9] built upon the concept of vector events to develop a computational model of active chromatin hydrodynamics that accounts for the role of ATP-driven processes. A long flexible polymer confined inside a spherical

cavity and subjected to stochastic force dipoles was simulated. These force dipoles generated fluid flows in the nucleoplasm, which in turn drove local nematic alignment of the chain. This positive feedback occurred only for extensile dipoles and resulted in large-scale coherent motions by a mechanism similar to the generic bend instability of extensile active nematics [158–160]. These simulations assumed a homopolymer chain, thus no macroscopic self-organization was observed beyond the alignment induced by hydrodynamic interactions.

Here, we extend this computational approach to illuminate the role of dipolar activity and nucleoplasmic flows in the dynamics of chromatin phase segregation in the differentiated cell nucleus. We perform large-scale coarse-grained simulations of an entire model nucleus containing multiple chromosomes immersed in a viscous nucleoplasm. The chromosomes are modeled as diblock copolymers composed of segments of active euchromatin subject to dipolar activity, alternating with segments of silent heterochromatin subject to inter- and intra-chain crosslinking. Our numerical results underscore the role of activity-driven coherent motions and nucleoplasmic flows on the compaction and spatial distribution of heterochromatin in differentiated cells.

4.2   Coarse-grained chromatin model

We simulate a system of M_c confined polymers representing individual chromosomes inside the interphase nucleus (Fig. 4.1). The nuclear envelope, which encloses the chains, is modeled as a prolate spheroidal cavity with bounding surface S of eccentricity e and equivalent radius R_s, and is filled with a viscous Newtonian nucleoplasm with viscosity η. Each chromosome is coarse-grained as an active Zimm bead-spring chain composed of N_b beads of hydrodynamic radius a_h connected by finitely extensible elastic springs. In this coarse-grained description, a bead should be viewed as a mesoscopic chromatin sub-

domain containing a large number of nucleosomes and associated proteins at a resolution of ~ 100 kbp. As depicted in Fig. 4.1, each chromosome further consists of alternating blocks of heterochromatin and euchromatin domains (HCDs and ECDs, respectively), with a fraction α_c of heterochromatin.
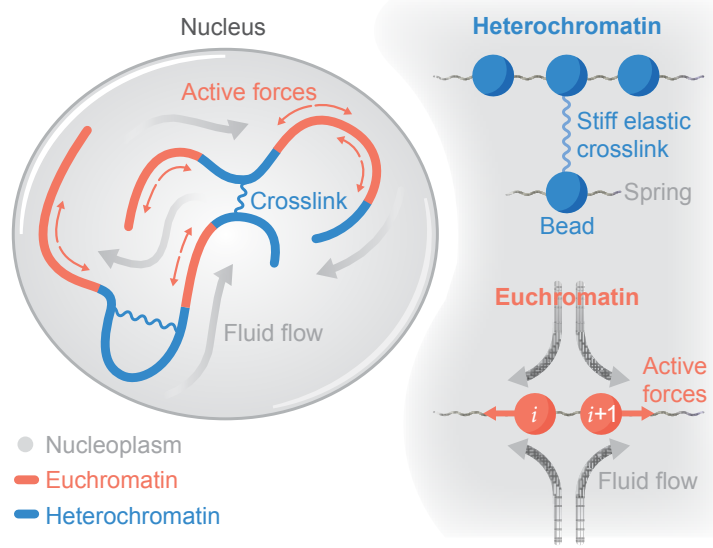
Figure 4.1: Model schematic: M_c bead-spring polymer chains representing individual chromosomes are confined inside a spheroidal nuclear envelope. Heterochromatic domains (HCDs) can form inter- and intra-chromosomal crosslinks, whereas euchromatic domains (ECDs) are decorated with active force dipoles that drive nucleoplasmic flows.

Transcriptionally active euchromatin experiences microscopic active stresses generated by the ATP-powered action of nuclear enzymes such as polymerases, helicases, and topoisomerases as they perform their functions. We model these stresses in terms of stochastic active force dipoles distributed along ECDs and applied to the viscous fluid in which they drive an active flow [9]. On the other hand, the silent HCDs are characterized by the presence of inter- and intra-chain crosslinks as a macroscopic model for the binding interactions between the heterochromatin protein 1 (HP1) and the trimethylated histone tails [5, 46, 161].

The position $\mathbf{x}_i(t)$ of bead $i = 1, ..., N$ (where $N = N_b \times M_c$) is governed by the

overdamped Langevin equation [69]

$$\frac{\mathrm{d}\mathbf{x}_i}{\mathrm{d}t} = \frac{1}{\zeta}\mathbf{F}_i(t) + \mathbf{u}(\mathbf{x}_i, t) + \boldsymbol{\xi}_i(t). \tag{4.1}$$

The first term describes transport under the net deterministic force on bead i, to be specified below, where $\zeta = 6\pi\eta a_h$ is the corresponding friction coefficient. The second term captures advection of the bead by the viscous flow inside the nucleus, with contributions from activity as well as hydrodynamic interactions resulting from viscous drag on the beads. Finally, the last term captures Brownian displacements and is calculated to satisfy the fluctuation–dissipation theorem.

The net deterministic force $\mathbf{F}_i$ on bead i accounts for entropic spring tensions, crosslink forces as well as excluded volume interactions between neighboring beads:

$$\mathbf{F}_i = \mathbf{F}_i^s + \mathbf{F}_i^c + \mathbf{F}_i^e. \tag{4.2}$$

Entropic spring forces $\mathbf{F}_i^s$ are modeled using the FENE spring law [116], and excluded volume forces $\mathbf{F}_i^e$ are captured using a soft repulsive potential; see Appendix B for details. Crosslink forces $\mathbf{F}_i^c$ are used to model binding interactions between beads inside HCDs. These crosslinks represents HP1 binding to the methylated K9 residue of histone H3 (H3K9me3), an established marker of the transcriptionally silent heterochromatin associated with high chromatin density and low gene expression levels. These binding interactions, which can occur inter- or intra-chain, are also captured using FENE springs but with a stiffer spring constant. These links can form stochastically between pairs of heterochromatic beads that are within a certain cutoff radius a_c of one another and are both in an activated state, where activation occurs stochastically as a Poisson process with rate k_{on}^c. Each bead can form at most one crosslink, and crosslinks are permanent once formed.

A key aspect of our model is the inclusion of hydrodynamic flows induced by the

activity of ATP-powered enzymes and from interactions between chain segments. Following our past work [9], microscopic active stresses are coarse-grained in the form of active dipolar forces applied to the fluid along euchromatic portions of the chromosomes and occur on the scale of one chain link. Specifically, active dipoles are switched on and off stochastically as a Poisson process with rates k_{on}^a and k_{off}^a, which set the probability $p_a = k_{on}^a/(k_{on}^a + k_{off}^a)$ for a link to be active. When a euchromatic link i is in the on–state, two equal and opposite forces are applied to the viscous nucleoplasm at the positions of the end beads:

$$\mathbf{F}_i^a = -f^a \hat{\mathbf{n}}_i(t), \quad \mathbf{F}_{i+1}^a = f^a \hat{\mathbf{n}}_i(t), \tag{4.3}$$

where $\hat{\mathbf{n}}_i = \mathbf{n}_i/n_i$ is the unit vector pointing from bead i to $i+1$ obtained from the connector $\mathbf{n}_i = \mathbf{x}_{i+1} - \mathbf{x}_i$ between the two beads. The pair of forces constitutes a dipole of magnitude $\sigma = f^a n_i$, which is extensile ($\leftarrow\rightarrow$) for $\sigma > 0$ and contractile ($\rightarrow\leftarrow$) for $\sigma < 0$. In simulations, we fix f^a, meaning that the actual dipole strength fluctuates with the distance n_i between the beads. We define a characteristic dipole strength as $\sigma_0 = f^a \ell_s$, where ℓ_s is the equilibrium length of an isolated passive spring.

Both passive and active forces contribute to the nucleoplasmic flow field $\mathbf{u}$ and corresponding pressure p, which satisfy the Stokes momentum equation

$$-\nabla p + \eta \nabla^2 \mathbf{u} = \sum_{i=1}^{N} \left(\mathbf{F}_i + \mathbf{F}_i^a\right) \delta(\mathbf{x} - \mathbf{x}_i) \tag{4.4}$$

along with the incompressibility constraint $\nabla \cdot \mathbf{u} = 0$. In Eq. (4.4), active forces on the right-hand side are only included for beads that are in the active state. The velocity field is subject to the no-slip condition $\mathbf{u} = \mathbf{0}$ on the surface of the nuclear envelope and is obtained using an accelerated algorithm based on the kernel-free fast-multipole method, allowing us to simulate large systems over long periods of time. In the following, we present results in dimensionless form based on characteristic thermal (equilibrium) scales. Further details of the computational methods and scalings are provided in Appendix B.

4.3 Results

In this section, we consider simulations of $M_c = 23$ identical chains (or chromosomes) of 1305 beads for a total of $\sim$ 30k beads, meaning that each bead represents $\sim$ 1000 of the $\sim$ 30M nucleosomes in the human genome. Each chromosomal chain contains four equally spaced linear HCDs that in total occupy a fraction $\alpha_c \approx 30\%$ of each chromosome. Recall that crosslinks can form within and between heterochromatic domains, but not with or within the complementary ECDs. Each chromosome is first prepared as a confined random walk, and then all are distributed within the nucleus to establish distinct chromosomal territories. This system is then equilibrated under Brownian fluctuations and excluded volume forces to establish initial data.

4.3.1 Dynamics of heterochromatin segregation

Figure 4.2 shows the results of two long-time simulations proceeding from identical initial data (top row). In the first case, the ECDs are entirely passive ($\sigma_0 = 0$, middle row), and the dynamics largely results from crosslinks forming within and between HCDs. In the second case, the ECDs are instead active ($\sigma_0 > 0$, bottom row), being stochastically populated with extensile dipoles.

In the passive case, the chromosomes roughly maintain their initial spatial territories (Fig. 4.2(a)), with only slight mixing, mainly due to thermal fluctuations, taking place near their boundaries. The stochastically nucleating crosslinks, being long-lived, have led progressively to crosslink-rich regions (Fig. 4.2(b)). These form a loose network that spans the entire system and alternates with crosslink-free euchromatin. However, the dynamics of crosslinking, together with any attendant change in the mechanics of the chromatin in response to thermal fluctuations and excluded volume forces, has not led to any large-scale rearrangements of chromosomal or heterochromatic domains. We suspect that, being

rapid in comparison to rearrangements by thermal effects, crosslinking may be rigidify-ing the system, leading to fewer opportunities for crosslinking between distal HCDs. At any rate, heterochromatin is distributed across the nucleus with approximate uniformity, corresponding to the initial placement of the HCDs; see Fig. 4.2(c).
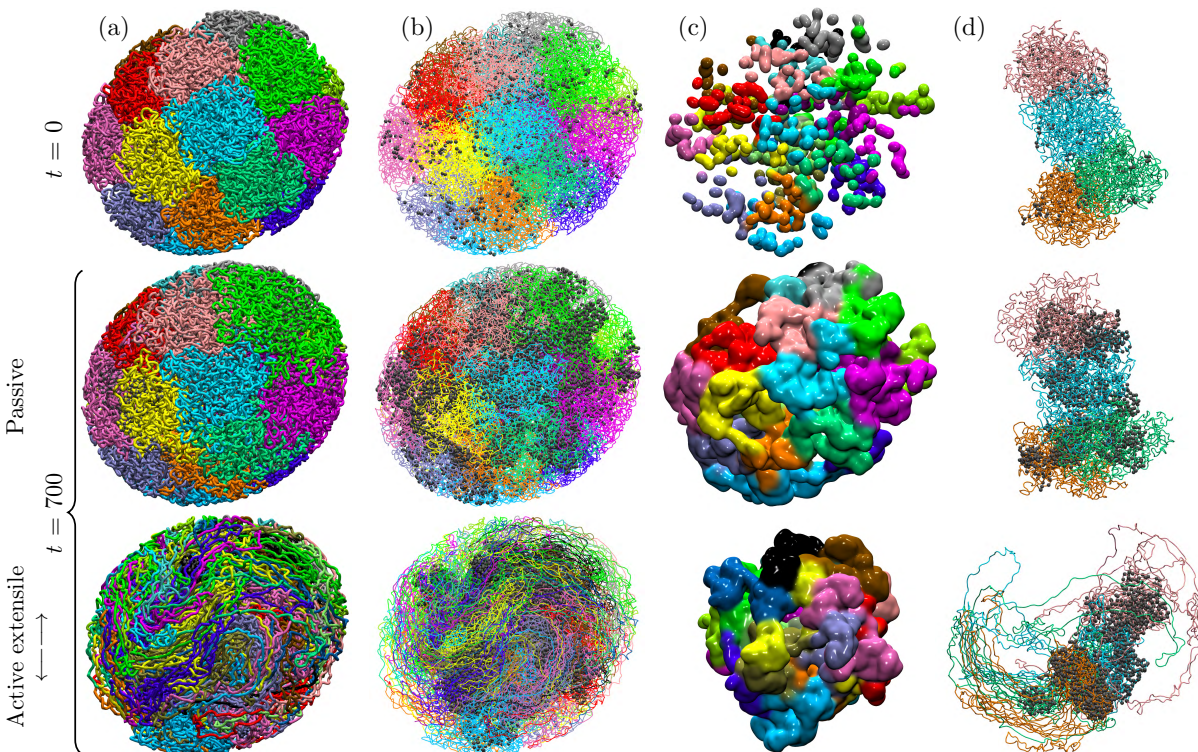
Figure 4.2: Long-time evolution of chromatin in simulations of two systems, one with passive euchromatin ($\sigma_0 = 0$) and another with active euchromatin (extensile, $\sigma_0 = 30$). Top row: initial system configuration at $t = 0$, which is identical in both simulations; second and third rows: system configurations at dimensionless time $t = 700$. The four columns show, from left to right: (a) the full chromatin system, with colors corresponding to distinct chromosomes; (b) the crosslinks within and between HCDs, shown as grey beads and overlayed on top of the chains; (c) the location of heterochromatic regions (HCRs), defined distinctly from heterochromatic domains as regions in space where the crosslink density exceeds 50% of its maximum value, and colored by chain membership; and (d) a subset of four chromosomes and associated crosslinks.

The dynamics and distribution of heterochromatin is very different for active eu-chromatin. There, extensile dipoles in ECDs drive large-scale coherent flows that draw

72

neighboring chain sections into alignment while mixing chromosomal territories. As a consequence of these active flows, the morphology of crosslinked heterochromatic regions (HCRs, defined distinctly from HCDs as the regions in space where the crosslink density exceeds 50% of its maximum value) is also quite different: mixing indeed facilitates crosslink formation between distinct HCDs, resulting in a more compact crosslinked network that progressively densifies near the center of the nucleus. These distinct morphologies are especially visible in Fig. 4.2(c), where we show the spatial boundary of HCRs. They have a much more compact and dense structure in the active case, with most of the active euchromatin expelled from the center towards the nuclear envelope. Snapshots of four individual chromosomes are also shown in Fig. 4.2(d) and further highlight the role of active nucleoplasmic flows that promote the compaction of heterochromatin while opening up and stretching active euchromatic chain segments.

We further quantify the spatiotemporal evolution of the system in Fig. 4.3. The migration of heterochromatin towards the nucleus center in the active case is evident in Fig. 4.3(a,left), showing the time evolution of the standard deviation $d = \sqrt{\langle |\mathbf{x}|^2 \rangle}$ of the polymer mass distribution normalized by the equivalent nuclear radius $R_s = 28$, for both ECDs and HCDs. While the spatial distribution of euchromatin shows only a minor shift towards the boundary, heterochromatin is found to concentrate near the center of the nucleus in the active extensile case, as evidenced by the decay of d_{hcd} with time and corresponding growth of the migration offset defined as $\Delta = d_{\mathrm{ecd}} - d_{\mathrm{hcd}}$. This inward migration is also accompanied by an increase in chromatin number density (both hetero- and euchromatin) as shown in Fig. 4.3(a,right), where we define $\rho_{\mathrm{hcr}} = N_{\mathrm{hcr}}/V_{\mathrm{hcr}}$ as the ratio of the number of beads of any type contained in the heterochromatic regions identified in Fig. 4.2(c) over the corresponding volume. In the absence of activity ($\sigma_0 = 0$), the number density remains close to the average number density of the system, whereas it

increases significantly when extensile dipoles are applied along ECDs ($\sigma_0 > 0$).
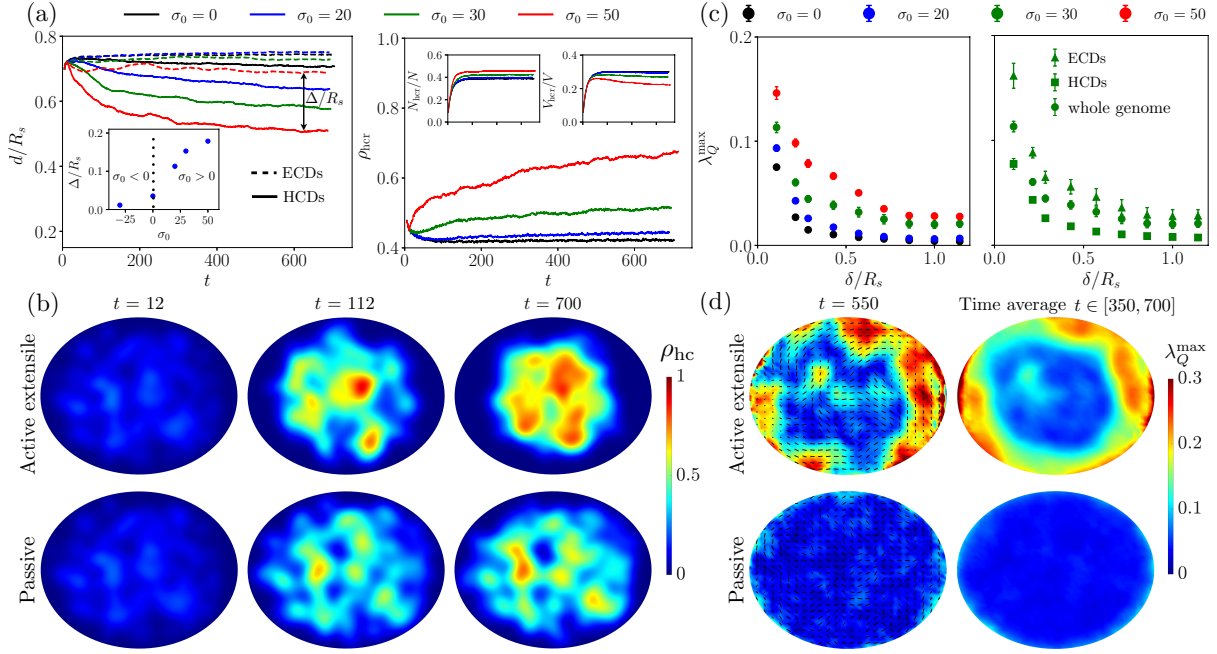
Figure 4.3: (a) Left: Standard deviation $d = \sqrt{\langle |\mathbf{x}|^2 \rangle}$ of the polymer mass distribution normalized by the equivalent nucleus radius R_s for ECDs and HCDs as functions of time, where HCDs are seen to migrate towards the center of the system. The inset shows the migration offset, defined as $\Delta = d_{\mathrm{ecd}} - d_{\mathrm{hcd}}$, at steady state as a function of activity σ_0. Right: Mean density ρ_{hcr} of HCRs (see Fig. 4.2(c)). Insets show the fraction of the number of beads contained in HCRs, as well as the fraction of the total volume that they occupy. (b) For the simulations in Fig. 4.2, time snapshots of the heterochromatin density field in a plane containing the major axis of the nucleus, for the active euchromatin case ($\sigma_0 = 30$, top row), and the passive euchromatin case ($\sigma_0 = 0$, bottom row). (c) Left: nematic order parameter $\lambda_Q^{\max}$, averaged over spheres of radius δ at late times, for various levels of activity σ_0. Right: nematic order parameter for ECDs, HCDs, and for the whole genome, in simulations with $\sigma_0 = 30$. (d) For the same simulations as shown in Fig. 4.2, the structure of nematic alignment in a plane containing the major axis of the nucleus, for the active euchromatin case ($\sigma_0 = 30$, top row) and the passive euchromatin case ($\sigma_0 = 0$, bottom row). The colormap is of the scalar nematic order parameter, while black segments depict the nematic director projected onto the viewing plane. The left column shows a snapshot at $t = 550$, whereas the right column shows a time average for $t \in [350, 700]$.

As shown by the insets in Fig. 4.3(a,right), this density increase is due to both an increase in N_{hcr} and a decrease in V_{hcr}, suggesting that activity not only drives a spatial

compaction of HCDs over time, but also causes these compacting regions to recruit and trap more ECD fragments during compaction. Spatial maps of the heterochromatic density in a plane cross-section are shown in Fig. 4.3(b) and confirm these findings: crosslinked regions are relatively sparse and evenly distributed across the nucleus in the passive case, but concentrate into a dense and compact structure near the center of the nucleus with extensile activity. The case of contractile activity (not shown) is qualitatively similar to the Brownian case, with no discernible phase segregation.

As observed in the snapshots of Fig. 4.2, euchromatic extensile activity not only facilitates the segregation and compaction of crosslinked heterochromatin, it also induces its own stretching and alignment as first predicted in our past work [9]. We quantify this alignment by calculating the tensorial nematic order parameter $\mathbf{Q} = \langle \hat{\mathbf{n}}\hat{\mathbf{n}} - \mathbf{I}/3 \rangle_\delta$, where $\hat{\mathbf{n}} = \mathbf{n}/|\mathbf{n}|$ is the unit director between successive beads inside the chains, and the average is performed over spherical domains of radius $\delta = 5$. Its largest eigenvalue $\lambda_Q^{\max} \in [0, 2/3]$ defines the scalar nematic order parameter and is a measure of the degree of euchromatin alignment on the length scale δ. Fig. 4.3(c,left) shows $\lambda_Q^{\max}$ as a function of δ for different levels of activity. In passive Brownian simulations ($\sigma_0 = 0$), nematic alignment is negligible except on short length scales ($\delta/R_s \lesssim 0.2$) where it is induced by steric interactions between neighboring chain segments. In the presence of extensile activity, the nematic order significantly increases on all scales as active force dipoles within ECDs induce local flows that draw nearby chain segments in alignment. This emergent alignment increases the spatial coherence of the active dipolar flows via a positive feedback loop, generating nematic order on length scales that greatly exceed the scale of one dipole. The precise mechanism for these coherent flows was discussed in our past work [9] and is similar to the generic instability occurring in various other active nematic systems [159, 160, 162]. As shown in Fig. 4.3(c,right), nematic alignment primarily occurs among ECDs where

dipolar activity takes place, as these sections of the chromatin are not crosslinked and therefore relatively free to reorganize in response to hydrodynamic flows. Alignment inside HCDs is much weaker and comparable to the passive case, as the internal structure of heterochromatin is strongly constrained by the presence of crosslinks. These observations are amplified in Fig. 4.3(d), which show spatial maps of the scalar order parameter and dominant alignment direction in a plane across the system. Nematic alignment is strong in euchromatic regions on the periphery of the nuclear interior, and tends to conform to the system boundary. These features remain present in the time-averaged nematic order parameter map, where the average was performed over $t \in [350, 700]$. The strong heterogeneity of the average map on this time scale suggests long-lived internal dynamics in the system, despite its very dynamic nature on short time scales.

In summary, our results underscore the central role of ATP-powered activity, taking place along ECDs, in determining the structure, placement and density of HCRs as they form inside the nucleus. We find that activity enhances the compaction of HCRs and the trapping of euchromatic fragments within, relative to the passive case, while creating large-scale nematic alignment outside of HCRs where ECDs are largely unconstrained and free to align with themselves and with boundaries. The mechanistic origin of this complex organization lies in the emergent stress fields – both active and passive – and attendant nucleoplasmic flows, which we now analyze.

4.3.2 Active stress and hydrodynamic flows

The dynamics of heterochromatin compaction and euchromatin nematic ordering are tightly linked to the hydrodynamic flows driven by active stresses and the resulting elastic stresses they generate inside the chains. We first analyze the internal stress distributions in Fig. 4.4(a), showing maps of the radial (Σ_{rr}) and shear ($\Sigma_{r\theta}$) components of

the active and tensile stress tensors in a plane across the nucleus, where (r, θ) are polar coordinates in that plane. The distribution of active dipoles along euchromatin results in an effective active stress [163, 164] that can be defined, based on the Irving–Kirkwood formula [165], as

$$\mathbf{\Sigma}^a(r, \theta) = \frac{1}{V_\delta} \sum_{\substack{\text{active} \\ \text{links}}} -\sigma_0 n_i (\hat{\mathbf{n}}_i \hat{\mathbf{n}}_i - \mathbf{I}/3), \tag{4.5}$$

where the sum is over all active links inside the local averaging volume V_δ, taken to be a sphere of radius $\delta = 5$. Similarly, the tensile stress is calculated as a local average over the FENE springs comprising the chromatin and crosslinks as

$$\mathbf{\Sigma}^s(r, \theta) = \frac{1}{V_\delta} \sum_{\text{springs}} \frac{H_c n_i^2}{1 - (n_i/n_0)^2} (\hat{\mathbf{n}}_i \hat{\mathbf{n}}_i - \mathbf{I}/3). \tag{4.6}$$

In the active extensile case ($\sigma_0 > 0$), active stresses are dominant in the periphery of the nucleus where euchromatin is primarily located and organized, and their distribution closely follows that of the nematic tensor in Fig. 4.2(d). Indeed, in the mean-field limit, the active stress of Eq. (4.5) can be approximated as $\mathbf{\Sigma}^a \approx -\rho_a \sigma_0 \langle n_a \rangle \mathbf{Q}$ where ρ_a is the local number density of active links and $\langle n_a \rangle \sim O(1)$ is the mean length of active links, which is activity dependent. In simulations with $\sigma_0 = 30$, we measure $\langle n_a \rangle \approx 1.3$. As shown by Fig. 4.4(a), a strong positive radial stress Σ_{rr}^a (similar to a negative active pressure) exists near the boundary and is consistent with the nematic alignment of the active extensile euchromatin chain segments along the boundary as found in Fig. 4.2(d). An active shear stress $\Sigma_{r\theta}$ is also observed near the boundary, albeit less intense and not uniformly distributed, with both $\Sigma_{r\theta} > 0$ and < 0 over distinct euchromatic regions. As is evident in Fig. 4.4(a), the response of the elastic chromatin chain network to dipolar activity involves an oppositely signed tensile stress $\mathbf{\Sigma}^s$ with radial and shear components that closely mirror the active stress distribution.
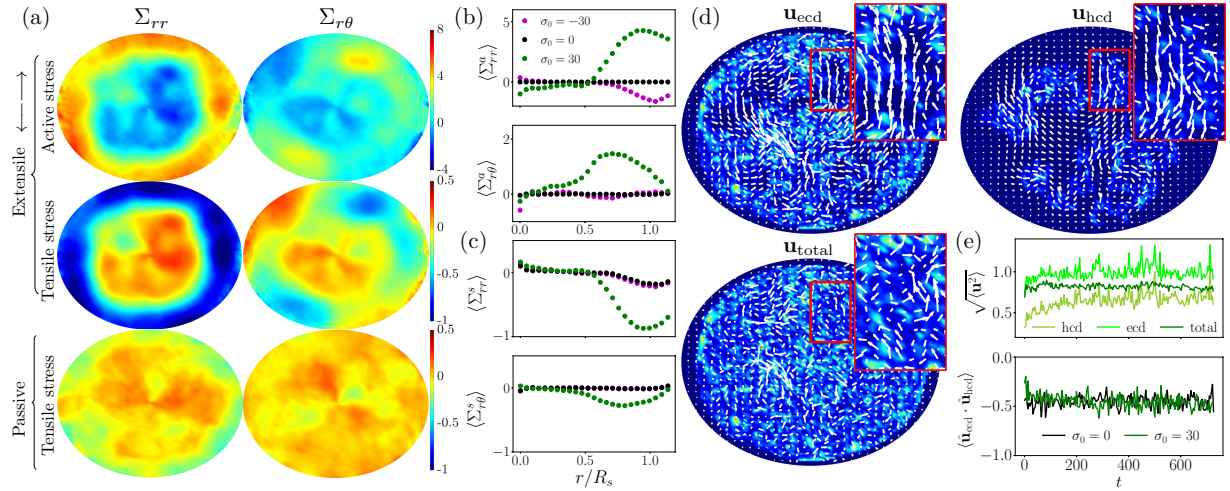
Figure 4.4: Analysis of the stress and flow fields: (a) Stress field exerted by dipolar active forces (first row) and internal tensile forces (second and third rows) in a plane containing the major axis of the nucleus, for the active euchromatin case (extensile, $\sigma_0 = 30$, top two rows) and the passive euchromatin case ($\sigma_0 = 0$, bottom row). The two columns show the radial (Σ_{rr}) and shear ($\Sigma_{r\theta}$) components of the stress averaged over $t \in [350, 700]$, where (r, θ) are polar coordinates in the plane. (b,c) Radial variation of active (b) and tensile (c) stress components averaged over the azimuthal direction for extensile ($\sigma_0 = 30$), passive ($\sigma_0 = 0$) and contractile ($\sigma_0 = -30$) systems. (d) Snapshots of the disturbance flows induced by deterministic forces along ECDs ($\mathbf{u}_{\mathrm{ecd}}$) and HCDs ($\mathbf{u}_{\mathrm{hcd}}$), as well as total disturbance flow ($\mathbf{u}_{\mathrm{total}} = \mathbf{u}_{\mathrm{ecd}} + \mathbf{u}_{\mathrm{hcd}}$), for an active extensile system with $\sigma_0 = 30$. The colormap shows the magnitude of the force distribution, and the vector plot shows the projections of the velocity field in a plane containing the major axis of the nucleus. Insets show zoomed-in regions where the flows induced by euchromatin and heterochromatin forces clearly oppose one another. (e) Top: Temporal evolution of the root mean square velocity $\sqrt{\langle \mathbf{u}^2 \rangle}$, showing the stronger flow induced by the euchromatin forces due to the presence of active dipole forces. Bottom: Time evolution of the correlation between the directions of the euchromatin and heterochromatin velocity fields, defined as $\langle \hat{\mathbf{u}}_{\mathrm{ecd}} \cdot \hat{\mathbf{u}}_{\mathrm{hcd}} \rangle$ where $\hat{\mathbf{u}} = \mathbf{u}/|\mathbf{u}|$, showing a strong negative correlation. These panels use the data from the simulations in Fig. 4.2.

This indicates that the fluid flows driven by active stresses tend to stretch and shear the chromatin network resulting in the observed tensile stress. In the passive system, there are no active stresses and the tensile stress distribution shows no clear structure except very close to the system boundary where weak alignment occurs due to steric effects.

These various findings are summarized in Fig. 4.4(b,c) showing the radial dependence of the various stress contributions in extensile, passive, and contractile systems. In all cases, average stresses are quite weak inside heterochromatin ($r/R_s < 0.5$) but display a peak near $r/R_s \approx 0.7 - 0.9$ where active stresses in extensile systems dominate the tensile stresses they induce inside the chain. With contractile activity, active stresses are of the opposite sign and are much weaker in magnitude due to the lack of nematic ordering in that case, other than very close to the envelope.

Figure 4.4(d) shows typical snapshots of the disturbance flows fields in the active extensile case. To analyze the distinct contributions of euchromatin and heterochromatin chain segments, we display separately the two flow fields induced by each type of chromatin (euchromatin and heterochromatin) as well as their sum, which is the net flow experienced by the system. The nucleoplasmic flow induced by euchromatin, which is distributed throughout the system, is found to be the strongest as a result of the active stresses present along these chain segments and is characterized by jets and swirls with mesoscale coherence. On the other hand, heterochromatin is primarily localized near the center of the system, and the disturbance flows it exerts are strongest there, where they are found to oppose the active flow driven by euchromatin. This is especially visible in the insets in Fig. 4.4(d), and is consistent with the discussion of stresses above: active flows tend to stretch and deform the heterochromatin network, which responds by developing tensile forces that oppose the flow. The net nucleoplasmic flow in the system, shown in the third panel of Fig. 4.4(d), is the sum of the two and indeed appears weaker and less coherent than the flow induced by euchromatin alone. This damping of active flows is indicative of hydrodynamic screening by the passive heterochromatic regions, which act as a porous elastic network. These findings are confirmed in Fig. 4.4(e), where we find that the root mean square velocity of the total flow falls between those of the contributions

from euchromatin and heterochromatin, and that the directions of these two velocity contributions tend to oppose one another: $\langle \hat{\mathbf{u}}_{\text{ecd}} \cdot \hat{\mathbf{u}}_{\text{hcd}} \rangle < 0$, where $\hat{\mathbf{u}} = \mathbf{u}/|\mathbf{u}|$. Interestingly, the same negative correlation exists in the passive case, even though motion in that case is purely thermal and thus spatially uncorrelated and much weaker. In summary, we find that the segregation of chromatin into dense HCRs surrounded by nematically aligned euchromatin occurs concomitantly with the development of stress fields inside the nucleus, which are strongest outside of HCRs and involve opposing contributions from activity and internal tensile forces. The resulting fluid flows are coherent on large length scales and show evidence of hydrodynamic screening by the crosslinked HCR networks. These flows, together with crosslinking interactions, result in dynamic, yet highly structured chromatin conformations whose impact on genome organization we now examine.

4.3.3   Hi-C proximity maps

Genome interactions at different length scales can be quantified in terms of the proximity between pairs of loci along the chromatin strand [24, 44]. The interactions between chromosomes 1 and 4, as estimated through proximity or near-contact, are represented as a heat map (or Hi-C map) in Fig. 4.5, with varying color intensity ranging from red to white to differentiate between regions of high/low proximity, respectively (see Appendix B.5 for details of the method used to calculate Hi-C maps). The lower diagonals in Fig. 4.5(a,b) show snapshots at a late time for a passive ($\sigma_0 = 0$) and active euchromatin simulation ($\sigma_0 = 30$), respectively, whereas the upper diagonals show time averages over $t \in [350, 700]$ for the same simulations. The blue colored segments along the axes highlight the location of the HCDs, while the green colored dots along the diagonal label portions of the genome that are spatially located inside the HCRs identified in Fig. 4.2(c). The relative size of these green high-interaction regions exceeds that of the HCDs due to chain connectiv-

ity, which ensures that proximal genomic segments become trapped inside HCRs as the permanent crosslinks form and compact the chain locally.
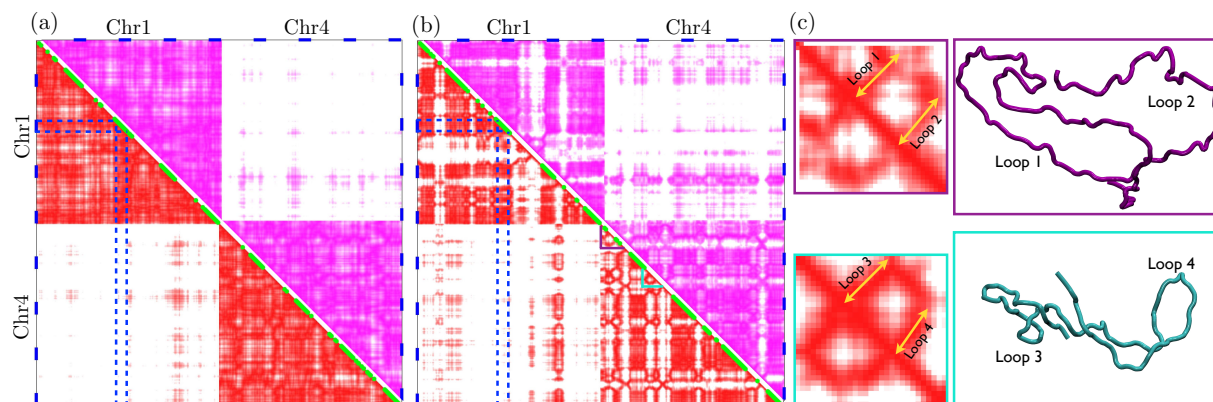
Figure 4.5: Hi-C proximity maps for (a) a passive euchromatin system ($\sigma_0 = 0$) and (b) an active euchromatin system (extensile, $\sigma_0 = 30$); ; see Appendix B.5 for details of the method. The maps show chromosomes 1 and 4 that were not in direct contact in the initial condition (pink and orange chains in Fig. 4.2(d)). In each case, the lower diagonal (red) shows a time snapshot, whereas the upper diagonal (pink) shows an average over $t \in [350, 700]$. Blue segments along the axes indicate the HCDs (four per chromosomes), which are the locations where crosslinks can form. Green segments along the diagonal shows sections of the chain that are spatially contained inside the HCRs identified in Fig. 4.2(c). (c) Two examples of loops forming inside euchromatin in the extensile case and a zoom on their signature in the Hi-C map of (b), where their location is highlighted by purple and cyan triangles along the diagonal of chromosome 4 in (b). These panels use the data from the simulations in Fig. 4.2.

This is especially true in the active extensile case (Fig. 4.5(b)) and is consistent with Fig. 4.3(a), which showed that the fraction of beads contained in HCRs increases with activity. The fraction of the genome that is contained inside HCRs has a higher probability of interaction with itself due to its compacted nature; on the other hand, euchromatin away from HCRs is generally stretched out and thus has little interaction, beyond a few links in distance, with itself or with the spatially segregated HCRs. This results in a checkerboard patterning of high and low interaction. The diagonal squares in our simulations are one signature of the highly crosslinked HCRs, which have high inter-

region interaction frequency. The variable size of those squares in Fig. 4.5(b) reflects the number of sequential HCDs that are occupants of the same HCR as well as the amount of trapped euchromatin. The off-diagonal squares arise from genomically distal HCDs being bound together into a single HCR. We find that extensile activity also promotes interchromosomal interactions as a result of mixing, as evidenced by the off-diagonal blocks in the Hi-C maps. Checkerboard patterning, at a resolution of a $0.1 - 1\,\mathrm{Mb}$, is a prominent feature of experimental Hi-C maps and is characteristic of the spatial compartmentalization of two main types of chromatin: active and open euchromatin and inactive and compacted heterochromatin [28, 44, 90, 166, 167]. Clear square patterns are absent in the passive euchromatin simulation, where crosslinked heterochromatin forms throughout the nucleus and remains evenly distributed (see Fig. 4.2), resulting in a relatively stronger probability of interaction with neighboring euchromatin.

Another prominent feature evidenced in Fig. 4.5(b) is the formation of temporary loops inside euchromatin regions. In experimental Hi-C maps, the evidence of loops is also commonplace, where they are formed by active proteins known as loop-extruding factors such as condensin and cohesin [30]. Here, the loops we observe have a different origin and derive from the stretching of non-crosslinked chain segments by active hydrodynamic flows. In some cases, these loops occur in pairs as highlighted in Fig. 4.5(c), showing two examples of loop pairs and close-ups of their signatures in the Hi-C map of Fig. 4.5(b) where they appear as closed semi-circles along the diagonal. These structures bear resemblance to the star-shaped Hi-C patterns observed by Brandão *et al.* [168], where they were explained as a consequence of specific interactions between two condensin motors. Each yellow arrow emanating from the diagonal in the detailed Hi-C maps of Fig. 4.5(c) describes one loop, whereas the lines parallel to the diagonal and bridging the two arrows correspond to the adjoining bases of the two loops. The size and intensity of each semi-circle depends on the

length of the loops and their compactness. We note that these patterns do not persist on long time scales and indeed disappear in the time-averaged Hi-C maps due the dynamic nature of the loops, whose fate is governed by the nucleoplasmic flow.

In summary, the proximity maps of Fig. 4.5 recapitulate many qualitative features observed in experimental Hi-C maps, from checkerboard patterns resulting from compaction of HCDs and nearby euchromatin fragments into dense HCRs, to the formation of transient loops inside euchromatin due to the stretching and unfolding of the chromatin by the nucleoplasmic flows. ATP-powered dipolar activity is found to play a key role in setting these genomic features, with consequences for gene interactions and for the regulation of gene expression that remain to be explored.

4.4   Discussion

Our coarse-grained numerical simulations of a whole differentiated cell nucleus have shone light on the mechanical role played by ATP-powered active processes and nucleoplasm-mediated hydrodynamic interactions in the dynamics of heterochromatin segregation and compaction. Using a simple active Zimm polymer model consisting of alternating blocks of passive heterochromatin subject to inter- and intra-chain crosslinks and of active euchromatin decorated by stochastic active force dipoles, we showed that the structure of the nucleus is profoundly affected by extensile euchromatic activity: in comparison with systems with passive euchromatin, activity was found to enhance the compaction of heterochromatin into dense HCRs, also resulting in the more likely capture and trapping of nearby euchromatin fragments inside these HCRs. The mechanism for this enhanced compaction was attributed to the nucleoplasmic flows induced by active dipoles, which led to more intense mixing between chromosomal territories, thus allowing additional inter-chromosomal crosslinks by bringing distal heterochromatin domains into contact. Nucleo-

plasmic flows are especially intense and display long-ranged coherence in systems involving extensile dipoles, due to their spontaneous alignment in their own self-induced flow fields, which gives rise to the emergence of nematic alignement and stretching of the polymer chain inside euchromatin [9].

Our model for active stresses in terms of stochastic force dipoles is built on the premise that ATP-powered nuclear enzymes exert microscopic forces on local chromatin segments that are transmitted to the nucleoplasm via viscous drag. These active events occur on the scale of individual genes, thus below the spatial resolution of our bead-spring chromosomes, and could involve complex protein-chromatin dynamics such as: linear translocation of polymerases accompanied by the polymerization of RNA segments, conformational changes of the DNA double helix by helicases, or mesoscopic chromatin reconfiguration by loop extruding factors such as cohesin or condensin. In spite of this richness and complexity, the stress signature of each of these active processes on the nucleoplasm can be formally coarse-grained as driving a dipolar fluid flow, which is the leading-order contribution conserving local momentum in the multipole expansion of the flow field generated by that fragment of chromatin and associated active enzyme. The type of dipole (extensile or contractile), its magnitude and duration, as well as its local orientation with respect to the chromatin chain is unknown for each type of active event. Such knowledge could be gleaned by performing microscopic molecular-scale simulations of protein-chromatin interactions and systematically coarse-graining the stress and flow fields they generate.

4.5   Acknowledgements

Chapter 5

Active hydrodynamics of DNA loop extrusion

5.1   Introduction

There is growing belief that the extrusion process helps in the systematic packaging and organization of the chromosome inside the nucleus of a cell [27, 29, 90, 166, 167] using the SMC complexes. These proteins share a common three-dimensional architecture with a long ring like configuration formed by a heterodimer of Smc2 and Smc4 subunits. [169, 170]. The $\sim$ 50-nm-long antiparallel coiled subunits are connected at one end by a stable dimerization interface, referred to as the hinge domain, and at the other end by globular adenosine triphosphatase (ATPase) domains belonging to the ATP-binding cassette family (see figure 5.1). The head domains of Smc2 and Smc4 subunits are connected by a protein of the condensin kleisin family which are additionally connected to two subunits consisting mainly of HEAT-repeat motif. It has been hypothesized that the looping, which has also been observed recently in a series of experiments [34, 35, 171–173], and simulation studies [90, 166] is achieved by continuous extrusion of the DNA by the

motors as they move along the chromatin fiber at a force dependent speed using the energy obtained from the hydrolysis of ATP [27, 29, 174]. According to this mechanism, chromatin loops would initially be small but would increase in size over time as the loop extrusion factor processively moves more chromatin into the loop. The formation of loops assists in myriad genomic functions like gene expression, DNA damage repair, interphase domains, compaction and segregation of chromatin.

Most of the initial studies were focused on theoretical and computational approaches of modeling the extrusion mechanism to understand the folding of mitotic chromosomes and compaction by condensin into arrays of reinforced loops which were robust and stable to detachment of motors with multiple complexes at the base. Accompanied with 3D polymer simulations, these studies also demonstrated the functionality of loop extrusion to alter chromatin morphology [90, 91]. Even though the initial ideas were computational, they were extremely useful and provided a possible explanation of the underlying microscopic mechanism. Following the footsteps of compaction of mitotic chromosome by condensins were the observations of a transient loop extrusion in interphase chromatin in vertebrate cells by cohesin. The interaction of the loop extruding motors resulted in pyramid shaped structures on Hi-C maps and revealed that chromatin organizes into loops or topologically associated domains (TADs) that spans across a resolution of $0.1 - 1$ Mb of DNA with high self-contact frequency [24, 26, 44, 92]. The boundaries of these domains are represented as dots which represents interaction between two specific loci mediated by the extruding motors. The loop extrusion can therefore mediate specific interactions between distal genomic regions, and can generate specific chromatin domains.

Despite the fact that most of the modeling efforts pointed towards loop extrusion as the mechanism for explanation of a variety of chromosome organization processes, these were formulated without the direct observation of the active motor activity of the SMC

complexes, and hence largely remained a hypothesis until recently. Single molecule imaging experiments have enabled the direct observation of the loop extrusion phenomenon from total internal reflection fluorescence (TIRF) experiments where quantum-dot-tagged yeast (Saccharomyces cerevisiae) condensins were observed to asymmetrically translocate along double-tethered lambda phage DNA in the presence of the external imposed flow. The condensin motors were observed to extrude at speeds of 60 bp/s with a compaction rate of 1.5 kbp/s and was strongly dependent on the load experienced by the motor heads relating the speed of extrusion to the tension forces in the DNA polymer [34]. This experimental setup was used in several subsequent single-molecule experiments observing DNA loop extrusion by SMC complexes. Unlike yeast condensin, human cohesin extrudes loops symmetrically in vitro [35, 36] both in purified components and in extracts from interphase Xenopus laevis eggs [171].

The presence of the active flows induced by the action of the motor proteins in the above systems both in vivo and in vitro cannot be neglected as it has been shown to play a crucial role in micron scale coherent motion and heterochromatin phase segregation/compaction [9]. The interaction between these bound active agents and biological polymers give rise to intriguing non-equilibrium effects and their conformational and dynamical properties are substantially affected by the active processes. Using biophysical modeling and numerical simulations, we investigate the role of hydrodynamic interactions on the physical mechanism of the loop extrusion process, which was absent in previous simulations studies [28, 90, 166], and whether the presence or absence of hydrodynamic interactions can impact degree of DNA compaction. We find that in the presence of hydrodynamic interactions, the motors are stably bounded to DNA chain, and have high residence time which allows them to extrude longer loops (~ 2 times). The force dependent behavior of the motors can have considerable effect on the dynamics of extrusion

at different imposed flow conditions. We also perform simulations to construct a phase space which shows a non-monotonic behavior for the extruded loop length at different flow Peclet (Pe).

5.2 Model and numerical approach

We use a coarse grained model for the DNA as a wormlike chain polymer in a fluid of viscosity μ consisting of N beads of hydrodynamic radius r_h connected by finitely extensible springs (figure 5.1) of maximum extension u_0 [175, 176]. In this model, each spring represents only a portion of the entire DNA molecule containing a large number of nucleotides and bond pairs, where the Kuhn steps per spring is denoted as $N_{k,s}$ [62]. The motion of each bead is described by the Langevin equation given by equation (5.1) with two ends fixed on a wall parallel to an imposed flow field,

$$\frac{\mathrm{d}\mathbf{r}_i}{\mathrm{d}t} = \mathbf{v}^\infty(\mathbf{r}_i) + \sum_{j=1}^{N} \mathbf{G}(\mathbf{r}_i; \mathbf{r}_j) \cdot \mathbf{F}_j + \sqrt{\frac{2k_BT}{\zeta\mathrm{d}t}}\mathbf{n}_i(t), \tag{5.1}$$

where $\zeta = 6\pi\mu r_h$ is the corresponding friction coefficient and $\mathbf{G}(\mathbf{r}_i; \mathbf{r}_j)$ is the mobility tensor to account for hydrodynamic interactions between the beads with $\mathbf{F}$ being the sum of external deterministic forces such that,

$$\mathbf{F} = \mathbf{F}^a + \mathbf{F}^S + \mathbf{F}^{ev}, \tag{5.2}$$

and $\mathbf{n}_j$ is the randomly distributed Gaussian vector with zero mean and variance,

$$\langle\mathbf{n}_j(t)\rangle = 0 \qquad \langle\mathbf{n}_i(t)\mathbf{n}_j(t')\rangle = \mathbf{I}\delta_{ij}\delta(t - t'), \tag{5.3}$$

We assume a spatially homogeneous velocity such that the imposed field $\mathbf{v}^\infty(\mathbf{r})$ can be expressed as $\mathbf{v}^\infty(\mathbf{r}) = \boldsymbol{\kappa} \cdot \mathbf{r}$, where $\boldsymbol{\kappa}$ is the velocity gradient tensor. For simple shear flow,

the velocity gradient tensor is given by,

$$\boldsymbol{\kappa} = \begin{bmatrix} 0 & \dot{\gamma} & 0 \\ 0 & 0 & 0 \\ 0 & 0 & 0 \end{bmatrix} \quad \text{and} \quad \frac{\partial v_i}{\partial r_j} = \dot{\gamma}\delta_{i1}\delta_{j2} \tag{5.4}$$

Equation (5.1) is non-dimensionalised by the following scales used in previous studies on Brownian dynamics of DNA [175–179],

$$t_s = \frac{\zeta}{4H_c}, \quad \ell_s = \sqrt{\frac{k_B T}{H_c}}, \quad F_s = \sqrt{k_B T H_c} \tag{5.5}$$

which leads to the non-dimensional form of the Langevin equation,

$$\frac{\mathrm{d}\mathbf{r}_i}{\mathrm{d}t} = Pe(\kappa \cdot \mathbf{r}_i) + \frac{1}{4}\sum_{j=1}^{N} \mathbf{G}(\mathbf{r}_i; \mathbf{r}_j) \cdot \mathbf{F}_j + \sqrt{\frac{1}{2\mathrm{d}t}}\,\mathbf{n}_i(t), \tag{5.6}$$

where Pe is the bead Peclet $Pe = \dot{\gamma}\zeta/4H_c$ defined as the ratio of the characteristic flow time to the chain relaxation time. The boundary conditions for the two attached ends can be imposed by using the following expression,

$$\dot{\mathbf{r}}_1 = 0, \quad \text{and} \quad \dot{\mathbf{r}}_N = 0 \tag{5.7}$$
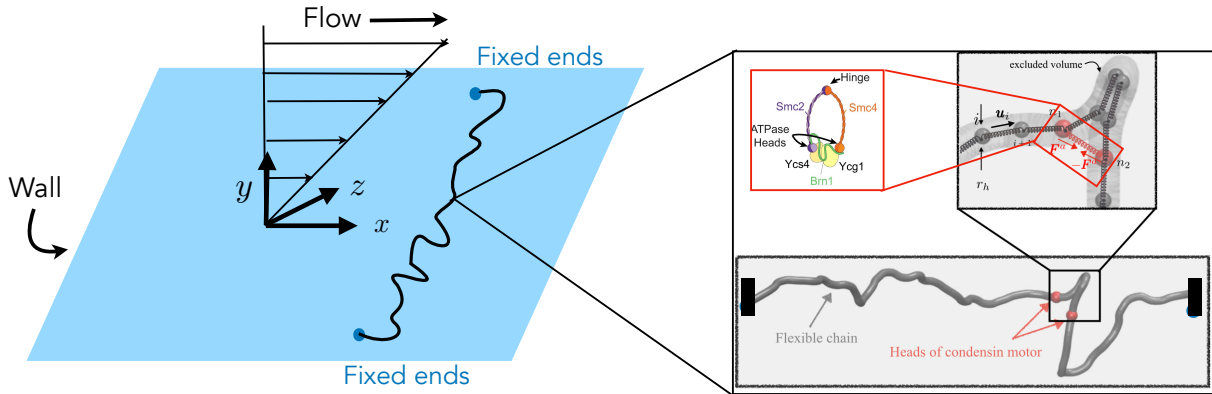
Figure 5.1: Sketch for the simulation setup with DNA polymer being attached at the two ends (blue points) in the presence of the imposed shear flow to imitate the experiments [34, 35, 172]. The zoomed in figure shows the model for the loop extruding motor with red-colored beads as the two heads of the motor connected by a harmonic spring. A cartoon of a yeast condensin complex adapted from [169]

In modeling intra-chain hydrodynamic interactions in the presence of the wall, a direct analytical expression for the Green's function $\mathbf{G}(\mathbf{r}_i; \mathbf{r}_j)$ is used that satisfies the no-slip condition at the wall $(y = 0)$, and also accounts for the finite size correction of the beads [180]. The non-dimensional radius of the bead r_h/ℓ_s can be written in terms of the hydrodynamic interaction parameter $h^* = r_h\sqrt{H_c/\pi k_B T}$ [175, 177] given in the table 5.1. Equation (5.6) can be solved by a two step predictor-corrector algorithm by recasting it in terms of spring connector vectors $\mathbf{u}_i$ to correct for the spring length at each time step, and takes care of the local bond extension exceeding the maximum spring length (u_0) that can occur during the simulation. Here, we will use the algorithm used in [110] for the free-draining case, which was extended to involve the full hydrodynamics in [181].

5.2.1 Model for DNA as a wormlike polymer

The model involves a flexible polymer chain composed of N beads connected by freely rotating mass-less springs of maximum extensibility u_0 subjected to forces given in equation (5.9), and the vector pointing from bead i to $i+1$ is denoted by $\mathbf{u}_i = \mathbf{r}_{i+1} - \mathbf{r}_i$ as shown in figure 5.1. The drag force from the surrounding fluid are experienced by the beads of the chain, and the spring represents the entropic effects such that,

$$\mathbf{F}_i^S = \begin{cases} \mathbf{F}_i^C & \text{if} \quad i = 1, \\ \\ \mathbf{F}_i^C - \mathbf{F}_{i-1}^C & \text{if} \quad 1 < i < N, \\ \\ \mathbf{F}_{N-1}^C & \text{if} \quad i = N, \end{cases} \tag{5.8}$$

where $\mathbf{F}_i^C$ is the constraint force on bead i using the Marko-Siggia (or worm-like spring) form of the spring potential that matches the asymptotics of the exact worm like chain

model in both the small and large force limits [73, 182],

$$\mathbf{F}_i^C = \sqrt{\frac{N_{k,s}}{3}} \frac{\mathbf{u}_i}{u} \left[\frac{1}{2} \frac{1}{\left(1 - u/(3N_{k,s})^{1/2}\right)^2} - \frac{1}{2} + \frac{2u}{\sqrt{3N_{k,s}}} \right], \qquad (5.9)$$

with the Hookean spring constant given by $H_c = 3k_B T/N_{k,s} b_k^2$ and $u_0 = N_{k,s} b_k$. The total number of Kuhn segments $N_{k,tot}$ in the molecule is $N_{k,tot} = (N-1)N_{k,s}$, the Kuhn step size is b_k, and the total dimensional contour length L of the DNA macro molecule is $L = N_{k,tot} b_k$.

5.2.2 Model for motor dynamics (active forces)

The motor proteins have a ring like structure which can stochastically attach to the chromatin fiber and progressively extrude along its length thus nucleating and enlarging the chromatin (or DNA) loop between the subunits to form arrays of loops. The action of the loop extrusion is modeled as an additional stiff harmonic potential in the form of a link (or spring) between two adjacent beads (i, j) acting as the heads of the condensin/cohesin. Each active head can processively translocate along the backbone chain, thus creating and enlarging the DNA loop between the subunits in a symmetric manner. We have assumed that the motors will perform symmetric two sided extrusion depending on the availability of the neighbouring sites even though yeast condensin have shown to extrude in a asymmetric one sided manner. Whether two-sided extrusion might occur due to structural differences between the different species of condensin or dimerization of the condensin molecules is still unclear. When the loop extruding motor (also known as loop extrusion factor or LEF) takes a step, the existing bond is deleted and replaced by a new bond between bead $(i-1, j+1)$, provided that there are no other LEF at the updated sites [28, 90, 183]. We assume that all active links also follows worm like chain model and are stiffer compared to the link maintaining the equilibrium length of the polymer acting on the beads of the

main chain. The SMC complexes are assumed to be on the scale of one link, bind to the main chain stochastically as a Poisson process with on - rates k_{on}. An actively extruding motor with two heads at n_1 and n_2 (see figure 5.1) will exert two equal and opposite forces ($\mathbf{F}^a$) on the DNA polymer at the positions of two heads, pointing towards each other along the local relative position vector ($\boldsymbol{r}_{n_1} - \boldsymbol{r}_{n_2}$) thus exerting a contractile dipole force on the polymer chain as well as on the fluid via viscous hydrodynamic drag.
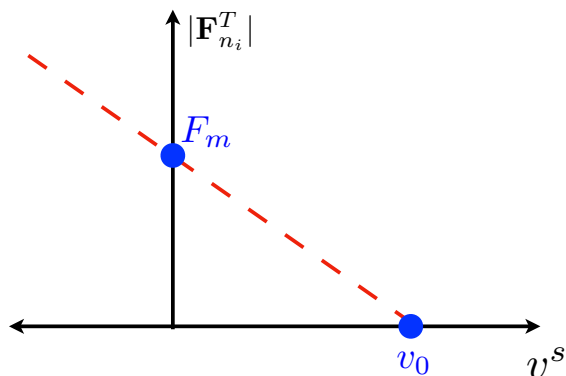
Figure 5.2: Figure shows the linear force-velocity relationship for loop extrusion. On exceeding the maximum force, LEF will move in the reverse direction if the site is unoccupied.

A child or sub-loop can exist within an existing parent loop and either heads of two adjacent extruding motors can not cross each other (or occupy the same position as other head of any LEF, see figure 5.3). We have also accounted for the force-velocity relationship that the motor follows as it extrudes along the DNA. This means that the extrusion velocity will be small when DNA is experiencing high tensile forces, and will extrude with maximum velocity when DNA is slack. Some of the parameters like the are obtained from recent experiments [34, 35, 172]. The velocity of extrusion v_k^s of motor k where the heads of the motor are at (n_1, n_2) is given by the force-velocity relationship,

$$v_k^s = v_0 \left(1 - \frac{0.5|(\boldsymbol{F}_{n_1}^T| + |\boldsymbol{F}_{n_2}^T|)}{F_m} \right), \tag{5.10}$$

where F_m is the maximum (or stall) force at which the motor changes its direction of

extrusion (or begins to de-extrude the chain), v_0 is the zero force velocity of the motor and $|\boldsymbol{F}_{n_i}^T| = |\boldsymbol{F}_{n_i}^S| + |\boldsymbol{F}_{n_i}^a|$ for $i = 1, 2$ (see figure 5.1). The force magnitude ($|\boldsymbol{F}_{n_i}^T|$) is chosen to be the average of the forces on the beads n_1 and n_2 that involves contribution from the tension forces in the main chain as well as from active forces coming due to the stochastic formation of a LEF link between the heads (n_1, n_2). If the force experienced by either heads of a link exceeds F_m, the LEF reverses its direction and begins to de-extrude the chain or can detach based on the detachment rate k_{off}. The process of de-extrusion allows for a competition between any two loops on a highly stretched chain and is motivated from the experiments of budding yeast condensin on λ-phage DNA [172] where one of the two loops were observed to grow at the expense of the existing loop. The LEF head under forces lower than F_m will start to reel in the DNA that is already being extruded by the LEF experiencing high forces. Figure 5.3 shows the important events for $Pe = 0.0$
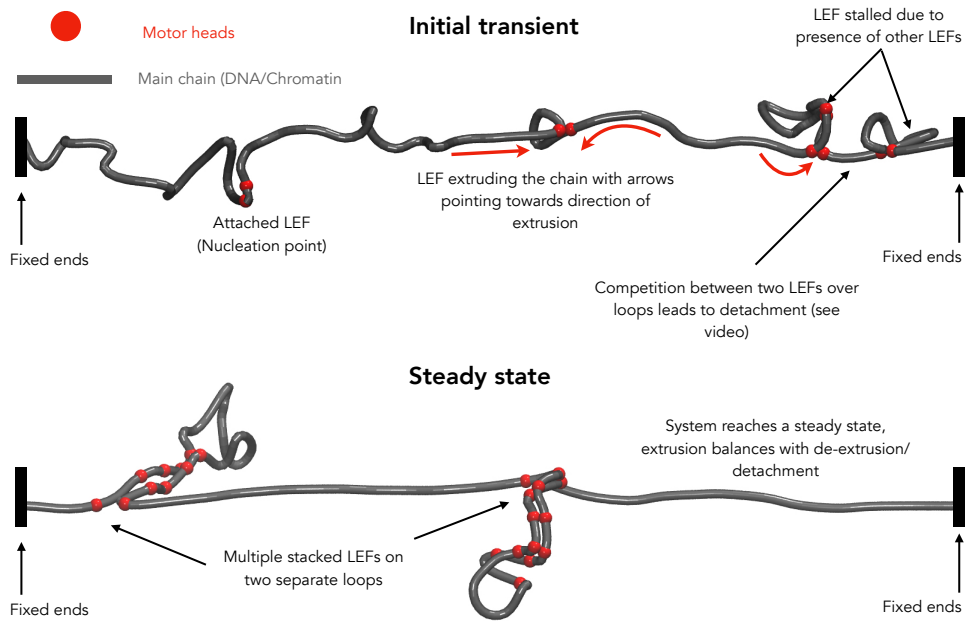
Figure 5.3: Figure shows a snapshot from the simulations highlighting important events in the active loop extrusion process with the red-colored beads representing the two heads of the motor connected by a harmonic spring. The chain is attached fixed at the two ends.

governed by the motor dynamics that is explained above. The nucleation event begins with attaching of the motor heads to adjacent beads with a stiff harmonic spring between them. The extrusion process starts when the adjoining motors heads begins to move along the DNA to form loops. When two loops are standing next to one another, it can give rise to competition between them resulting in one loop winning over the other for the available DNA. Eventually, the detachment/attachment of motors will balance each other leading to steady state. At this point in the simulation, multiple long stable loops can be seen which have stacks of motors formed on top of each other.

5.3 Results and discussion

In this section we consider simulations of a single chain with $N = 100$ beads, and two ends tethered to the wall in the $x - z$ plane. Other relevant parameters are listed in Table 5.1, most of which are obtained from the experiments. A linear shear flow is applied in the direction parallel to the wall varying linearly in the y direction, and satisfying no slip condition at the wall. In the absence of the motors, external shear flow would stretch out the chain in the direction of the flow resulting in a parabolic shape profile. The chain will continue to fluctuate due to local balance between Brownian, shear and tension forces. In the presence of the loop extruding factors, the heads of a motor attach to adjacent beads on the chain, and start to extrude the DNA based on the mechanism given in the above section. The process of attachment is based on k_{on} rate whereas the de-extrusion/detachment can happen once the tension inside the chain exceeds the stall force F_m and is based on k_{off}. Figure 5.4 (A) shows the evolution of the loop length l/L for $p_a = k_{on}/(k_{on} + k_{off}) = 0.5$ and $Pe = 0.75$, and the system will reach a steady state once the total loop length reaches a plateau. The increase in the loop length during the initial transient occurs due to continuous extrusion of the slack chain by the bound

motors. Once the tension inside the chain reaches F_m as a consequence of continuous extrusion and imposed flow, the de-extrusion/detachment process begins which eventually comes into balance with the attachment of the motors and leads to steady state as shown in Fig. 5.4 (A). In the absence of the external flow, these loops exist in a compact crumpled state similar to the ones observed in the experiments whereas, applying an external flow stretches out the loops to make them clearly visible in experiments. The above setup has been used as a test bed in previous experimental studies [34,35,171,172] to characterize the extrusion mechanism and its dependence on external factors (like concentration of ATP, cohesin-NIPBL interactions etc.) The experiments were performed on λ-phage DNA with nuclear extracts from a cell at the interphase stage inside a micro channel [171]. The DNA strands were attached at the two ends and stretched using an imposed flow.

5.3.1 Hydrodynamic interactions assist loop formation

In this section, we will look at the effects of hydrodynamic interaction on evolution of extruded loop length for different flow Pe.

Table 5.1: Numerical values of the parameters used in the simulations.

Parameters	Numerical Value (present study)	Physical interpretation
b_k	0.132 μm	Kuhn step of DNA [177]
L	16.5 μm	contour length of DNA [34]
N	100	number of beads
$\nu = \Phi_0 H_c/(k_B T)^2$	100	excluded volume coefficient
h^*	0.12	hydrodynamic interaction parameter
$k_{on}/k_{o}ff$	$0.001 - 0.2/0.02$	attachment/detachment rate
F_m	$0.16 - 1.2$ pN	maximum force (or stall force) [34, 171]
v_0	$0.6 - 2.8$ kbp/s	max. extrusion velocity [34, 35, 171, 172]

Fig. 5.4 (B) shows top view snapshots from numerical simulations to compare the dynamics in the absence and presence of hydrodynamic interactions for $Pe = 0.75$ along with $Pe = 0.0$ for reference. The initial condition is a slacked polymer colored in grey with

two ends tethered to the wall ($z = 0, z = L$). The location of each motor head is shown in red color which can attach/detach based on the mechanism given in above section. Once the motors attaches to the chain, it starts to reel the DNA in from the sides, forcing out a progressively larger loop in between. For $Pe = 0.0$, the loops grows as the time evolves, and are located uniformly along the length of the chain. They can also go out of the plane as can be seen from the figure 5.4 (B). On applying an external flow, the chain stretches out in the $x - z$ plane, and motors progressively translocate along the length of DNA with loops forming predominantly in the middle of the chain. Figure 5.4 (A) shows the temporal evolution of the average loop length and compares the two cases of with/without hydrodynamic interactions (HI) for two flow Pe.
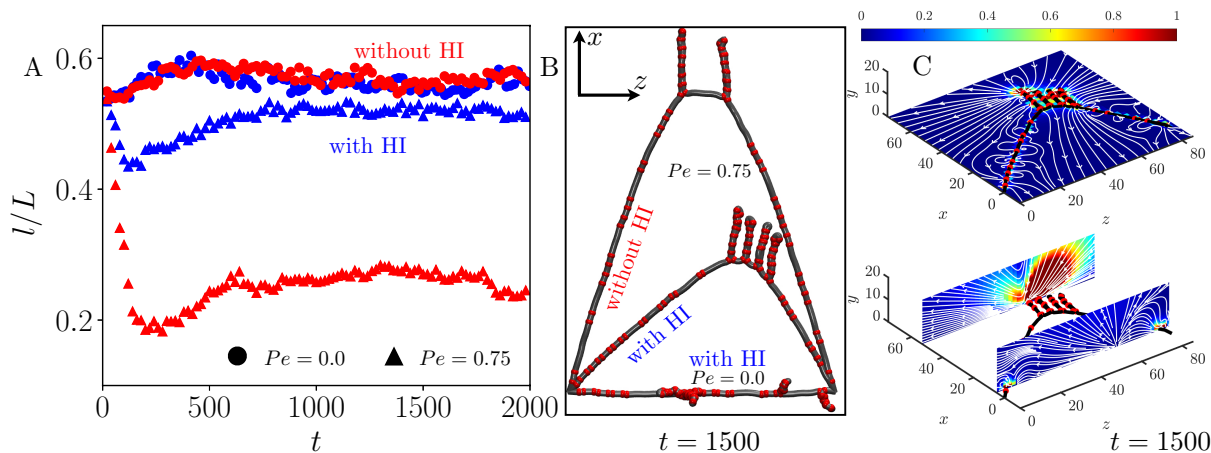
Figure 5.4: Figure shows the (A) evolution of total length of the loop extruded by the DNA for $Pe = 0.0$ and $Pe = 0.75$ in the presence and absence of hydrodynamic interactions. (B) The snapshots ($x - z$ plane) of the DNA tethered to the wall at $t = 1500$ showing the difference in dynamics in the presence and absence of hydrodynamic interactions for different flow Pe, the chain tends to be more stretched out in space due to the external flow. (C) 3D flow field at $t = 1500$ in different planes shows the response of the chain to the external shear flow showing a strong negative correlation between the imposed field and response flow.

Under external flow and in the presence of hydrodynamic interactions, the stretching of the polymer induces high tension within the chain which in turn creates a response

flow in the opposite direction to the imposed flow. The response flow further lowers the force experienced by the motor heads thereby assisting them to progressively extrude the loops. The absence of hydrodynamic interactions does not create these response flows and leads to small loop lengths due to strong tension forces experienced by the motors resulting in their detachment. For $Pe = 0.0$, there is no significant difference on the length of loop extruded for the two cases, and only gets exaggerated in the presence of the flow. To validate our arguments, we analyzed the flow fields generated by the external forces acting on the extruding polymer. In the Stokes regime ($Re \rightarrow 0$), the velocity at any point x in the fluid is simply obtained in terms of the force distribution along the polymer. Snapshots of the instantaneous flow fields in two different planes induced by the deterministic forces are shown in figure 5.4 (C) with no-slip condition at the wall.
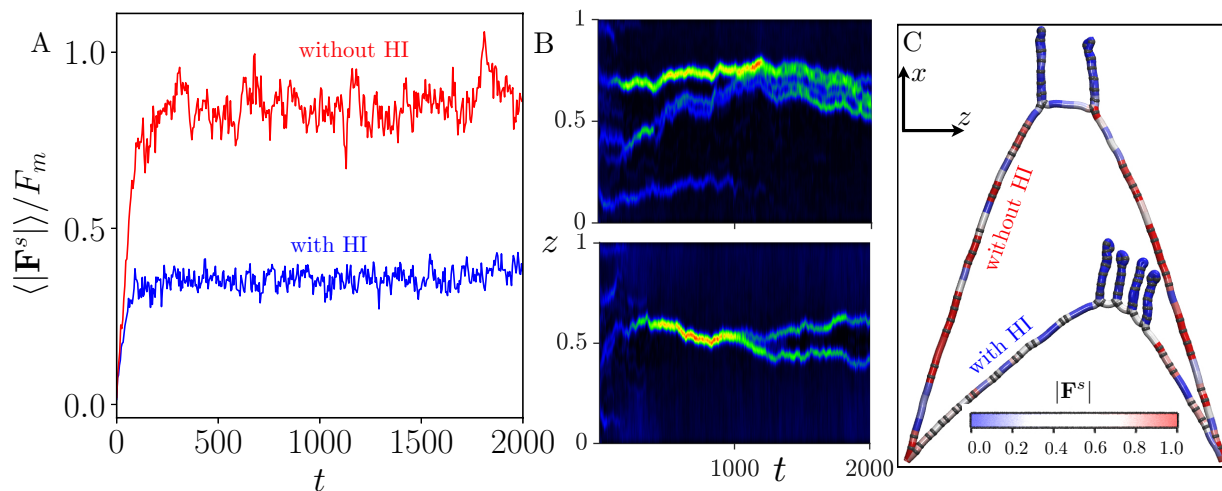
Figure 5.5: (A) Figure shows the evolution of magnitude of tension forces inside the chain for $Pe = 0.75$ in the presence and absence of hydrodynamic interactions. (B) The kymographs of the 1-D motor density averaged in the $x - y$ plane represents accumulation of the motors at the center of the chain, the top and bottom plot are without and with hydrodynamic interactions respectively. (C) Spatial variation of the magnitude of tension forces along the length of the chain normalized with the maximum stall force at $t = 1500$.

Along with the induced flow, there also exists recirculation regions for certain con-

formations due to the presence of the wall. As expected, velocities are largest close to the polymer ($\sim \frac{1}{r}$), with maximum values attained near the motor heads and tethered ends. In addition to the flow field, time evolution of average tension inside the chain is also shown in figure 5.5 (A). In the presence of hydrodynamics, the response flow relaxes the chain which reduces the tension inside the polymer thus allowing the motors to extrude longer loops. The magnitude of average tension with respect to time inside the chain confirms the above hypothesis. In addition to loop length, there is a preferential accumulation or eventual migration of the motors at the center which can be ascribed to low tension forces experienced by the polymer in the middle. This makes it relatively easier for the motors to stay stably bound to the chain compare to other locations along the length of the chain irrespective of hydrodynamic interactions. The kymographs also confirm this picture where the maximum density is seen at the center during the later stages of the simulation. In the middle of the chain, the motor at the base of a loop experiences the least tension and the rest of the motors can bind on top of one another resulting in a stable loop with stack of motors providing with additional reinforcement in the event of base motor detachment. This results in a stable loop near the center with a high motor density as reflected in the kymographs.

Effect on the loop number statistics

The importance of hydrodynamic interactions is less prominent in weak (or no) flow as can be seen from figure 5.4 (A) and 5.6 (A). For flow $Pe = 0.0$, the distribution of number ($P(N_l)$) of loops does not show a profound difference in the presence (blue) and absence (red) of hydrodynamic interactions as compared to $Pe = 0.75$. The presence of hydrodynamic interactions, however, for moderately strong flows ($Pe = 0.75$), assists in the loop formation and results in almost twice the number of loops due to additional

stability of the motors to stay bound on the chain. The higher probability of loop formation is also reflected in figure 5.6 (B). In order to inspect the effects of varying p_a, we will look at the parameters where the transition happens in phase space (see figure 5.8 (A), phase space).
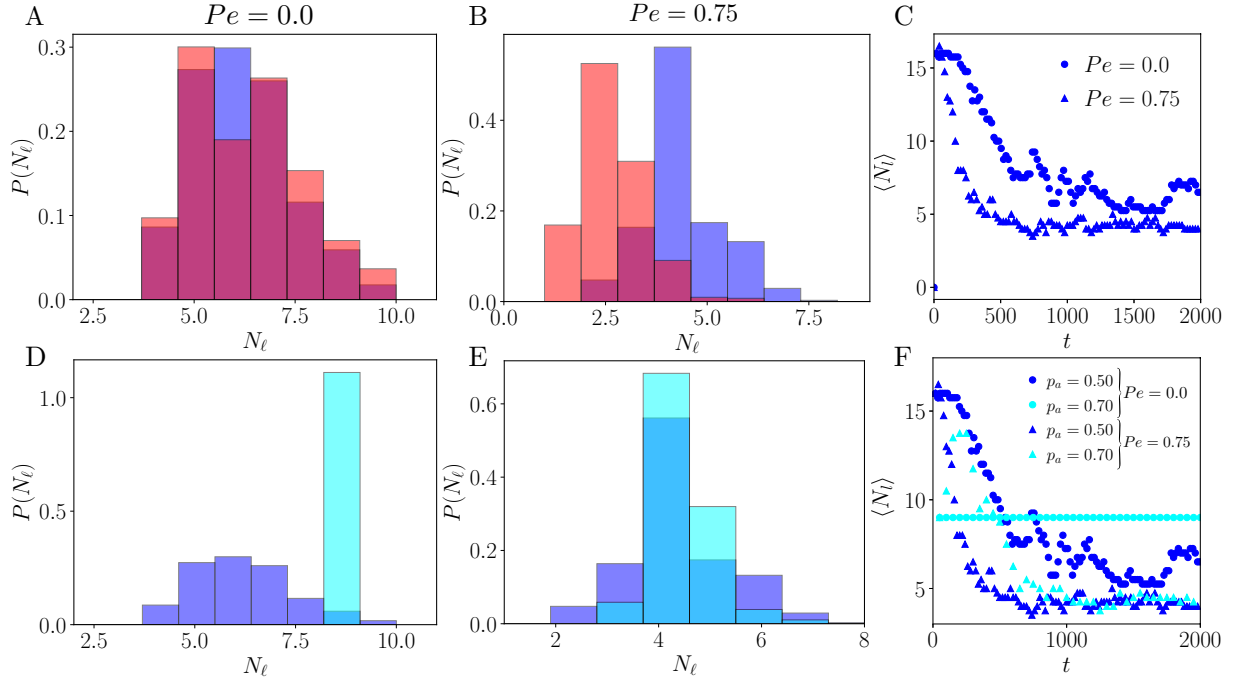
Figure 5.6: (A,B) Probability density $(P(N_l))$ of the number of loops N_l for $Pe = 0.0$ and $Pe = 0.75$ in the presence/absence of hydrodynamic interactions. In the presence of the imposed external flow, hydrodynamic interactions has a more profound effect on the dynamics of the loop formation. (C) Evolution of average number of loops with respect to time to different flow Pe. (D,E) Probability density $(P(N_l))$ of the number of loops N_l for $Pe = 0.0$ and $Pe = 0.75$ in the presence of hydrodynamic interactions for different p_a values. (F) Evolution of average number of loops with respect to time to different flow Pe and p_a.

The number of available motors that can be bound to the chain is only dependent on the parameter p_a whereas their time spent bound to the DNA depends on the underlying tension forces. For low flow $Pe = 0.0$, the presence of additional number of motors for $p_a = 0.7$ allows for higher probability of forming a loop as shown in figure 5.6 (D) but of

shorter length when compared to $p_a = 0.5$ (figure 5.8 (A)). The short loop lengths at high p_a mainly arises because of unavailability of free DNA for the motors to extrude. Moving to a high $Pe = 0.75$, there is no difference in the distribution of loop numbers between the two p_a values. The presence of imposed flow assists in unbinding of the motors which open up the DNA for the motors to extrude. In addition to that, the mean number of loops (and loop length) are higher under weak flows due to the weaker tension forces resulting in higher probability of motors to stay attached to the DNA. We will discuss more in detail in the section on phase diagram.

Effect on the motor number statistics

As mentioned earlier, the probability of the motors to stay bound to the chain is strongly affected by the mean tension in the chain. In order for a stable loop to exist, the base of the loop should be able to extrude a loop under low tension forces. Once the loop is long enough that it can accommodate multiple motors that can stack on top of each other, and it will be stable because of multiple motor reinforcement in the event of detachment of the base motor. The low mean tension inside the polymer ensures that a stable loop can be formed. From figure 5.7 (A), the fraction of chain that is occupied by the motors ($\langle N_m \rangle$) shows no discernible difference for different Pe (with and without hydrodynamic interactions) as the number of the available motors is only a function of parameter p_a. Even in the event of a detachment the opened up site is occupied by another available motor. The primary effect of the mean tension is reflected in the fraction of motors that are bound inside the loop f_{N_m}. For low $Pe = 0.0$, low mean tension in the absence of the flow allows the bound motors to stay stably bound to the chain and form longer loops which eventually results in considerably more available sites for the motors to occupy inside the loop. In summary, the tension inside the chain is inversely proportional to the

101

fraction of motors inside the loop as summarized in figure 5.7 (B) and (C).
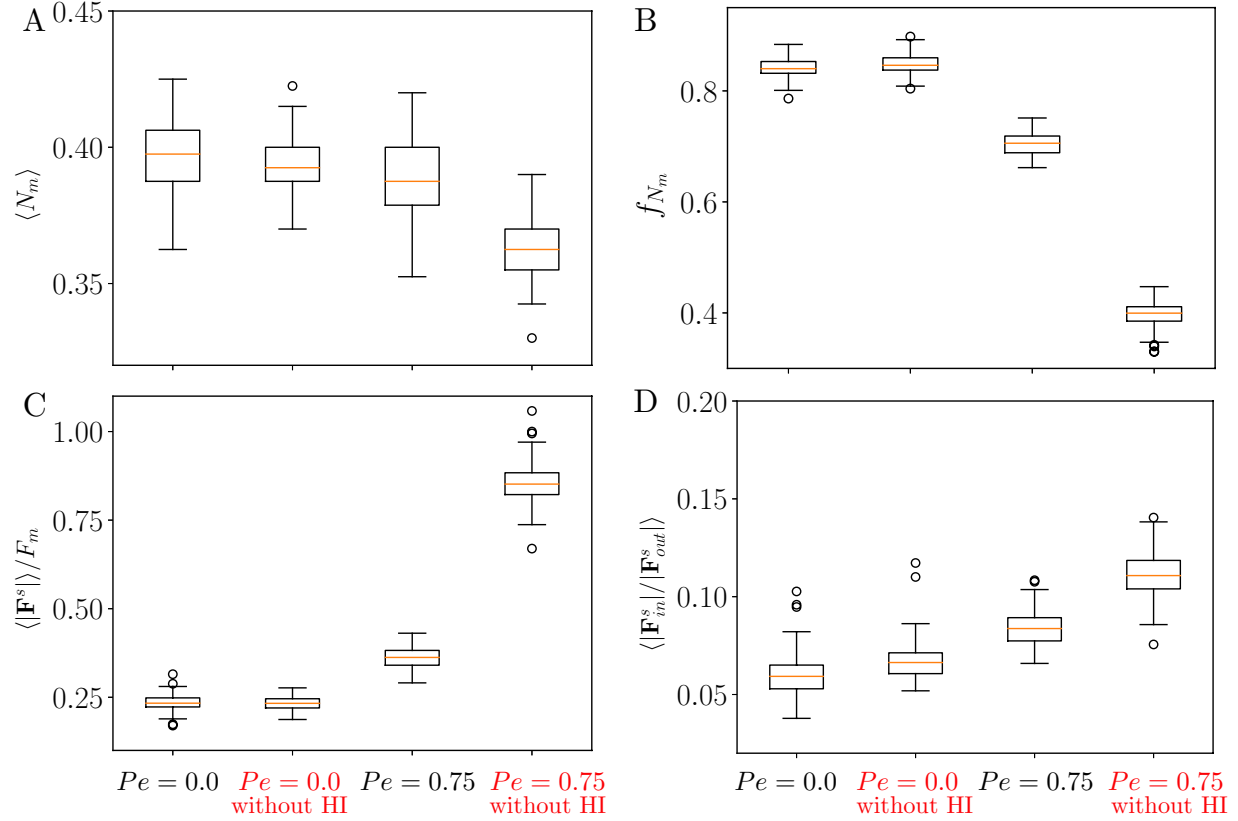
Figure 5.7: (A) Average number of bound motors to the polymer for different Pe in the presence/absence of hydrodynamic interactions. Number of bound motors does not get affected by the flow, and is only a function of p_a and tension inside the chain. (B) The fraction of motors bound inside the loop shows a strong dependence on the average tension in the chain (C). For stronger tensile forces, the probability of motors to stay bound to the chain is low which results in smaller loops thereby reducing the number of motors inside the loops. (D) Variation of tension inside the loop to the tension outside the loop.

Additionally, the presence of motors inside the loops provides an additional stability to the loop which is reflected in the ratio of tension force inside to the outside of the loops as shown in figure 5.7 (D).

5.4 Phase Diagram: Effect of varying $Pe - p_a$

Next we can systematically explore the parameter space $(Pe - p_a)$ through numerical simulations and characterize non-monotonic features of loop extrusion in figure 5.8. On increasing the flow Peclet number, one can argue that the tension inside the chain would increase which further increases the load on the motor heads thus inducing the detachment/de-extrusion mechanism, and subsequently resulting in small size loops.
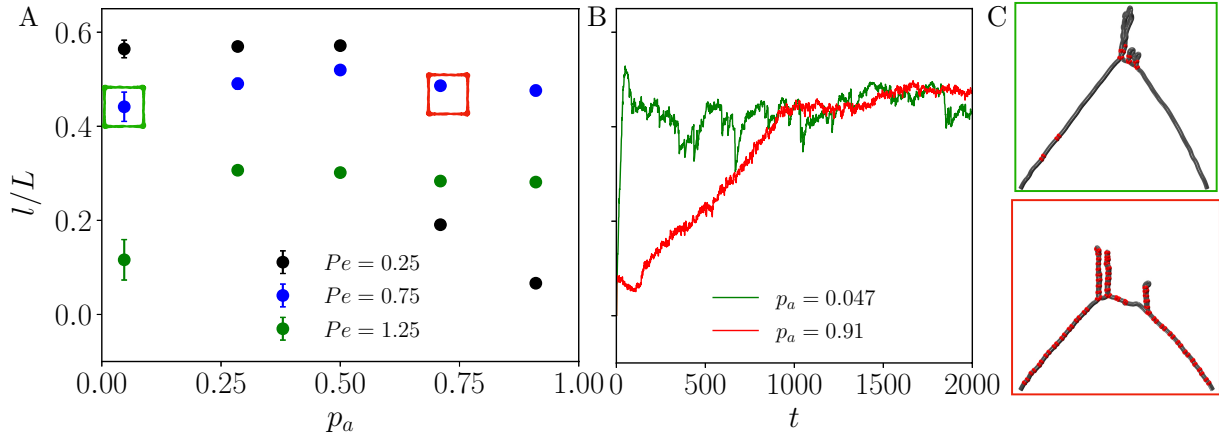
Figure 5.8: (A) Phase diagram of l/L v/s p_a for different flow strength Pe. (B) The time evolution of dimensionless loop length for different p_a. At higher Pe, varying the number of bound motors does not affect the extruded loop length. (C) Snapshots illustrating the number of bound motors to the polymer chain for different values of p_a. Higher values of p_a corresponds to more number of motors which will provide more stability to the loop formed, whereas low values of p_a will lead to weaker loops which can be seen in the highly fluctuating mean values of l/L for $p_a = 0.047$

This argument seems to work well for low $p_a \sim < 0.5$ where increasing the flow rate results in a decreases in the average length of the extruded loop. The natural tendency of the motors to extrude the available DNA is resisted by the presence of the external shear flow, and a clear monotonic behavior can be seen for $p_a < 0.5$. Figure 5.8 (C, top) shows a snapshot of the chain for $Pe = 0.75$ and $p_a = 0.011$ where a small number of motor proteins extrudes multiple loops at the center which shows presence of fewer motors with

large fraction of DNA available to be extruded. Once the motors extrude most of the DNA so as the tension inside the chain exceeds F_m, the de-extrusion/detachment process results in unbinding of the motors, and eventually a steady state is attained. To the contrary, the dynamics is completely different and the trend is non-monotonic at high $p_a > 0.5$ values. In the high $p_a \sim > 0.5$ regime, the motors heads can occupy most of the available sites on the polymer chain as can be seen from figure 5.8 (C, bottom). This results in small size loops at low Pe as most of the available sites on the DNA are occupied by the motor heads and hence can not be extruded. For moderate $Pe = 0.75$ regime, as the simulations advance in time, the increase in tension due to stretching of the chain under strong flows, triggers the detachment of the motor proteins and open up sites on the DNA especially near the centre of the chain. The motors starts occupying the available empty sites resulting in comparatively longer loops. For high $Pe = 1.25$, the dynamics is strongly influenced by the imposed flow, and the motors cannot stay long enough on the DNA to extrude it efficiently thereby resulting in small size loops for all values of p_a. Surprisingly, the size of the loop does not depend on p_a for moderate Pe partially could be due to a balance between the detachment of the motors and extrusion.

5.5   Acknowledgements

Chapter 6

Concluding remarks and future direction

6.1 Conclusion

In the present thesis, we have considered many complex multifaceted problems on dynamics of chromatin organization at different length scales and implications of mechanics and hydrodynamic flows on it. The present work focused largely on developing efficient computational tools to perform numerical simulations and comparing them with available experimental data with focal point of elucidating the underlying physical mechanisms. The myriad range of length and time scales in these problems can generally prove to be a computational bottleneck, the ways to systematically approach some of them has been addressed in this work.

In Chapter 2, we discussed various aspects of biophysical modeling and hydrodynamics of chromatin/DNA as flexbile active polymer. We also discussed origin of subcellular activity inside the cell, and how they can be modeled at molecular level, and coarse grained at the required resolution. Further, we extended the length scales of simulations

to incorporate new physics, and provided a numerical framework to perform simulations within biological time scales. One such example is the presence of multiple chromatin chains bounded by a prolate spheroid which has been lacking in the literature. This allowed us to understand the interactions between multiple chromosomes, and their compaction inside the nucleus. Our discussion also provided a number of existing useful concepts and properties that formed the backbone of the current work.

We will begin with elucidating the self induced spontaneous coil-stretch transition of active polymers in free space as highlighted in **Chapter 3**. We analyze the conformational dynamics and statistical properties of an active polymer model. Using Langevin simulations of isolated chains in unconfined domains, we show how the coupling of active flows with polymer conformations leads to emergent dynamics. Systems with contractile dipoles behave similarly to passive Brownian chains with enhanced fluctuations due to dipolar flows. In systems with extensile dipoles, however, our simulations uncover an active coil-stretch transition whereby the polymer spontaneous unfolds and stretches out in its own self-induced hydrodynamic flow, and we characterize this transition in terms of a dimensionless activity parameter comparing active dipolar forces to thermal fluctuations. We also drew a comparison in the context of the classic coil-stretch transition of passive polymers in extensional flows, and complement our simulations with a simple kinetic model for an active trimer.

Building on the tools and physics discussed in Chapter 2, we highlighted the mechanical role played by ATP-powered active processes and long-ranged hydrodynamic interactions in the dynamics of heterochromatin segregation and compaction in **Chapter 4**. We perform large-scale coarse-grained simulations of an entire model nucleus as a rigid membrane containing multiple chromosomes suspended in a viscous nucleoplasm. Our numerical results underscore the role of activity-driven coherent motions and nucleoplasmic

flows on the compaction and spatial distribution of heterochromatin in differentiated cells. We found that activity enhances the compaction of heterochromatin regions (HCRs) and the trapping of euchromatic fragments within, relative to the passive case, while creating large-scale nematic alignment outside of HCRs where euchromatic domains are largely unconstrained and free to align with themselves and with boundaries. Interestingly, we also find that the stress fields are strongest outside of HCRs and involve opposing contributions from activity and internal tensile forces. The coherent fluid flows on large length scales also show evidence of hydrodyamic screening by the crosslinked heterochromatin regions. We were also able to recapitulate many qualitative features observed in experimental Hi-C maps, from checkboard patterns, to the formation of transient loops showing the robustness of the present approach.

Chapter 5 focus on dynamics of active loop extrusion that are driven by nuclear enzymes known as Structural maintenance of chromosomes (SMC). These motors are involved in extrusion process which helps in the systematic packaging and organization of the chromosome inside the nucleus of a cell. Using a bottom-up modeling approach that accounts for all the necessary structural details and stochastic kinetics of molecular motors, we were able to observe a variety of loop and motor patterns which were assisted by the presence hydrodynamic interactions. Our computations also revealed that in the presence of external shear flow which are typically used in experimental test beds for clear visualization of loops, the dynamics of the motors are greatly affected due to their tension dependent mechanical function. This in turn affects the ability of the motors to extrude thereby affecting the statistics of number and length of loops extruded in relevant parameter regimes. Model predictions agreed with recent experiments and illuminated the crucial roles of hydrodynamics and bio-mechanical feedback in loop extrusion.

6.2 Ongoing work and future directions

Here, we will discuss a few potential directions that can be explored further based on our work. Broadly, we have outlined three different aspects below,

- *Interaction of chromatin with lamina:* In Chapter 4 we discussed how the presence of nucleoplasmic flows and active stresses assists the formation of heterochromatin domains of the genome. Heterochromatin formation and compaction in our simulations was observed to occur near the center of the nucleus – a likely consequence of the symmetry of the initial data, in which a randomly placed HCD is statistically more likely to find another HCD to bind with near the center of the system than near the boundary. This central placement is consistent with past equilibrium simulations of heterochromatin formation [5, 6], but fails to capture the complexity of the heterochromatin distribution observed in experiments, where HCRs tends to concentrate near the nuclear envelope and in the periphery of nuclear bodies such as nucleoli. This suggests the likely role of other types of interactions, such as tethering of the chromatin chain to the nuclear lamina, which is known to be of importance in experiments where it results in hererochromatin-rich lamin-associated domains (LADs) [184]. Accumulation of heterochromatin near boundaries in the presence of binding interactions has been observed in equilibrium simulations [52], even when both eu- and heterochromatin have the same affinity with the boundary [53]. The role played by activity-driven flows in the formation, distribution, and compactness of LADs is open question. In addition to that, ATP-powered dipolar activity is found to play a key role in setting the genomic features, with consequences for gene interactions and for the regulation of gene expression that remain to be explored.

- *Rheological response of chromatin:* Another problem that could be relevant is the

rheological repsonse of the heterogeneous chromatin structure which impacts the timescales and length scales of all biological processes [185]. As demonstrated by our model, the process of heterochromatin segregation is not only driven by local crosslink formation but also tightly coupled to the large-scale mechanics of chromatin and nucleoplasm, which interact via active and passive stress fields distributed across the entire nucleus. The strongly heterogeneous structure of chromatin organization suggests a complex spatially dependent rheological behavior, with crosslinked heterochromatin behaving like an elastic porous solid, and unconstrained active euchromatin behaving like an active fluid with local nematic order [164]. These two segregated materials interact via both mechanical stress at the outer boundary of HCRs, and viscous stresses due to nucleoplamic flows, which permeate both phases. This picture is supported by the recent experiments of Eshghi *et al.* [186], which used passive microrheology to infer the local rheological behavior in differentiated cell nuclei and uncovered a coexistence of fluid-like and solid-like phases. A numerical characterization of effective rheological properties in simulations could elucidate the micromechanics underlying these measurements, as well as provide a basis for developing self-consistent continuum models of nuclear mechanics that could be used for mathematical analysis as well as mean-field simulations [187].

- *Loop extrusion on a chromatin fiber with/without confinement:* A natural extension to the present work in the case is to elucidate the effect of loop extrusion on a chromatin polymer. Unlike the case of a short chain, the loop extrusion on a long chain have shown to play an important role in the formation of topologically associated domains, especially in the presence of a confinement. In this way, the motor dynamics can be added at a microscopic level without the need of coarse graining, and the macroscopic properties can be measured. We can systematically start with placing

the motors in free space on single/multiple chains, and compare the interactions between the chain in the presence of the motors and flow field created by them. Furthermore, we can add them inside a confinement to look at their effect. The fundamental challenge is to compute efficiently large scale hydrodynamic interactions that typically scale as $\mathcal{O}(N^2)$.

Appendix A

Comparison with full hydrodynamics

The model discussed in Chapter 3 Sec. 3.2 describes a freely-draining polymer chain where hydrodynamic interactions due to constraint forces, excluded volume interactions and thermal fluctuations are neglected and where the only hydrodynamic flow is that induced by active dipoles. Here, we present a more complete model that accounts for hydrodynamic interactions and compare results obtained by both formulations. In the presence of hydrodynamic interactions, the Langevin equation (3.1) becomes:

$$\frac{d\mathbf{r}_i}{dt} = \mathbf{u}^a(\mathbf{r}_i, t) + \sum_{j=1}^{N} \mathbf{M}_{ij} \cdot \left[\mathbf{F}_j^c(t) + \mathbf{F}_j^e(t) \right] + \boldsymbol{\xi}_i(t). \tag{A.1}$$

$\mathbf{M}_{ij}$ denotes the grand mobility tensor that captures viscous drag on the beads as well as long-ranged hydrodynamic interactions:

$$\mathbf{M}_{ij} = \frac{\mathbf{I}}{\zeta}\delta_{ij} + \mathbf{G}(\mathbf{r}_i; \mathbf{r}_j)\left(1 - \delta_{ij}\right), \tag{A.2}$$

where $\mathbf{G}$ is the Oseen tensor introduced in Eq. (3.6). Furthermore, the fluctuation-dissipation theorem governing the statistics of Brownian displacements becomes:

$$\langle \boldsymbol{\xi}_i(t) \rangle = \mathbf{0}, \quad \langle \boldsymbol{\xi}_i(t)\boldsymbol{\xi}_j(t') \rangle = 2k_{\mathrm{B}}T\mathbf{M}_{ij}\delta(t - t'). \tag{A.3}$$

In practice, $\boldsymbol{\xi}_i$ is calculated as

$$\boldsymbol{\xi}_i(t) = \sum_{j=1}^{N} \mathbf{B}_{ij} \cdot \mathbf{w}_j, \tag{A.4}$$

where $\mathbf{w}_j$ is an uncorrelated Gaussian white noise with zero mean and unit variance, and the tensor $\mathbf{B}_{ij}$ is related to the grand mobility tensor as

$$\sum_{p=1}^{N} \mathbf{B}_{ip} \cdot \mathbf{B}_{jp}^{T} = 2k_{\mathrm{B}}T\mathbf{M}_{ij}. \tag{A.5}$$

We compute $\mathbf{B}_{ij}$ as the lower triangular Cholesky factor of $\mathbf{M}_{ij}$. An additional complication in the presence of hydrodynamic interactions arises from the calculation of tensions: indeed, Eq. (3.11) now involves a full matrix instead of a tridiagonal system, which we solve using LU decomposition.
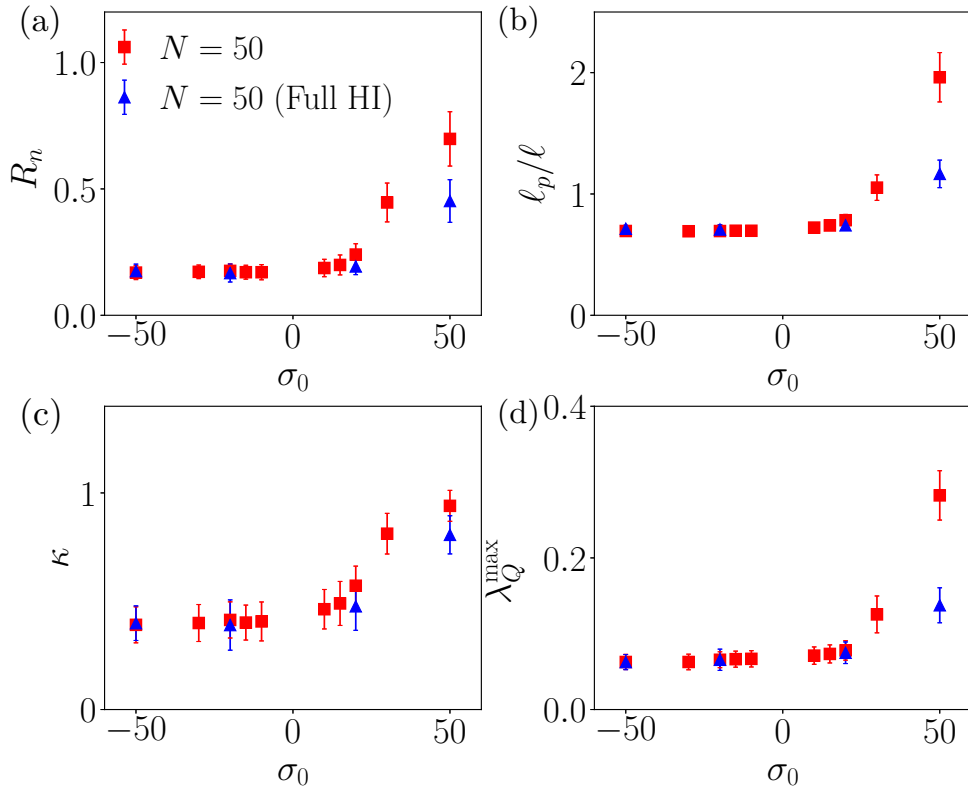
Figure A.1: Comparison of structural properties similar to Fig. 3.4 (by solving Eq. 3.1) with (full) in the legend corresponds to Eq. A.1 for parameter values with $N = 50$, $k_{\mathrm{on}} = 200$ and $k_{\mathrm{off}} = 500$.

Figure A.1 shows a comparison of conformational properties in simulations with and without hydrodynamic interactions. We find that all the qualitative trends reported in Sec. 4.3 remain the same, but that the spontaneous stretching induced by activity in extensile systems becomes weaker due to the increased viscous dissipation in the system.

Appendix B

Details of the computational model

In the following appendix, we will outline some of the aspects of the model that is used in Chapter 4. We will start with describing the FENE polymer model for the backbone chromatin chain followed by a summary of the computational algorithm based on boundary integral formulation; a more detailed version of which can be seen in Appendix C. The algorithm for evaluating the Hi-C proximity map is outlined at the end.

B.1   Chain mechanics: deterministic forces

The spring forces $\mathbf{F}_i^s$ in Eq. (4.2) are modeled using the FENE spring law [116], which gives linear Hookean behavior at short extensions but prevents stretching beyond a maximum extension n_0. Within a given chain, the net spring force on bead i is

$$\mathbf{F}_i^s = \frac{H_c \mathbf{n}_i}{1 - (n_i/n_0)^2} - \frac{H_c \mathbf{n}_{i-1}}{1 - (n_{i-1}/n_0)^2}, \tag{B.1}$$

where $\mathbf{n}_i = \mathbf{x}_{i+1} - \mathbf{x}_i$ is the connector from bead i to $i+1$ and H_c is the entropic spring constant. Crosslink forces $\mathbf{F}_i^c$ are captured using the same force law, but with a stiffer spring constant of $10 H_c$.

114

Excluded volume forces $\mathbf{F}_i^e$ prevent overlap of distinct sections of the polymer and are captured using a soft repulsive potential:

$$\mathbf{F}_i^e = -\sum_{j \neq i} \nabla_i \Phi(\mathbf{x}_i - \mathbf{x}_j), \quad \text{with} \quad \Phi(\mathbf{x}) = \frac{\Phi_0}{|\mathbf{x}|^n}, \tag{B.2}$$

with $n = 3$. The choice of the parameter Φ_0 is ad hoc and chosen to ensure that the chain does not cross itself. The potential is truncated whenever $|\mathbf{x}_i - \mathbf{x}_j| > \ell_s$, where ℓ_s is the equilibrium spring length, and three additional equally-spaced repulsive nodes are placed along each link in addition to the beads when calculating these interactions. A cell list algorithm is employed for efficient calculation of these forces with $O(N)$ complexity [188].

B.2 Hydrodynamic interactions

The calculation of the nucleoplasmic flow field $\mathbf{u}$ appearing in the Langevin equation (4.1) involves solving the Stokes equation (4.4) subject to the no-slip condition on the nuclear envelope and evaluating the solution at the location of each bead. Due to the linearity of the Stokes equations, that solution can be written in terms of a Green's function $\mathbf{G}$ as

$$\mathbf{u}(\mathbf{x}_i) = \sum_{j=1}^{N} \mathbf{G}(\mathbf{x}_i; \mathbf{x}_j) \cdot \left(\mathbf{F}_j + \mathbf{F}_j^a\right), \tag{B.3}$$

where the forces on the right-hand side are known. While analytical expressions for $\mathbf{G}$ exist in spherical domains [9, 133], a numerical solution is required in the spheroidal domains considered here. Rather than evaluating $\mathbf{G}$ directly, we instead decompose the velocity of Eq. (B.3) into two parts [189]: $\mathbf{u} = \mathbf{u}^s + \mathbf{u}^c$. The first contribution is defined as the velocity induced by the distribution of point forces in free space,

$$\mathbf{u}^s(\mathbf{x}) = \sum_{j=1}^{N} \mathbf{G}^s(\mathbf{x}; \mathbf{x}_j) \cdot \left(\mathbf{F}_j + \mathbf{F}_j^a\right), \tag{B.4}$$

expressed in terms of the Oseen tensor or Stokeslet

$$\mathbf{G}^s(\mathbf{x}; \mathbf{x}_0) = \frac{1}{8\pi\eta} \left(\frac{\mathbf{I}}{|\mathbf{x} - \mathbf{x}_0|} + \frac{(\mathbf{x} - \mathbf{x}_0)(\mathbf{x} - \mathbf{x}_0)}{|\mathbf{x} - \mathbf{x}_0|^3} \right). \tag{B.5}$$

The second contribution $\mathbf{u}^c$ is a correction velocity calculated to satisfy the correct bound-ary condition. Note that $\mathbf{u}^c$ satisfies the homogeneous Stokes equations with boundary condition $\mathbf{u}^c(\mathbf{x}) = -\mathbf{u}^s(\mathbf{x})$ for $\mathbf{x} \in S$. It can be calculated as a single-layer boundary integral equation for Stokes flow [128]:

$$\mathbf{u}^c(\mathbf{x}) = -\int_S \mathbf{G}(\mathbf{x}; \mathbf{x}_0) \cdot \mathbf{f}(\mathbf{x}_0) \, \mathrm{d}S(\mathbf{x}_0), \tag{B.6}$$

where $\mathbf{f}(\mathbf{x}_0)$ is an unknown traction distribution on the surface of the domain boundary. Evaluating Eq. (B.6) on the surface S and using the boundary condition $\mathbf{u}^c(\mathbf{x}) = -\mathbf{u}^s(\mathbf{x})$ yields an integral equation for the traction field $\mathbf{f}$ that can be solved numerically. Once $\mathbf{f}$ is known on the surface for a given point force distribution, the velocity correction $\mathbf{u}^c$ is obtained by evaluating Eq. (B.6) at the locations $\mathbf{r}_i$ of the beads, and can be added to the free-space velocity $\mathbf{u}^s$ of Eq. (B.4) to provide the desired velocity (B.3). The boundary integral equation (B.6) is evaluated by quadrature after discretization of the surface into a mesh of 6-node triangular elements [128]. The algorithm was tested by comparison to the analytical Green's function inside a spherical domain [133] (see Appendix C for more details). Simulations shown were performed with 5120 elements, with a numerical error of less than 2%. Finally, the calculation of both $\mathbf{u}^s$ and $\mathbf{u}^c$ is accelerated using a kernel-free fast multipole algorithm [136, 137, 190], resulting on an overall $O(N)$ complexity with respect to the total number of beads in the system. For a more detailed discussion on the present numerical pipeline, readers can refer to Appendix C.

B.3   Thermal fluctuations

The Brownian displacements $\boldsymbol{\xi}_i(t)$ in Eq. (4.1) are calculated to satisfy the fluctuation-dissipation theorem, which specifies their mean and variance as

$$\langle \boldsymbol{\xi}_i(t) \rangle = \mathbf{0}, \quad \langle \boldsymbol{\xi}_i(t)\boldsymbol{\xi}_j(t') \rangle = 2k_BT\mathbf{M}_{ij}\delta(t - t'), \tag{B.7}$$

where $\mathbf{M}_{ij}$ denotes the grand mobility tensor that captures viscous resistance on the chain as well as long-ranged hydrodynamic interactions:

$$\mathbf{M}_{ij} = \zeta^{-1}\mathbf{I}\delta_{ij} + \mathbf{G}(\mathbf{x}_i; \mathbf{x}_j)\left(1 - \delta_{ij}\right). \tag{B.8}$$

Equation (B.10) is satisfied by calculating the Brownian displacements as

$$\boldsymbol{\xi}_i(t) = \sum_{j=1}^{N} \mathbf{B}_{ij} \cdot \mathbf{w}_j, \tag{B.9}$$

where $\mathbf{w}_j$ is an uncorrelated Gaussian white noise with zero mean and unit variance, and the tensor $\mathbf{B}_{ij}$ is related to the grand mobility tensor as

$$\sum_{p=1}^{N} \mathbf{B}_{ip} \cdot \mathbf{B}_{jp}^T = 2k_BT\mathbf{M}_{ij}\,. \tag{B.10}$$

In general, solving for $\mathbf{B}_{ij}$ from Eq. (B.10) involves either a costly Cholesky decomposition, an iterative scheme such as the Lanczos method [119], or a numerical approximation [191]. In the present work, we make the local approximation $\mathbf{M}_{ij} \approx \zeta^{-1}\mathbf{I}\,\delta_{ij}$ when calculating Brownian fluctuations, and under this approximation the right-hand side in Eq. (B.10) becomes $2D_b\mathbf{I}\delta_{ij}$, where $D_b = k_BT/\zeta$ is the Brownian diffusivity of one bead in isolation. Numerical comparison between the full solution of Eq. (B.10) using the Lanczos method and the local approximation were carried out in small systems and showed negligible differences in the relevant statistical quantities.

B.4 Scalings and parameters

In all the results of Sec. 4.3, we scale lengths with the equilibrium length ℓ_s of a FENE spring, forces by the corresponding spring force F_s, and times by the characteristic time t_s for one isolated bead to diffuse a distance of ℓ_s:

$$\ell_s = \sqrt{\frac{k_B T}{H_c}}, \quad F_s = \sqrt{k_B T H_c}, \quad t_s = \frac{\zeta}{H_c}. \tag{B.11}$$

Note that t_s is also the spring relaxation time. Upon scaling of the system of equations, the dimensionless parameters governing the dynamics of the system are the dimensionless rate constants for active and crosslink forces, the dimensionless hydrodynamic radius a_h/ℓ_s, the dimensionless maximum spring extension n_0/ℓ_s, and the dimensionless active dipole strength

$$\sigma_0 = \frac{f^a}{\sqrt{k_B T H_c}}. \tag{B.12}$$

All simulations shown are for $M_c = 23$ chains of $N_b = 1305$ beads (total of 30,015 beads), with four alternating blocks of active euchromatin (945 beads) and passive heterochromatin (360 beads) per chain, for a fraction $\alpha_c \approx 0.28$ of heterochromatin. The dimensionless effective radius of the nucleus is $R_s = 28$, and its eccentricity is $e = 0.36$. The hydrodynamic bead radius is $a_h/\ell_s = 0.1$, the maximum spring extension is $n_0/\ell_s = 2.5$, and the various dimensionless rate constants are set to $k_{on}^c = 0.02$, $k_{on}^a = 2.0$, and $k_{off}^a = 5.0$. The corresponding fraction of active links along ECDs is $p_a = 0.285$.

B.5 Hi-C map calculation

The algorithm used to calculate the Hi-C proximity maps of Fig. 4.5 follows [44,192] and is based on the spatial distance between pairs of genomic loci along the chromatin chains. Specifically, entries in the matrix are evaluated based on a Gaussian kernel, such

that

$$H_{ij} = \frac{1}{\sigma\sqrt{2\pi}} \exp(-r_{ij}^2/2\sigma^2), \tag{B.13}$$

where $r_{ij} = |\mathbf{x}_i - \mathbf{x}_j|$ is the distance between beads i and j, and where we choose a standard deviation of $\sigma = 6$ for the Gaussian. In practice, successive beads along the chains are binned into groups of 5, and the entries H_{ij} are averaged over each bin to generate a matrix of linear size $N_b/5 = 261$ per chromosome. This matrix is then shown as a color plot in Fig. 4.5(a,b), using a linear color map from white to red (or pink) over the range of values of the matrix entries. Green dots on the diagonal in Fig. 4.5(a,b) highlight sections of the chromosomes that are spatially located inside HCRs, where a dot is added to the Hi-C map if at least 2 beads out of 5 inside a given bin fall inside an HCR.

Appendix C

Numerical algorithm and benchmarking of boundary element method

In the following appendix, we will discuss the details of computational methods and algorithms for systematically calculating the flow field using boundary integral methods by extending the discussion from chapter 1 on Stokes flow. This is used to evaluate $\mathbf{u}(\mathbf{x}_i, t)$ in Chapter 4 (equation 4.1). As mentioned in Chapter 4, the nuclear envelope, which encloses the chains, is modeled as a prolate spheroidal cavity with bounding surface S of eccentricity e and equivalent radius R_s, and is filled with a viscous Newtonian nucleoplasm with viscosity η. Each chromosome is coarse-grained as an active Zimm bead-spring chain composed of N_b beads of hydrodynamic radius a_h connected by finitely extensible elastic springs. Finally, we will summarize and benchmark the performance of our simulation tool box.

C.1   Numerical details: boundary integral formulation

Here we extend the hydrodynamics section with a more detailed discussion for an arbitrary system where the direct analytical expression of the Green's function are not available or for a large system such as ours. A convenient point for deriving the boundary integral equation is the Lorentz reciprocal identity stating that for any two non-singular flows $\boldsymbol{u}$ and $\boldsymbol{u}'$ with corresponding stress tensors $\boldsymbol{\sigma}$ and $\boldsymbol{\sigma}'$ [128],

$$\frac{\partial}{\partial x_k}(u_i'\sigma_{ik} - u_i\sigma_{ik}') = 0 \tag{C.1}$$

where the $\boldsymbol{u}'$ represents the flow due to a point force ($\mathbf{f}$) in free space located at point $\mathbf{x}_0$. Due to linearity of the Stokes equations, they can be related as following,

$$\boldsymbol{u}'(\boldsymbol{x}) = \frac{1}{8\pi\mu}\mathbf{G}(\boldsymbol{x}, \boldsymbol{x}_0) \cdot \boldsymbol{f}, \qquad \boldsymbol{\sigma}'(\boldsymbol{x}) = \frac{1}{8\pi}\mathsf{T}(\boldsymbol{x}, \boldsymbol{x}_0) \cdot \boldsymbol{f}. \tag{C.2}$$

Substituting into Eq. C.1, we will obtain

$$\frac{\partial}{\partial x_k}[\mathbf{G}(\boldsymbol{x}, \boldsymbol{x}_0) \cdot \boldsymbol{\sigma}(\boldsymbol{x}) - \mu\boldsymbol{u} \cdot \mathsf{T}(\boldsymbol{x}, \boldsymbol{x}_0)] = 0. \tag{C.3}$$

Now, for a control volume V that is bounded by the closed surface S, using the divergence theorem we can convert the volume integral over V into a surface integral over S,

$$\int_S [\mathbf{G}(\boldsymbol{x}, \boldsymbol{x}_0) \cdot \boldsymbol{\sigma}(\boldsymbol{x}) - \mu\boldsymbol{u} \cdot \mathsf{T}(\boldsymbol{x}, \boldsymbol{x}_0)] = 0. \tag{C.4}$$

Note that S may be composed of fluid surfaces, fluid interfaces, or solid surfaces. In the present work, we will only deal with solid surfaces which does not deform under external or internal shear, and any function inside the domain is regular throughout V. A small spherical volume of infinitesimally small radius ϵ is then introduced around evaluation point $\boldsymbol{x}_0$. The above integral is then valid over the boundary S and the small spherical

volume S_ϵ. It can be shown that as the spherical volume becomes smaller $\epsilon \to 0$, the surface integral over the small spherical volume becomes equal to $8\pi\mu u_j$. Using the symmetry of the Green's function $G_{ij}(\boldsymbol{x}, \boldsymbol{x}_0) = G_{ji}(\boldsymbol{x}_0, \boldsymbol{x})$, we can convert the above expression to,

$$u_j(\boldsymbol{x}_0) = -\frac{1}{8\pi\mu} \int_S G_{ji}(\boldsymbol{x}_0, \boldsymbol{x}) f_i(\boldsymbol{x}) \mathrm{d}S(\boldsymbol{x}) + \frac{1}{8\pi} \int_S u_i(\boldsymbol{x}) T_{ijk}(\boldsymbol{x}, \boldsymbol{x}_0) n_k \mathrm{d}S(\boldsymbol{x}). \qquad (\text{C.5})$$

The first integral on the right hand side represents a distribution of Stokeslet on the boundaries and is also called as single layer potential while the second integral represents a distribution of stresslets and is called a double layer potential and when the point $\boldsymbol{x}_0$ is located on the boundary results in the following expression,

$$u_j(\boldsymbol{x}_0) = -\frac{1}{4\pi\mu} \int_S G_{ji}(\boldsymbol{x}_0, \boldsymbol{x}) f_i(\boldsymbol{x}) \mathrm{d}S(\boldsymbol{x}) + \frac{1}{4\pi} \int_S u_i(\boldsymbol{x}) T_{ijk}(\boldsymbol{x}, \boldsymbol{x}_0) n_k \mathrm{d}S(\boldsymbol{x}), \qquad (\text{C.6})$$

with following useful properties,

$$\int_S T_{ijk}(\boldsymbol{x}, \boldsymbol{x}_0) n_k(\boldsymbol{x}) \mathrm{d}S(\boldsymbol{x}) = \begin{bmatrix} 8\pi \\ 4\pi \\ 0 \end{bmatrix} \delta_{ij}, \qquad (\text{C.7})$$

for a point $\boldsymbol{x}_0$ located inside, right on, or outside S respectively, and integral of the Green's function over the surface $\int_S G_{ij}(\boldsymbol{x}, \boldsymbol{x}_0) n_j(\boldsymbol{x}) \mathrm{d}S(\boldsymbol{x}) = 0$. We now focus our attention to the boundary element method which underlies the numerical framework for solving boundary integral equations shown above. Analytical solutions for an arbitrary domain are feasible only for a limited number of boundary geometries and types of flow. To compute the solution under general conditions, we must resort to numerical approaches. In the first step, we trace the domain of the integral equation S with a network of marker points or nodes, and approximate S using a set of boundary elements that are defined with respect to the nodes. In the second step, we can approximate the unknown boundary velocity $\boldsymbol{u}$, surface force $\boldsymbol{f}$ over each boundary element using a truncated polynomial expansion in terms of properly defined surface variables. The main advantages of the

boundary element method over other numerical methods like finite element, finite volume or finite differences is the reduction of the solution by one dimension when compared to the physical space [129, 130]. Since the boundary integral formulation is an exact solution to the governing equations, the numerical solution tends to be highly accurate when compared to other numerical methods. However, the linear systems obtained by boundary element method are dense which can impose restrictions on the size of the system unless other advanced computational techniques like fast multipole methods [131], iterative solvers like GMRES [132], Lanczos method [119] etc. are used. As boundary integral equations are formed using fundamental solutions of the governing equations, they tend to be singular and these singularities need to be accurately treated numerically or analytically. For a reader who is specifically interested in the problems presented in the thesis, a detailed discussion on the development of the computational can be found in the following sections, and for more general derivations and applications of the boundary element method to potential and Stokes flow problems can be found in literature [128].

C.2   Boundary element representation: discretization

An important stage in the numerical implementation of a boundary integral method is the representation of the boundary of the flow by a set of boundary elements or discretization of the surface into marker points or nodes. This not only allows the computation of the required boundary integrals but also provides framework for expanding the unknown boundary function in a series of local basis function. For simple two-dimensional flow, the surface may be represented simply by a planar line that resides in a meridional plane or in the plane of the flow as shown in figure C.1. To set up boundary elements representations, we trace the planar line with a set of marker points $\boldsymbol{x}_i$, $i = 1, ..., N$. For first approximation, we represent the line with a set of straight segments that pass through successive

pairs of marker points. The straight segment passing through the points $\boldsymbol{x}$ and $\boldsymbol{x}_{i+1}$ is described by the equation $y = a_i x + b_i$ where $a_i = (y_{i+1} - y_i)/(x_{i+1} - x_i)$, and $b_i = y_i - a_i x_i$. The differential arc length over the ith segment is given by

$$dl = (a_i^2 + 1)^{1/2}|\mathrm{d}x| = \alpha(a_i^2 + 1)^{1/2}\mathrm{d}x, \tag{C.8}$$

where $\alpha = (x_{i+1} - x_i)/|x_{i+1} - x_i|$. The line integral of a function f over the ith straight segment is given by,

$$\int_S f(x, y)dl = \alpha(a_i^2 + 1)^{1/2} \int_{x_i}^{x_{i+1}} f(x, a_i x + b_i)\mathrm{d}x, \tag{C.9}$$

and the unit normal and tangent vectors are given by

$$\mathbf{t} = \frac{\alpha}{(1 + a_i^2)^{1/2}}(1, a_i) \qquad \mathbf{n} = \frac{\alpha}{(1 + a_i^2)^{1/2}}(a_i, -1). \tag{C.10}$$
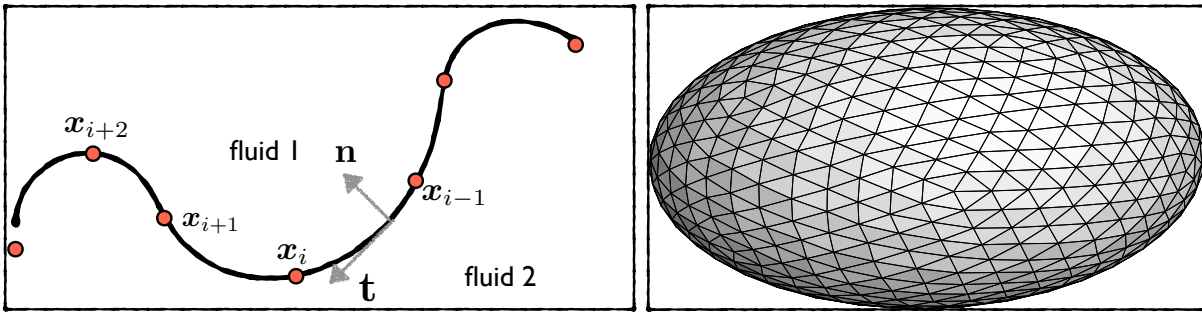
Figure C.1: Discretized mesh in 2D (left) for intuition, the surface is represented by a planar line, and disretized by a set of marker points. Discretization in 3D (right) of an ellipsoid: $N_\Delta = 1280$ six-node triangular elements.

Now that we have the intuition on how the discretization of a 2D surface is performed, let's move to three dimensional surface. For three dimensional problems, the general strategy is to trace the boundaries with a network of nodes, and to represent the boundaries with a collection of elements that defined in terms of a set of neighboring nodes as shown in figure C.1. But before we do that, it is necessary to review some fundamental

concepts of differential geometry of surfaces. One way to describe a three dimensional surface is to introduce a right handed curvilinear, but not necessarily orthogonal, coordinate system (η, ξ) described over the surface, and to view the position of a point $\boldsymbol{x}$ on the surface as a function of η, ξ namely $\boldsymbol{x}(\eta, \xi)$. A unit vector tangential to the surface is given by,

$$\mathbf{t} = \frac{1}{h_t}\left(\frac{\partial \boldsymbol{x}}{\partial \eta} + \omega \frac{\partial \boldsymbol{x}}{\partial \xi}\right) \qquad h_t = \left|\frac{\partial \boldsymbol{x}}{\partial \eta} + \omega \frac{\partial \boldsymbol{x}}{\partial \xi}\right|, \tag{C.11}$$

where ω is a constant.
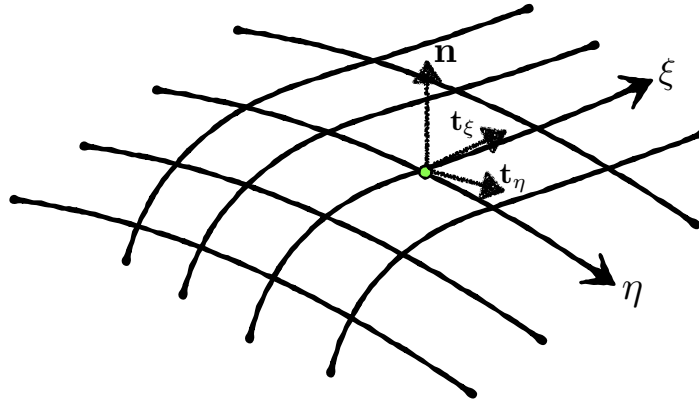
Figure C.2: Parametric representation of a three-dimensional surface using two surface variables (η, ξ).

The tangent vectors pointing toward the positive direction of an η or a ξ line are denoted by $\mathbf{t}_\eta$ and $\mathbf{t}_\xi$ and correspond to $\omega = 0$ or $\omega = \infty$ respectively. The unit vector normal to the surface is given by

$$\mathbf{n} = \frac{1}{h_n}\left(\frac{\partial \boldsymbol{x}}{\partial \eta} \times \frac{\partial \boldsymbol{x}}{\partial \xi}\right) \qquad h_n = \left|\frac{\partial \boldsymbol{x}}{\partial \eta} \times \frac{\partial \boldsymbol{x}}{\partial \xi}\right| \tag{C.12}$$

The differential area of the surface element can be written as

$$\mathrm{d}S = h_n \, \mathrm{d}\eta \, \mathrm{d}\xi \tag{C.13}$$

The integral of a function f over the surface is given by

$$\int_S f(\boldsymbol{x})\mathrm{d}S(\boldsymbol{x}) = \int_S f(\boldsymbol{x}(\eta,\xi))h_n \; \mathrm{d}\eta \; \mathrm{d}\xi \tag{C.14}$$

The differential length of an infinitesimal line element on the surface is given by

$$\mathrm{d}l^2 = \mathrm{d}\boldsymbol{x} \cdot \mathrm{d}\boldsymbol{x} = \left(\frac{\partial \boldsymbol{x}}{\partial \eta}\mathrm{d}\eta + \frac{\partial \boldsymbol{x}}{\partial \xi}\mathrm{d}\xi\right) \cdot \left(\frac{\partial \boldsymbol{x}}{\partial \eta}\mathrm{d}\eta + \frac{\partial \boldsymbol{x}}{\partial \xi}\mathrm{d}\xi\right) \tag{C.15}$$

$$= \frac{\partial \boldsymbol{x}}{\partial \eta} \cdot \frac{\partial \boldsymbol{x}}{\partial \eta}\mathrm{d}\eta^2 + 2\frac{\partial \boldsymbol{x}}{\partial \eta} \cdot \frac{\partial \boldsymbol{x}}{\partial \xi}\mathrm{d}\eta \; \mathrm{d}\xi + \frac{\partial \boldsymbol{x}}{\partial \xi} \cdot \frac{\partial \boldsymbol{x}}{\partial \xi}\mathrm{d}\xi^2 \tag{C.16}$$

If η and ξ are orthogonal, then the second term on the right hand side is 0, and we can write the differential arc length in an alternative form

$$\mathrm{d}l = h_t|\mathrm{d}\eta|, \qquad \text{where} \qquad h_t = (a_{\eta\eta} + 2a_{\eta\xi}\omega + a_{\xi\xi}\omega^2)^{1/2} \tag{C.17}$$

where

$$a_{\eta\eta} = \frac{\partial \boldsymbol{x}}{\partial \eta} \cdot \frac{\partial \boldsymbol{x}}{\partial \eta} \quad a_{\eta\xi} = \frac{\partial \boldsymbol{x}}{\partial \eta} \cdot \frac{\partial \boldsymbol{x}}{\partial \xi} \quad a_{\xi\xi} = \frac{\partial \boldsymbol{x}}{\partial \xi} \cdot \frac{\partial \boldsymbol{x}}{\partial \xi} \tag{C.18}$$

C.3 Three-dimensional boundary elements

Moving from the parametric representation of 3D surfaces, we will now consider representation of three dimensional boundaries.
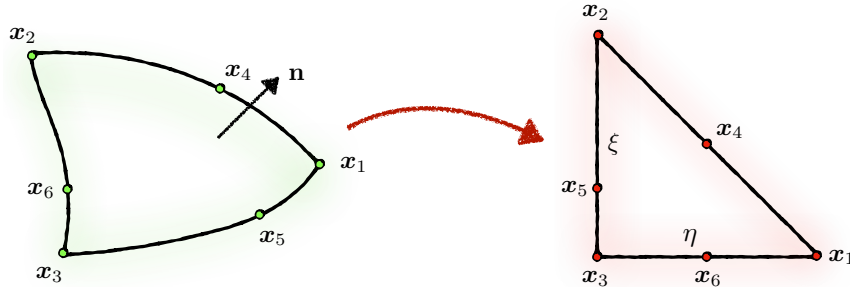

Figure C.3: Mapping of a curved triangle in physical space onto a right triangle in the $\eta\xi$-plane.

The elements may be chosen to have a variety of shapes but we will stick to curved triangles which is a second order approximation. We discretize the boundary into a set of curved triangles. Each triangle is defined by six nodes or marker points $\boldsymbol{x}_i, i = 1, .., 6$ as shown in figure C.3. To describe the surface of a triangle we use a parametric representation in terms of two variables η and ξ as

$$\boldsymbol{x}(\eta, \xi) = \boldsymbol{a} + \boldsymbol{b}\eta + \boldsymbol{c}\xi + \boldsymbol{d}\eta^2 + \boldsymbol{e}\xi^2 + \boldsymbol{f}\eta\xi \tag{C.19}$$

where η and ξ take values over the right isosceles triangle depicted on the right of figure C.3. To ensure that the curved triangle passes through six marker points, we require

$$\boldsymbol{x}(1,0) = \boldsymbol{x}_1 \qquad \boldsymbol{x}(0,1) = \boldsymbol{x}_2 \qquad \boldsymbol{x}(0,0) = \boldsymbol{x}_3 \tag{C.20}$$

$$\boldsymbol{x}(\gamma, 1 - \gamma) = \boldsymbol{x}_4 \qquad \boldsymbol{x}(0, \beta) = \boldsymbol{x}_5 \qquad \boldsymbol{x}(\alpha, 0) = \boldsymbol{x}_6 \tag{C.21}$$

where the three scalar coefficients α, β and γ are defined as

$$\alpha = \frac{1}{1 + \frac{|\boldsymbol{x}_6 - \boldsymbol{x}_1|}{|\boldsymbol{x}_6 - \boldsymbol{x}_3|}} \qquad \beta = \frac{1}{1 + \frac{|\boldsymbol{x}_5 - \boldsymbol{x}_2|}{|\boldsymbol{x}_5 - \boldsymbol{x}_3|}} \qquad \gamma = \frac{1}{1 + \frac{|\boldsymbol{x}_4 - \boldsymbol{x}_1|}{|\boldsymbol{x}_4 - \boldsymbol{x}_2|}} \tag{C.22}$$

The 3-1 side of the triangle is mapped on the η-axis, the 2-3 side is mapped onto the ξ-axis, and 1-2 side is mapped onto the diagonal line. Substituting equation (C.20) into equation (C.19), solving for the unknown coefficients $\boldsymbol{a} - \boldsymbol{f}$, we obtain a representation in terms of six local basis functions, namely

$$\boldsymbol{x}(\eta, \xi) = \sum_{i=1}^{6} \boldsymbol{x}_i \phi_i(\eta, \xi) \tag{C.23}$$

where

$$\phi_1 = \frac{\alpha}{\alpha - 1}\eta \left[\frac{1}{\alpha}\eta - 1 + \frac{(\alpha - \gamma)}{\alpha(1 - \gamma)\xi} \right] \qquad \phi_2 = \frac{\beta}{\beta - 1}\xi \left[\frac{1}{\beta}\xi - 1 + \frac{(\beta + \gamma - 1)}{\beta\gamma\eta} \right] \tag{C.24}$$

$$\phi_3 = \frac{1}{\gamma(1 - \gamma)}\eta\xi \qquad \phi_4 = \frac{1}{\beta(1 - \beta)}\xi(1 - \eta - \xi) \tag{C.25}$$

127

$$\phi_5 = \frac{1}{\alpha(1-\alpha)}\eta(1-\eta-\xi) \qquad \phi_6 = 1 - \phi_1 - \phi_2 - \phi_3 - \phi_4 - \phi_5 \qquad \text{(C.26)}$$

In the event when the triangle in the physical space is markedly skewed, or when one middle marker point along a side of the triangle does not lie sufficiently close to the straight line that connects the corresponding vertices, the mapping might contain singular points. It can be avoided by making sure that the determinant of the metric tensor at several points over the element is a positive number not very close to zero.

C.4 Numerical computation of boundary integral

One important task in the series of the entire framework is the calculation of the single and double layer integrals over the boundary elements.
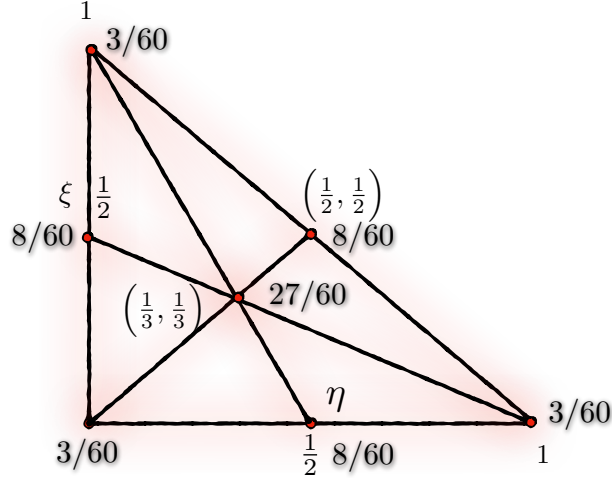
Figure C.4: A cubic quadrature to compute a 2D integral over a triangle using seven base points. The weights in bold corresponding to the seven base points are used in gaussian quadrature

To compute the integrals at a point located away from an element, we use Gaussian quadrature, a standard numerical method for computing a boundary integral over a planar or curved triangle. The triangle is mapped from the physical space to the η, ξ space, and

the boundary integral is approximated with a finite weighted sum as,

$$\int_{triangle} f(\boldsymbol{x})\mathrm{d}S(\boldsymbol{x}) = \int_{triangle} g(\eta,\xi)\mathrm{d}\eta\mathrm{d}\xi \approx \frac{1}{2}\sum_{n=1}^{n=7} g(\eta_n, \xi_n)w_n \qquad (\text{C.27})$$

where $g = fh_n$. The coordinates of the base points and the corresponding weights are indicated in figure C.4. To compute accurately a boundary integral at a point located on an element, we must account for the singularity arising due to Stokeslet and Stresslet.

C.5 Computational pipeline and algorithm

Now that we have formalized the relevant details in the preceding sections, we can focus on how it is relevant to the system of interest given in Chapter 4. As you have seen in the previous sections, the problem setup involves an active polymer inside a bounding surface S with multiple external forces acting on the polymer at the location of the beads x_i. In order to calculate the flows $\boldsymbol{u}$ inside the system, we need to find the distribution of traction forces $\boldsymbol{\sigma} \cdot \mathbf{n}$ on the surface S.

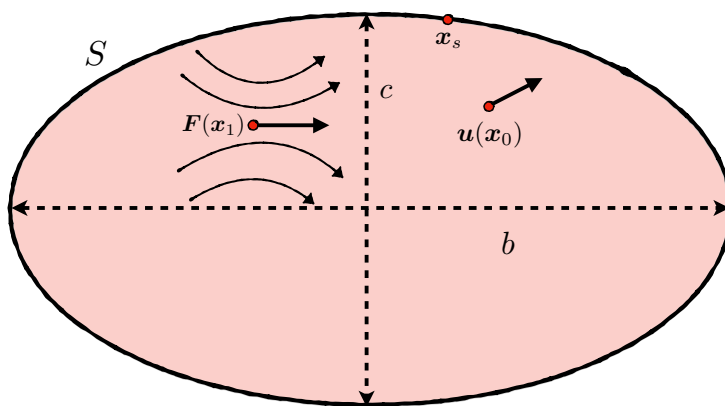**Figure C.5**: Representation of the velocity induced by a point force $(\boldsymbol{x}_1)$ inside an ellipsoid shell of equivalent radius R_s. To gain understanding of the computational pipeline, we have constructed a simple picture of a single point force inside the bounding surface S. The point force will induce a flow inside the domain which satisfies the no-slip condition at the wall.

In the present study, we will reduce equation (C.5) to only account for the single layer potential on the basis of the ansatz that it is always possible to find an external complimentary flow so that it has the same boundary values on D [128]. Rewriting the integral equations,

$$\boldsymbol{u}(\boldsymbol{x}_0) = -\frac{1}{8\pi\mu} \int_D \mathbf{G}(\boldsymbol{x}_0; \boldsymbol{x}) \cdot \boldsymbol{f}(\boldsymbol{x}) \, \mathrm{d}S(\boldsymbol{x}) \tag{C.28}$$

In the presence of a closed confinement as shown in the figure C.5, a direct analytical expression for the Green's function to correct for the no-slip boundary condition at the wall is not known to the best of our knowledge. In order to make further progress, we will use the following procedure to evaluate the traction forces ($\boldsymbol{f}(\boldsymbol{x})$) on the surface which can be used in equation (C.28) to calculate the velocities at any point inside the domain. A two-dimensional cross section of the domain is shown for simplicity in figure C.5 but the algorithm works for three dimensional surface.

- We will consider a simple system with a single point force at position $\boldsymbol{x}_1$ which can induce a flow inside the bounding S due to hydrodynamic interactions. In free space, we can linearly relate the velocity in terms of external forcing with a proportionality tensor known as the Stokeslet. But in the presence of a bounding surface, we need to know a priori the condition on the surface. The most commonly used condition is the no-slip condition which means that the fluid particle at the wall should move with the velocity of the wall.

- In case of stationary wall like the one shown above, the velocity on the wall $\boldsymbol{u}(\boldsymbol{x}_s)$ = 0 where $\boldsymbol{x}_s$ is any point on the surface. The total velocity field $\boldsymbol{u}(\boldsymbol{x}_0)$ due to a point force $\boldsymbol{F}(\boldsymbol{x}_1)$ at a point ($\boldsymbol{x}_1$) (see figure C.5) inside the confinement is the sum of velocity $\boldsymbol{u}^s(\boldsymbol{x}_0)$ induced by a Stokelset (calculated using the free space Green's function or Oseen tensor), and a correction term $\boldsymbol{u}^c(\boldsymbol{x}_0)$ to account for the presence

of the boundary,

$$u(\boldsymbol{x}_0) = \boldsymbol{u}^s(\boldsymbol{r}_0) + \boldsymbol{u}^c(\boldsymbol{x}_0). \qquad (C.29)$$

- On moving the point $(\boldsymbol{x}_0)$ to the surface such that $\boldsymbol{x}_0 = \boldsymbol{x}_s$, the total velocity becomes zero to satisfy the no-slip condition at the boundary such that,

$$\boldsymbol{u}^c(\boldsymbol{x}_s) = -\boldsymbol{u}^s(\boldsymbol{x}_s) = -\mathbf{G}(\boldsymbol{x}_s; \boldsymbol{x}_1) \cdot \boldsymbol{F}(\boldsymbol{x}_1), \quad \text{at} \quad \boldsymbol{x}_0 = \boldsymbol{x}_s \text{ (on the surface). } (C.30)$$

- Note that $\boldsymbol{u}^c$ satisfies the homogeneous Stokes equations with boundary condition $\boldsymbol{u}^c(\boldsymbol{x}_0) = -\boldsymbol{u}^s(\boldsymbol{x}_0)$ for $\boldsymbol{x}_0 \in S$. The above equation when plugged in equation (C.28) will result in the following expression,

$$\boldsymbol{u}^s(\boldsymbol{x}_s) = \frac{1}{8\pi\mu} \int_D \mathbf{G}(\boldsymbol{x}_s; \boldsymbol{x}) \cdot \boldsymbol{f}(\boldsymbol{x}) \mathrm{d}S(\boldsymbol{x}). \qquad (C.31)$$

The only unknown quantity in the above equation (C.31) are the tractions ($\boldsymbol{f}(\boldsymbol{x})$) on the surface of the domain which can be obtained by discretizing the surface and evaluating the integral using Gaussian quadratures using equation (C.27). The discretization involves triangulation of the surface into planar elements defined by six nodes based on successive sub-division of a regular icosahedron. This will result in a set of linear algebraic system of equations to solve for the unknown tractions. Once the tractions are known, the velocity correction $\boldsymbol{u}^c(\boldsymbol{x}_0)$ at any point $\boldsymbol{x}_0$ inside the domain can be calculated along with the total velocity by using equations (C.28) and (C.29) respectively.

C.6 Accuracy of the boundary integral methods

The accuracy of a boundary element method will depend on the shape and distribution of boundary elements. The accuracy will start to decline when the boundaries contain sharp corners, points or lines of discontinuous velocities. In these cases, the flow

will contain singularities associated with infinite values of the velocity, surface force, or the density of the hydrodynamic potential.
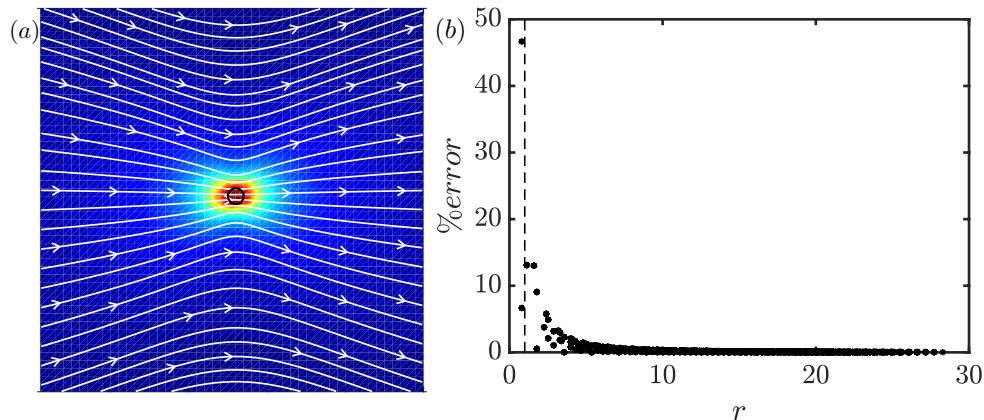

Figure C.6: (Left) Streamlines for translation of a sphere in a viscous fluid. Disturbance flow field induced by a translating sphere as given by the Eq. in the x-y plane. The size of the sphere $a = 1$ with force ($\boldsymbol{f} = F_0 e_x = 10\mathbf{e}_x$) acting in the positive x-direction. (Right) Decay of the % error with radial distance (r) from the center of the sphere where the dashed line shows the radius of the sphere.

Now, in order to optimize the accuracy of a boundary element computation, we need to distribute the boundary elements so as to minimize a suitably defined global or local error of the required variable. Considering the high accuracy of boundary integral methods, the next step is to compare the numerical computation with the analytical results available in the literature. Here, we have considered two different scenarios for comparison, one for the classical Stokes flow problem of a translating sphere in a viscous fluid or in mathematical terms velocity field in presence of a point force accounting for a finite size correction using the Rotne-Prager-Yamakawa (RPY) mobility tensor, and the second is to compare the velocity field in the presence of a point force inside a bounding sphere using boundary integral method with the flow field obtained using the analytical Green's function from the literature [133]. The first problem involves essentially solving the forced

Stokes equation,

$$\boldsymbol{\nabla} \cdot \boldsymbol{\sigma} = \boldsymbol{\nabla} p + \mu \boldsymbol{\nabla}^2 \boldsymbol{u} = -\boldsymbol{f}\delta(\boldsymbol{x}) \tag{C.32}$$

using either the stream-function or Fourier transform approach or we take the easier route of just writing the final expression,

$$\boldsymbol{u} = \frac{1}{8\pi\mu}\mathbf{G}\cdot\boldsymbol{f} \tag{C.33}$$

Figure C.6 (a) shows the fluid flow induced by the motion of the sphere in a viscous fluid.
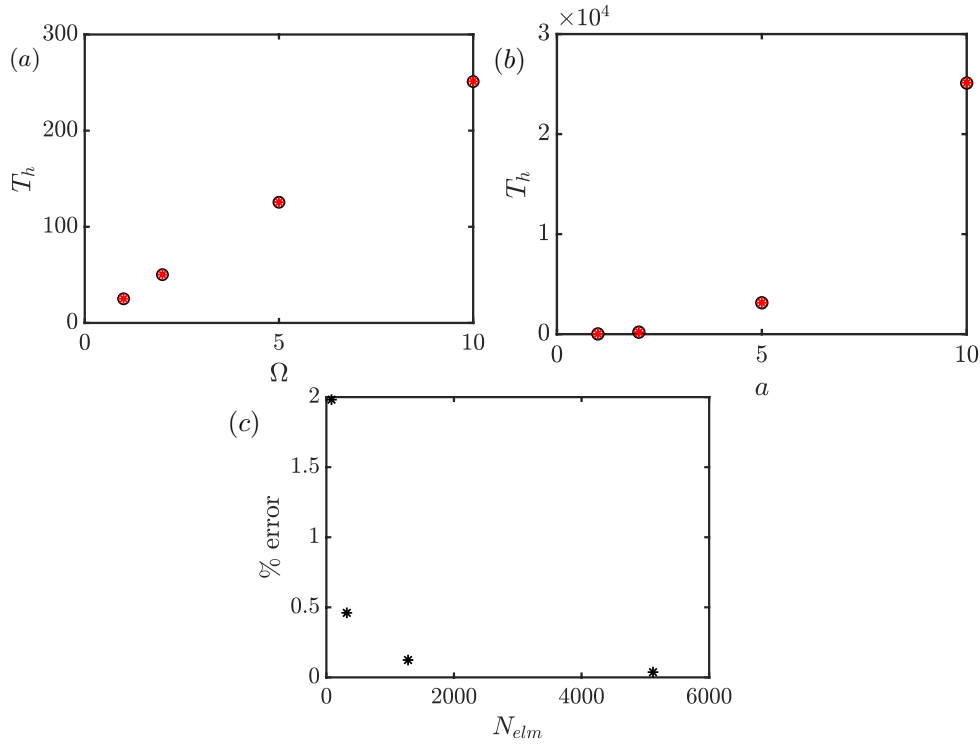
Figure C.7: Hydrodynamic torque acting on a sphere calculated using the boundary integral and comparing it with the analytical expression. a) shows the variation of torque with respect to angular velocity of the particle, (b) shows the variation with respect to size of the particle. There exists excellent agreement between the analytical and boundary integral solution with the error (c) decaying quadratically with number of elements on the surface (N_{elm})

Here we have considered a sphere of size $a = 1$ with force acting in the x-direction $\boldsymbol{f} = F_0 e_x = 10\mathbf{e}_x$. The flow lines are similar to the ones observed due to a Stokeslet. For

a quantitative comparison, we have also compared the % error in velocity magnitude at different radial locations r for number of nodes $= 5120$ as shown in figure C.6 (b).

Figure C.8: Comparison of the disturbance flows ($\boldsymbol{u}$) induced by a point force in x-y plane inside a sphere of radius $R_s = 8.0$. (a) is computed using the boundary integral method whereas (b) is obtained using the analytical expression for the Green's function ($\mathbf{G}$) for a point force inside a sphere [133]. The point force is located at $r = 15$ on the x-axi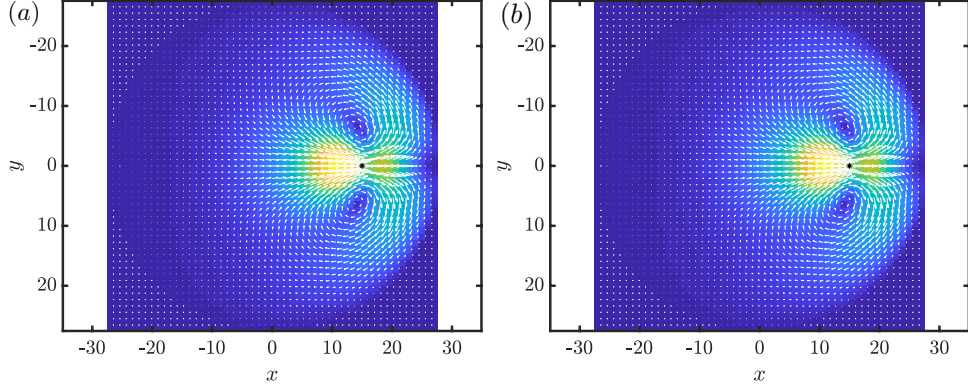s such that $x = 15, y = 0, z = 0$ shown as black star. The colormap shows the magnitude of the force distribution, and the vector plot shows the projections of the velocity field in a plane.

The error decays sharply away from the boundary, and increases very close to the surface which is very typical of boundary integral simulations, and can be improved with further discretization of the surface. We can also look at the hydrodynamic torque. The hydrodynamic force moment or torque of a spherical particle rotating with velocities $\boldsymbol{\omega}$ in an ambient rotational flow ($\boldsymbol{\omega}^\infty \times \boldsymbol{x}$) is given by,

$$\mathbf{T}^h = 8\pi\mu a^3 [\boldsymbol{\omega}^\infty(\boldsymbol{x} = 0) - \boldsymbol{\omega}] \tag{C.34}$$

Here we have compared the hydrodynamic torque T_h on a particle rotating for varying omega $\boldsymbol{\omega} = \Omega\mathbf{e}_z$ and size of the sphere a. The black circles in the plot figure C.7 (a) and (b) are obtained from boundary integral method whereas the red stars are from the analytical expression given by equation C.34. Both the methods shows excellent agreement with each other and the error decays with increase in number of elements ($\sim N_{elm}^{-2}$). The

second problem is more involved and the analytical solution of the Stokes equation in the presence of a sphere S is formally derived using method of images, and can be referred from [133].
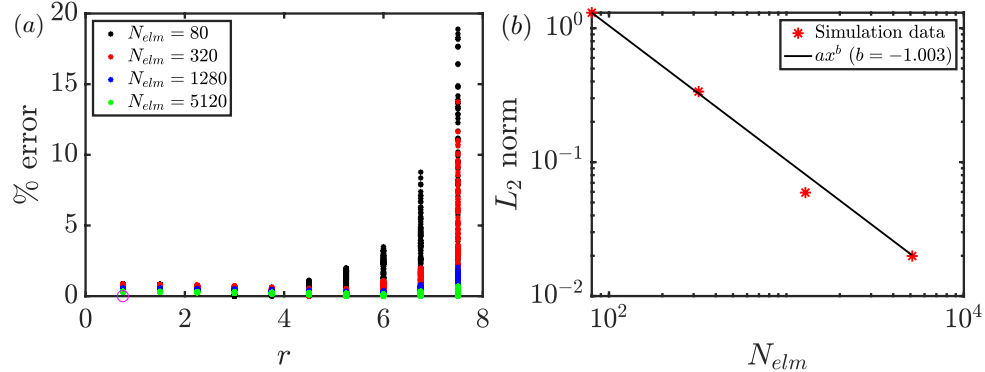
Figure C.9: Quantitative error analysis of the boundary integral method and it's comparison with the analytical green's functions solution. (a) shows the % error for the induced velocity at different radial positions inside a sphere $(R_s = 8.0)$ for a point force located on the x axis at $r = 1$ with varying surface elements. For $N_{elm} = 5120$, the error is well below $1 - 2\%$ which shows the power of boundary computational method in representing the flow fields. (b) represents the scaling of L2 norm of the induced velocity with number of elements on the surface $(\sim N_{elm})$ on a log-log plot.

Figure C.8 shows the flow field induced by a point force located on the x axis in a plane passing through of the center of the sphere. A good qualitative comparison between flow field obtained from the boundary integral method (a) and using the analytical Green's function (b) can be seen. Next, we can make it a bit more quantitatively by calculating the % error between the two methods. Figure C.9 $(a), (b)$ shows the convergence of the error by characterizing the L2 norm with varying number of elements on the surface, and it decays as $(\sim N_{elm})$ on a log-log plot.

C.7 Fast multiple methods: benchmark and scaling

The Fast Multipole Method (FMM) was introduced to solve a large N-body problem which can arise from discretization of boundary integral representation as in the present problem and has gained attention due to its $O(N)$ complexity, efficient arithmetic intensity in implementation [134], and better scalability compared to competing methods like FFT in performing the N-body sum. Let's see the idea of FMM on an N-body problem with a set of N source and target points. For each source point with a known position $\boldsymbol{x}_{0j} \in \mathbf{R}^3$ and source density $\boldsymbol{f}_j$, we have a target point with known position $(\boldsymbol{x}_i)$ and unknown potential $\boldsymbol{u}_i$ such that they are related to each other by,

$$\boldsymbol{u}_i = \sum_{j=1}^{N} \mathbf{G}(\boldsymbol{x}_i; \boldsymbol{x}_{0j}) \boldsymbol{f}(\boldsymbol{x}_{0j}), \tag{C.35}$$

where $\mathbf{G}$ is called the kernel function. To solve this problem, we first need to partition the domain using a tree data structure. The potential is evaluated at all the target points by computing the interactions from all other tree nodes. In FMM, the interactions are divided into two parts, near interactions which are computed exactly through direct summation using matrix vector multiplication by adding contributions from each source point, and far interactions corresponds to the contributions coming from the tree nodes far away from a target point. The interactions from source points in a well separated tree node are low rank and can be approximated using multipole expansion [135–138]. Here, we have presented some of the scaling and benchmarks data performed on a workstation and super computer (*Comet*) under XSEDE research allocation program. The simulation results are part of chapter 4 for fiber composed of beads in a confining ellipsoid of equivalent radius $R_s = 28.0$.

Table C.1: Table listing the numerical values of the dimensional parameters used in the simulations for benchmarking. The parameters are defined in Chapter 4.

Parameters	Values
N	1305/chain ($N_c = 23$)
R_s	28
$e = b/c$	1.25
$F_0/\sqrt{k_B T H_c}$	50
k_{on}/k_{off}	2/5
b	$\sqrt{3}$
Δt	5×10^{-6}

To reach a statistical steady state, it takes close to 120 hours (~ 5 days or total simulation time of ~ 30) plus another 2 days for ensemble averaging on a single node with 8 cores using a time step of $\Delta t = 5 \times 10^{-6}$ to have sufficient data to perform an ensemble average. Other simulation parameters are given in the table C.1. A simple calculation would give us the constraint on the maximum time step that can be used. The length scale (ℓ_c) is based on the minimum distance between the two beads given by the cut off distance a in the repulsive excluded volume forces and the corresponding velocity scale is governed by the magnitude of active forcing $\sim O(\sigma_0)$, which gives us the maximum time step $\Delta t_m = a/\sigma_0 = 6 \times 10^{-3}$. Distributed and shared memory parallelization in fast multipole methods is achieved on most platforms using OpenMP and MPI respectively. The limits of parallel scalability is clearly restricted by the serial part of the code most of which is developed in-house. A conservative estimate for good efficiency on recent platforms such as the *Comet* machine at SDSC is shown in Fig. C.10(*a*) which presents a fairly good picture on the speed up of our semi parallel code compared to the fully serial code. By semi-parallel, it means that the evaluation of the induced velocity $\boldsymbol{u}$ (see Chap 4) is completely parallel which make use of the ideas of the Kernel independent fast multipole expansion detailed above, whereas, the rest of the code involving time stepping, evaluation of the position dependent external forces etc. are in serial. We have tested the optimal

distribution of cores for a single run, and found that a single node with 8 cores offered the best trade-off for efficiency and resource usage as can be seen in Fig. C.10(b).
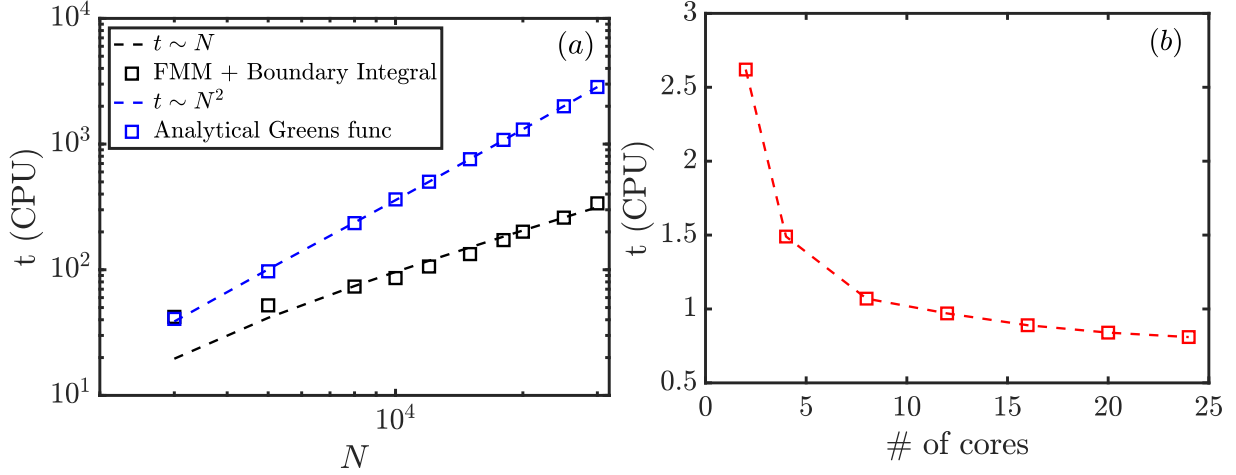

Figure C.10: (a) Benchmark data showing the comparison of the CPU time with number of beads (N) for 1000 time steps. The $O(N)$ scaling is very well known in the literature for the FMM compared to the $O(N^2)$ computation time scaling using in the classical matrix-vector multiplication, and (b) represents the comparison of CPU (time) with number of cores on a single node per single time step.

It is also necessary to leave a few available cores to avoid wasting significant amount of computational resources on a semi-parallel code. The most time consuming part in the code is the evaluation of the induced velocity by the external forcing as mentioned. Consequently, our optimization efforts focused mainly on implementing it efficiently. The above plot in figure C.10 (a) shows the CPU time calculated per 1000 time steps using 8 cores on a single node *Comet* at SDSC by varying number of beads, and our algorithm performs exceptionally well $\sim O(N)$ compared to the traditional methods $\sim O(N^2)$. Figure C.10 (b) shows the comparison of CPU time per single time step with number of cores for a single simulation time step using the same parameter values, but a fixed particle number of $N = 30,000$. On an in-house 16-core parallel workstation, the above code takes around $8 - 10$ days to have enough data for statistical averaging, whereas on the comet super

computer, the same set of simulation run would take $5 - 7$ days depending on the job submission queue. Even though this is not a significant decrease in the run time, the advantage comes from the fact that multiple runs can be executed on a super computer compared to a single run on a workstation.

Bibliography

[1] Nature, "The next 20 years of human genomics must be more equitable and more open," *Nature*, 2021.

[2] K. Roberts, B. Alberts, A. Johnson, P. Walter, and T. Hunt, "Molecular biology of the cell," *New York: Garland Science*, vol. 32, no. 2, 2002.

[3] D. E. Handy, R. Castro, and J. Loscalzo, "Epigenetic modifications: basic mechanisms and role in cardiovascular disease," *Circulation*, vol. 123, no. 19, pp. 2145–2156, 2011.

[4] M. Di Pierro, B. Zhang, E. L. Aiden, P. G. Wolynes, and J. N. Onuchic, "Transferable model for chromosome architecture," *Proceedings of the National Academy of Sciences*, vol. 113, no. 43, pp. 12168–12173, 2016.

[5] Q. MacPherson, B. Beltran, and A. J. Spakowitz, "Bottom–up modeling of chromatin segregation due to epigenetic modifications," *Proceedings of the National Academy of Sciences*, vol. 115, no. 50, pp. 12739–12744, 2018.

[6] M. Falk, Y. Feodorova, N. Naumova, M. Imakaev, B. R. Lajoie, H. Leonhardt, B. Joffe, J. Dekker, G. Fudenberg, I. Solovei, and L. A. Mirny, "Heterochromatin drives compartmentalization of inverted and conventional nuclei," *Nature*, vol. 570, no. 7761, pp. 395–399, 2019.

[7] T. J. Lampo, A. S. Kennard, and A. J. Spakowitz, "Physical modeling of dynamic coupling between chromosomal loci," *Biophysical journal*, vol. 110, no. 2, pp. 338–347, 2016.

[8] E. F. Koslover, M. D. de la Rosa, and A. J. Spakowitz, "Crowding and hopping in a protein's diffusive transport on dna," *Journal of Physics A: Mathematical and Theoretical*, vol. 50, no. 7, p. 074005, 2017.

[9] D. Saintillan, M. J. Shelley, and A. Zidovska, "Extensile motor activity drives coherent motions in a model of interphase chromatin," *Proceedings of the National Academy of Sciences*, vol. 115, no. 45, pp. 11442–11447, 2018.

[10] T. Shinar, M. Mana, F. Piano, and M. J. Shelley, "A model of cytoplasmically driven microtubule-based motion in the single-celled caenorhabditis elegans embryo," *Proceedings of the National Academy of Sciences*, vol. 108, no. 26, pp. 10508–10513, 2011.

[11] M. J. Shelley, "The dynamics of microtubule/motor-protein assemblies in biology and physics," *Annual Review of Fluid Mechanics*, vol. 48, pp. 487–506, 2016.

[12] R. E. Goldstein, I. Tuval, and J.-W. van de Meent, "Microfluidics of cytoplasmic streaming and its implications for intracellular transport," *Proceedings of the National Academy of Sciences*, vol. 105, no. 10, pp. 3663–3667, 2008.

[13] P. K. Trong, J. Guck, and R. E. Goldstein, "Coupling of active motion and advection shapes intracellular cargo transport," *Physical review letters*, vol. 109, no. 2, p. 028104, 2012.

[14] R. Phillips, J. Kondev, J. Theriot, H. G. Garcia, and N. Orme, *Physical biology of the cell*. Garland Science, 2012.

[15] P. A. Wiggins, T. Van Der Heijden, F. Moreno-Herrero, A. Spakowitz, R. Phillips, J. Widom, C. Dekker, and P. C. Nelson, "High flexibility of dna on short length scales probed by atomic force microscopy," *Nature nanotechnology*, vol. 1, no. 2, pp. 137–141, 2006.

[16] R. D. Kornberg and L. Stryer, "Statistical distributions of nucleosomes: nonrandom locations by a stochastic mechanism," *Nucleic acids research*, vol. 16, no. 14, pp. 6677–6690, 1988.

[17] R. Padinhateeri and J. F. Marko, "Nucleosome positioning in a model of active chromatin remodeling enzymes," *Proceedings of the National Academy of Sciences*, vol. 108, no. 19, pp. 7799–7803, 2011.

[18] J. J. Parmar, J. F. Marko, and R. Padinhateeri, "Nucleosome positioning and kinetics near transcription-start-site barriers are controlled by interplay between active remodeling and dna sequence," *Nucleic acids research*, vol. 42, no. 1, pp. 128–136, 2014.

[19] E. Fussner, U. Djuric, M. Strauss, A. Hotta, C. Perez-Iratxeta, F. Lanner, F. J. Dilworth, J. Ellis, and D. P. Bazett-Jones, "Constitutive heterochromatin reorganization during somatic cell reprogramming," *The EMBO journal*, vol. 30, no. 9, pp. 1778–1789, 2011.

[20] J. C. Hansen, M. Connolly, C. J. McDonald, A. Pan, A. Pryamkova, K. Ray, E. Seidel, S. Tamura, R. Rogge, and K. Maeshima, "The 10-nm chromatin fiber and its relationship to interphase chromosome organization," *Biochemical Society Transactions*, vol. 46, no. 1, pp. 67–76, 2018.

[21] S. V. Razin and A. A. Gavrilov, "Chromatin without the 30-nm fiber: constrained disorder instead of hierarchical folding," *Epigenetics*, vol. 9, no. 5, pp. 653–657, 2014.

[22] H. D. Ou, S. Phan, T. J. Deerinck, A. Thor, M. H. Ellisman, and C. C. O'shea, "Chromemt: Visualizing 3d chromatin structure and compaction in interphase and mitotic cells," *Science*, vol. 357, no. 6349, 2017.

[23] T. Misteli, "The self-organizing genome: principles of genome architecture and function," *Cell*, 2020.

[24] J. R. Dixon, S. Selvaraj, F. Yue, A. Kim, Y. Li, Y. Shen, M. Hu, J. S. Liu, and B. Ren, "Topological domains in mammalian genomes identified by analysis of chromatin interactions," *Nature*, vol. 485, no. 7398, pp. 376–380, 2012.

[25] E. P. Nora, B. R. Lajoie, E. G. Schulz, L. Giorgetti, I. Okamoto, N. Servant, T. Piolot, N. L. Van Berkum, J. Meisig, J. Sedat, J. Gribnau, E. Barillot, N. Blüthgen, J. Dekker, and E. Heard, "Spatial partitioning of the regulatory landscape of the x-inactivation centre," *Nature*, vol. 485, no. 7398, pp. 381–385, 2012.

[26] S. S. Rao, M. H. Huntley, N. C. Durand, E. K. Stamenova, I. D. Bochkov, J. T. Robinson, A. L. Sanborn, I. Machol, A. D. Omer, E. S. Lander, and E. L. Aiden, "A 3d map of the human genome at kilobase resolution reveals principles of chromatin looping," *Cell*, vol. 159, no. 7, pp. 1665–1680, 2014.

[27] E. Alipour and J. F. Marko, "Self-organization of domain structures by dna-loop-extruding enzymes," *Nucleic acids research*, vol. 40, no. 22, pp. 11202–11212, 2012.

[28] G. Fudenberg, M. Imakaev, C. Lu, A. Goloborodko, N. Abdennur, and L. A. Mirny, "Formation of chromosomal domains by loop extrusion," *Cell reports*, vol. 15, no. 9, pp. 2038–2049, 2016.

[29] K. Nasmyth, "Disseminating the genome: joining, resolving, and separating sister chromatids during mitosis and meiosis," *Annual review of genetics*, vol. 35, no. 1, pp. 673–745, 2001.

[30] J. Nuebler, G. Fudenberg, M. Imakaev, N. Abdennur, and L. A. Mirny, "Chromatin organization by an interplay of loop extrusion and compartmental segregation," *Proceedings of the National Academy of Sciences*, vol. 115, no. 29, pp. E6697–E6706, 2018.

[31] A. L. Sanborn, S. S. P. Rao, S.-C. Huang, N. C. Durand, M. H. Huntley, A. I. Jewett, I. D. Bochkov, D. Chinnappan, A. Cutkosky, J. Li, K. P. Geeting, A. Gnirke, A. Melnikov, D. McKenna, E. K. Stamenova, E. S. Lander, and E. L. Aiden, "Chromatin extrusion explains key features of loop and domain formation in wild-type and engineered genomes," *Proceedings of the National Academy of Sciences*, vol. 112, no. 47, pp. E6456–E6465, 2015.

[32] C. Brackley, M. Pereira, J. Johnson, D. Michieletto, and D. Marenduzzo, "Predictive models for 3d chromosome organization: The transcription factor and diffusive loop extrusion models," *Modeling the 3D Conformation of Genomes*, pp. 97–114, 2019.

[33] D. Racko, F. Benedetti, J. Dorier, and A. Stasiak, "Transcription-induced supercoiling as the driving force of chromatin loop extrusion during formation of tads in interphase chromosomes," *Nucleic acids research*, vol. 46, no. 4, pp. 1648–1660, 2018.

[34] M. Ganji, I. A. Shaltiel, S. Bisht, E. Kim, A. Kalichava, C. H. Haering, and C. Dekker, "Real-time imaging of dna loop extrusion by condensin," *Science*, vol. 360, no. 6384, pp. 102–105, 2018.

[35] I. F. Davidson, B. Bauer, D. Goetz, W. Tang, G. Wutz, and J.-M. Peters, "Dna loop extrusion by human cohesin," *Science*, vol. 366, no. 6471, pp. 1338–1345, 2019.

[36] Y. Kim, Z. Shi, H. Zhang, I. J. Finkelstein, and H. Yu, "Human cohesin compacts dna by loop extrusion," *Science*, vol. 366, no. 6471, pp. 1345–1349, 2019.

[37] S. Golfier, T. Quail, H. Kimura, and J. Brugués, "Cohesin and condensin extrude dna loops in a cell cycle-dependent manner," *Elife*, vol. 9, p. e53885, 2020.

[38] I. F. Davidson, D. Goetz, M. P. Zaczek, M. I. Molodtsov, P. J. Huis in 't Veld, F. Weissmann, G. Litos, D. A. Cisneros, M. Ocampo-Hafalla, R. Ladurner, F. Uhlmann, A. Vaziri, and J.-M. Peters, "Rapid movement and transcriptional relocalization of human cohesin on dna," *The EMBO journal*, vol. 35, no. 24, pp. 2671–2685, 2016.

[39] A. S. Hansen, I. Pustova, C. Cattoglio, R. Tjian, and X. Darzacq, "Ctcf and cohesin regulate chromatin loop stability with distinct dynamics," *Elife*, vol. 6, p. e25776, 2017.

[40] D. G. Lupiáñez, K. Kraft, V. Heinrich, P. Krawitz, F. Brancati, E. Klopocki, D. Horn, H. Kayserili, J. M. Opitz, R. Laxova, F. Santos-Simarro, B. Gilbert-Dussardier, L. Wittler, M. Borschiwer, S. A. Haas, M. Osterwalder, M. Franke, B. Timmermann, J. Hecht, M. Spielmann, A. Visel, and S. Mundlos, "Disruptions of topological chromatin domains cause pathogenic rewiring of gene-enhancer interactions," *Cell*, vol. 161, no. 5, pp. 1012–1025, 2015.

[41] W. A. Flavahan, Y. Drier, B. B. Liau, S. M. Gillespie, A. S. Venteicher, A. O. Stemmer-Rachamimov, M. L. Suvà, and B. E. Bernstein, "Insulator dysfunction and oncogene activation in idh mutant gliomas," *Nature*, vol. 529, no. 7584, pp. 110–114, 2016.

[42] B. D. Pope, T. Ryba, V. Dileep, F. Yue, W. Wu, O. Denas, D. L. Vera, Y. Wang, R. S. Hansen, T. K. Canfield, R. E. Thurman, Y. Cheng, G. Gülsoy, J. H. Dennis, M. P. Snyder, J. A. Stamatoyannopoulos, J. Taylor, R. C. Hardison, T. Kahveci, B. Ren, and D. M. Gilbert, "Topologically associating domains are stable units of replication-timing regulation," *Nature*, vol. 515, no. 7527, pp. 402–405, 2014.

[43] I. Solovei, M. Kreysing, C. Lanctôt, S. Kösem, L. Peichl, T. Cremer, J. Guck, and B. Joffe, "Nuclear architecture of rod photoreceptor cells adapts to vision in mammalian evolution," *Cell*, vol. 137, no. 2, pp. 356–368, 2009.

[44] E. Lieberman-Aiden, N. L. van Berkum, L. Williams, M. Imakaev, T. Ragoczy, A. Telling, I. Amit, B. R. Lajoie, P. J. Sabo, M. O. Dorschner, R. Sandstrom, B. Bernstein, M. A. Bender, M. Groudine, A. Gnirke, J. Stamatoyannopoulos, L. A. Mirny, E. S. Lander, and J. Dekker, "Comprehensive mapping of long-range interactions reveals folding principles of the human genome," *science*, vol. 326, no. 5950, pp. 289–293, 2009.

[45] F. Zenk, Y. Zhan, P. Kos, E. Löser, N. Atinbayeva, M. Schächtle, G. Tiana, L. Giorgetti, and N. Iovino, "Hp1 drives de novo 3d genome reorganization in early drosophila embryos," *Nature*, vol. 593, no. 7858, pp. 289–293, 2021.

[46] D. Canzio, E. Y. Chang, S. Shankar, K. M. Kuchenbecker, M. D. Simon, H. D. Madhani, G. J. Narlikar, and B. Al-Sady, "Chromodomain-mediated oligomerization of hp1 suggests a nucleosome-bridging mechanism for heterochromatin assembly," *Molecular cell*, vol. 41, no. 1, pp. 67–81, 2011.

[47] P. J. Verschure, I. Van Der Kraan, W. De Leeuw, J. Van Der Vlag, A. E. Carpenter, A. S. Belmont, and R. Van Driel, "In vivo hp1 targeting causes large-scale chromatin condensation and enhanced histone lysine methylation," *Molecular and cellular biology*, vol. 25, no. 11, pp. 4552–4564, 2005.

[48] T. Cheutin, A. J. McNairn, T. Jenuwein, D. M. Gilbert, P. B. Singh, and T. Misteli, "Maintenance of stable heterochromatin domains by dynamic hp1 binding," *Science*, vol. 299, no. 5607, pp. 721–725, 2003.

[49] S. Machida, Y. Takizawa, M. Ishimaru, Y. Sugita, S. Sekine, J.-i. Nakayama, M. Wolf, and H. Kurumizaka, "Structural basis of heterochromatin formation by human hp1," *Molecular cell*, vol. 69, no. 3, pp. 385–397, 2018.

[50] A. G. Larson, D. Elnatan, M. M. Keenen, M. J. Trnka, J. B. Johnston, A. L. Burlingame, D. A. Agard, S. Redding, and G. J. Narlikar, "Liquid droplet formation by hp1α suggests a role for phase separation in heterochromatin," *Nature*, vol. 547, no. 7662, pp. 236–240, 2017.

[51] A. R. Strom, A. V. Emelyanov, M. Mir, D. V. Fyodorov, X. Darzacq, and G. H. Karpen, "Phase separation drives heterochromatin domain formation," *Nature*, vol. 547, no. 7662, pp. 241–245, 2017.

[52] Y. Feodorova, M. Falk, L. A. Mirny, and I. Solovei, "Viewing nuclear architecture through the eyes of nocturnal mammals," *Trends in cell biology*, vol. 30, no. 4, pp. 276–289, 2020.

[53] Q. MacPherson, B. Beltran, and A. J. Spakowitz, "Chromatin compaction leads to a preference for peripheral heterochromatin," *Biophys. J.*, vol. 118, pp. 1479–1488, 2020.

[54] T. Cremer and M. Cremer, "Chromosome territories," *Cold Spring Harbor perspectives in biology*, vol. 2, no. 3, p. a003889, 2010.

[55] A. Rosa and R. Everaers, "Structure and dynamics of interphase chromosomes," *PLoS computational biology*, vol. 4, no. 8, p. e1000153, 2008.

[56] A. Y. Grosberg, S. K. Nechaev, and E. I. Shakhnovich, "The role of topological constraints in the kinetics of collapse of macromolecules," *Journal de physique*, vol. 49, no. 12, pp. 2095–2100, 1988.

[57] E. Guazzelli and J. F. Morris, *A physical introduction to suspension dynamics*, vol. 45. Cambridge University Press, 2011.

[58] T. U. N. C. for Fluid Mechanics Films, "Low reynolds number flows," 1966. `http://web.mit.edu/hml/ncfmf.html`.

[59] S. Kim and S. J. Karrila, *Microhydrodynamics: principles and selected applications*. Courier Corporation, 2013.

[60] S. Bianco, A. M. Chiariello, M. Conte, A. Esposito, L. Fiorillo, F. Musella, and M. Nicodemi, "Computational approaches from polymer physics to investigate chromatin folding," *Current opinion in cell biology*, vol. 64, pp. 10–17, 2020.

[61] J. J. Parmar, M. Woringer, and C. Zimmer, "How the genome folds: the biophysics of four-dimensional chromatin organization," *Annual review of biophysics*, vol. 48, pp. 231–253, 2019.

[62] M. Doi and S. F. Edwards, *The theory of polymer dynamics*, vol. 73. oxford university press, 1988.

[63] M. Rubinstein and R. H. Colby, *Polymer physics*, vol. 23. Oxford university press New York, 2003.

[64] Y. Cui and C. Bustamante, "Pulling a single chromatin fiber reveals the forces that maintain its higher-order structure," *Proceedings of the National Academy of Sciences*, vol. 97, no. 1, pp. 127–132, 2000.

[65] J. Dekker, K. Rippe, M. Dekker, and N. Kleckner, "Capturing chromosome conformation," *science*, vol. 295, no. 5558, pp. 1306–1311, 2002.

[66] P.-G. De Gennes and P.-G. Gennes, *Scaling concepts in polymer physics*. Cornell university press, 1979.

[67] C. A. Brackey, D. Marenduzzo, and N. Gilbert, "Mechanistic modeling of chromatin folding to understand function," *Nature Methods*, vol. 17, no. 8, pp. 767–775, 2020.

[68] L. Giorgetti, R. Galupa, E. P. Nora, T. Piolot, F. Lam, J. Dekker, G. Tiana, and E. Heard, "Predictive polymer modeling reveals coupled fluctuations in chromosome conformation and transcription," *Cell*, vol. 157, no. 4, pp. 950–963, 2014.

[69] H. C. Öttinger, *Stochastic Processes in Polymeric Fluids*. Springer, 1996.

[70] S. A. Hollingsworth and R. O. Dror, "Molecular dynamics simulation for all," *Neuron*, vol. 99, no. 6, pp. 1129–1143, 2018.

[71] D. L. Ermak and J. A. McCammon, "Brownian dynamics with hydrodynamic interactions," *The Journal of chemical physics*, vol. 69, no. 4, pp. 1352–1360, 1978.

[72] R. G. Larson, "The rheology of dilute solutions of flexible polymers: Progress and problems," *Journal of Rheology*, vol. 49, no. 1, pp. 1–70, 2005.

[73] J. F. Marko and E. D. Siggia, "Stretching dna," *Macromolecules*, vol. 28, no. 26, pp. 8759–8770, 1995.

[74] P. S. Doyle, E. S. Shaqfeh, and A. P. Gast, "Dynamic simulation of freely draining flexible polymers in steady linear flows," *Journal of Fluid Mechanics*, vol. 334, pp. 251–291, 1997.

[75] J. S. Hur, E. S. Shaqfeh, and R. G. Larson, "Brownian dynamics simulations of single dna molecules in shear flow," *Journal of Rheology*, vol. 44, no. 4, pp. 713–742, 2000.

[76] A. Grosberg, Y. Rabin, S. Havlin, and A. Neer, "Crumpled globule model of the three-dimensional structure of dna," *EPL (Europhysics Letters)*, vol. 23, no. 5, p. 373, 1993.

[77] L. A. Mirny, "The fractal globule as a model of chromatin architecture in the cell," *Chromosome research*, vol. 19, no. 1, pp. 37–51, 2011.

[78] J. Smrek and A. Y. Grosberg, "Facilitated diffusion of proteins through crumpled fractal dna globules," *Physical Review E*, vol. 92, no. 1, p. 012702, 2015.

[79] F. Jin, Y. Li, J. R. Dixon, S. Selvaraj, Z. Ye, A. Y. Lee, C.-A. Yen, A. D. Schmitt, C. A. Espinoza, and B. Ren, "A high-resolution map of the three-dimensional chromatin interactome in human cells," *Nature*, vol. 503, no. 7475, pp. 290–294, 2013.

[80] E. H. Finn, G. Pegoraro, H. B. Brandao, A.-L. Valton, M. E. Oomen, J. Dekker, L. Mirny, and T. Misteli, "Extensive heterogeneity and intrinsic variation in spatial genome organization," *Cell*, vol. 176, no. 6, pp. 1502–1515, 2019.

[81] M. Barbieri, M. Chotalia, J. Fraser, L.-M. Lavitas, J. Dostie, A. Pombo, and M. Nicodemi, "Complexity of chromatin folding is captured by the strings and binders switch model," *Proceedings of the National Academy of Sciences*, vol. 109, no. 40, pp. 16173–16178, 2012.

[82] M. Nicodemi and A. Prisco, "Thermodynamic pathways to genome spatial organization in the cell nucleus," *Biophysical journal*, vol. 96, no. 6, pp. 2168–2177, 2009.

[83] C. Annunziatella, A. M. Chiariello, S. Bianco, and M. Nicodemi, "Polymer models of the hierarchical folding of the hox-b chromosomal locus," *Physical Review E*, vol. 94, no. 4, p. 042402, 2016.

[84] D. Michieletto, E. Orlandini, and D. Marenduzzo, "Polymer model with epigenetic recoloring reveals a pathway for the de novo establishment and 3d organization of chromatin domains," *Physical Review X*, vol. 6, no. 4, p. 041047, 2016.

[85] C. A. Brackley, S. Taylor, A. Papantonis, P. R. Cook, and D. Marenduzzo, "Nonspecific bridging-induced attraction drives clustering of dna-binding proteins and genome organization," *Proceedings of the National Academy of Sciences*, vol. 110, no. 38, pp. E3605–E3611, 2013.

[86] F. Erdel and K. Rippe, "Formation of chromatin subcompartments by phase separation," *Biophysical journal*, vol. 114, no. 10, pp. 2262–2270, 2018.

[87] C. A. Brackley, J. Johnson, S. Kelly, P. R. Cook, and D. Marenduzzo, "Simulated binding of transcription factors to active and inactive regions folds human chromosomes into loops, rosettes and topological domains," *Nucleic acids research*, vol. 44, no. 8, pp. 3503–3512, 2016.

[88] E. J. Banigan and L. A. Mirny, "Loop extrusion: theory meets single-molecule experiments," *Current opinion in cell biology*, vol. 64, pp. 124–138, 2020.

[89] N. Naumova, M. Imakaev, G. Fudenberg, Y. Zhan, B. R. Lajoie, L. A. Mirny, and J. Dekker, "Organization of the mitotic chromosome," *Science*, vol. 342, no. 6161, pp. 948–953, 2013.

[90] A. Goloborodko, J. F. Marko, and L. A. Mirny, "Chromosome compaction by active loop extrusion," *Biophys. J.*, vol. 110, no. 10, pp. 2162–2168, 2016.

[91] A. Goloborodko, M. V. Imakaev, J. F. Marko, and L. Mirny, "Compaction and segregation of sister chromatids via active loop extrusion," *Elife*, vol. 5, p. e14864, 2016.

[92] S. S. Rao, S.-C. Huang, B. Glenn St Hilaire, J. M. Engreitz, E. M. Perez, K.-R. Kieffer-Kwon, A. L. Sanborn, S. E. Johnstone, G. D. Bascom, I. D. Bochkov, X. Huang, M. S. Shamim, J. Shin, D. Turner, Z. Ye, A. D. Omer, J. T. Robinson, T. Schlick, B. E. Bernstein, R. Casellas, E. S. Lander, and E. L. Aiden, "Cohesin loss eliminates all loop domains," *Cell*, vol. 171, no. 2, pp. 305–320, 2017.

[93] W. Schwarzer, N. Abdennur, A. Goloborodko, A. Pekowska, G. Fudenberg, Y. Loe-Mie, N. A. Fonseca, W. Huber, C. H. Haering, L. Mirny, and F. Spitz, "Two independent modes of chromatin organization revealed by cohesin removal," *Nature*, vol. 551, no. 7678, pp. 51–56, 2017.

[94] A. B. Kolomeisky and M. E. Fisher, "Molecular motors: a theorist's perspective," *Annu. Rev. Phys. Chem.*, vol. 58, pp. 675–695, 2007.

[95] V. Schaller, C. Weber, C. Semmrich, E. Frey, and A. R. Bausch, "Polar patterns of driven filaments," *Nature*, vol. 467, no. 7311, pp. 73–77, 2010.

[96] T. Sanchez, D. Welch, D. Nicastro, and Z. Dogic, "Cilia-like beating of active microtubule bundles," *Science*, vol. 333, no. 6041, pp. 456–459, 2011.

[97] T. Sanchez, D. T. Chen, S. J. DeCamp, M. Heymann, and Z. Dogic, "Spontaneous motion in hierarchically assembled active matter," *Nature*, vol. 491, no. 7424, p. 431, 2012.

[98] D. Needleman and Z. Dogic, "Active matter at the interface between materials science and cell biology," *Nat. Rev. Mater.*, vol. 2, p. 17048, 2017.

[99] R. G. Winkler and G. Gompper, "The physics of active polymers and filaments," *J. Chem. Phys.*, vol. 153, p. 040901, 2020.

[100] X. Liao, P. K. Purohit, and A. Gopinath, "Extensions of the worm-like-chain model to tethered active filaments under tension," *J. Chem. Phys.*, vol. 153, p. 194901, 2020.

[101] A. Laskar and R. Adhikari, "Brownian microhydrodynamics of active filaments," *Soft Matter*, vol. 11, pp. 9073–9085, 2015.

[102] T. Eisenstecken, G. Gompper, and R. G. Winkler, "Conformational properties of active semiflexible polymers," *Polymers*, vol. 8, no. 8, 2016.

[103] A. Martín-Gómez, T. Eisenstecken, G. Gompper, and R. G. Winkler, "Active brownian filaments with hydrodynamic interactions: conformations and dynamics," *Soft Matter*, vol. 15, pp. 3957–3969, 2019.

[104] S. K. Anand and S. P. Singh, "Conformation and dynamics of a self-avoiding active flexible polymer," *Phys. Rev. E*, vol. 101, p. 030501, 2020.

[105] D. Osmanović, "Properties of rouse polymers with actively driven regions," *J. Chem. Phys.*, vol. 149, p. 164911, 2018.

[106] S. Put, T. Sakaue, and C. Vanderzande, "Active dynamics and spatially coherent motion in chromosomes subject to enzymatic force dipoles," *Phys. Rev. E*, vol. 99, p. 032421, 2019.

[107] K. Liu, A. E. Patteson, E. J. Banigan, and J. M. Schwarz, "Dynamic nuclear structure emerges from chromatin cross-links and motors," *Phys. Rev. Lett.*, vol. 126, p. 158101, 2021.

[108] S. Lim, A. Ferent, X. S. Wang, and C. S. Peskin, "Dynamics of a closed rod with twist and bend in fluid," *SIAM Journal on Scientific Computing*, vol. 31, no. 1, pp. 273–302, 2008.

[109] C. S. Peskin, "The immersed boundary method," *Acta numerica*, vol. 11, pp. 479–517, 2002.

[110] M. Somasi, B. Khomami, N. J. Woo, J. S. Hur, and E. S. Shaqfeh, "Brownian dynamics simulations of bead-rod and bead-spring chains: numerical algorithms and coarse-graining issues," *Journal of non-newtonian fluid mechanics*, vol. 108, no. 1-3, pp. 227–255, 2002.

[111] B. Delmotte, E. Climent, and F. Plouraboué, "A general formulation of bead models applied to flexible fibers and active filaments at low reynolds number," *Journal of Computational Physics*, vol. 286, pp. 14–37, 2015.

[112] R. Cortez, "The method of regularized stokeslets," *SIAM Journal on Scientific Computing*, vol. 23, no. 4, pp. 1204–1225, 2001.

[113] D. J. Smith, "A boundary element regularized stokeslet method applied to cilia-and flagella-driven flow," *Proceedings of the Royal Society A: Mathematical, Physical and Engineering Sciences*, vol. 465, no. 2112, pp. 3605–3626, 2009.

[114] E. L. Bouzarth and M. L. Minion, "Modeling slender bodies with the method of regularized stokeslets," *Journal of Computational Physics*, vol. 230, no. 10, pp. 3929–3947, 2011.

[115] G. Gompper, T. Ihle, D. Kroll, and R. Winkler, "Multi-particle collision dynamics: A particle-based mesoscale simulation approach to the hydrodynamics of complex fluids," in *Advanced computer simulation approaches for soft matter sciences III*, pp. 1–87, Springer, 2009.

[116] R. B. Bird, C. F. Curtiss, R. C. Armstrong, and O. Hassager, *Dynamics of polymeric liquids, volume 2: Kinetic theory*. Wiley, 1987.

[117] T. W. Liu, "Flexible polymer chain dynamics and rheological properties in steady flows," *The Journal of chemical physics*, vol. 90, no. 10, pp. 5826–5842, 1989.

[118] H. C. Öttinger, *Stochastic processes in polymeric fluids: tools and examples for developing simulation algorithms*. Springer Science & Business Media, 2012.

[119] T. Ando, E. Chow, Y. Saad, and J. Skolnick, "Krylov subspace methods for computing hydrodynamic interactions in Brownian dynamics simulations," *J. Chem. Phys.*, vol. 137, p. 064106, 2012.

[120] A. Zidovska, D. A. Weitz, and T. J. Mitchison, "Micron-scale coherence in interphase chromatin dynamics," *Proceedings of the National Academy of Sciences*, vol. 110, no. 39, pp. 15555–15560, 2013.

[121] R. Bruinsma, A. Y. Grosberg, Y. Rabin, and A. Zidovska, "Chromatin hydrodynamics," *Biophysical journal*, vol. 106, no. 9, pp. 1871–1881, 2014.

[122] M. Di Pierro, D. A. Potoyan, P. G. Wolynes, and J. N. Onuchic, "Anomalous diffusion, spatial coherence, and viscoelasticity from the energy landscape of human chromosomes," *Proceedings of the National Academy of Sciences*, vol. 115, no. 30, pp. 7753–7758, 2018.

[123] L. Liu, G. Shi, D. Thirumalai, and C. Hyeon, "Chain organization of human interphase chromosome determines the spatiotemporal dynamics of chromatin loci," *PLoS computational biology*, vol. 14, no. 12, p. e1006617, 2018.

[124] G. Shi, L. Liu, C. Hyeon, and D. Thirumalai, "Interphase human chromosome exhibits out of equilibrium glassy dynamics," *Nature communications*, vol. 9, no. 1, pp. 1–13, 2018.

[125] D. Saintillan and M. J. Shelley, "Instabilities and pattern formation in active particle suspensions: kinetic theory and continuum simulations," *Physical Review Letters*, vol. 100, no. 17, p. 178103, 2008.

[126] D. Saintillan and M. J. Shelley, "Instabilities, pattern formation, and mixing in active suspensions," *Physics of Fluids*, vol. 20, no. 12, p. 123304, 2008.

[127] T. Gao, M. D. Betterton, A.-S. Jhang, and M. J. Shelley, "Analytical structure, dynamics, and coarse graining of a kinetic model of an active fluid," *Physical Review Fluids*, vol. 2, no. 9, p. 093302, 2017.

[128] C. Pozrikidis, *Boundary Integral and Singularity Methods for Linearized Viscous Flow*. Cambridge University Press, 1992.

[129] C. Pozrikidis, *A practical guide to boundary element methods with the software library BEMLIB*. CRC Press, 2002.

[130] C. Pozrikidis and D. Jankowski, *Introduction to theoretical and computational fluid dynamics*, vol. 675. Oxford university press New York, 1997.

[131] L. Greengard and V. Rokhlin, "A fast algorithm for particle simulations," *Journal of computational physics*, vol. 73, no. 2, pp. 325–348, 1987.

[132] Y. Saad and M. H. Schultz, "Gmres: A generalized minimal residual algorithm for solving nonsymmetric linear systems," *SIAM Journal on scientific and statistical computing*, vol. 7, no. 3, pp. 856–869, 1986.

[133] C. Maul and S. Kim, "Image of a point force in a spherical container and its connection to the Lorentz reflection formula," *J. Eng. Math.*, vol. 30, pp. 119–130, 1996.

[134] R. Yokota, "An fmm based on dual tree traversal for many-core architectures," *Journal of Algorithms & Computational Technology*, vol. 7, no. 3, pp. 301–324, 2013.

[135] W. Yan and M. Shelley, "Flexibly imposing periodicity in kernel independent fmm: A multipole-to-local operator approach," *Journal of Computational Physics*, vol. 355, pp. 214–232, 2018.

[136] D. Malhotra and G. Biros, "PVFMM: A parallel kernel independent FMM for particle and volume potentials," *Commun. Comput. Phys.*, vol. 18, no. 3, pp. 808–830, 2015.

[137] L. Ying, G. Biros, and D. Zorin, "A kernel-independent adaptive fast multipole algorithm in two and three dimensions," *J. Comput. Phys.*, vol. 196, no. 2, pp. 591–626, 2004.

[138] W. Yan, E. Corona, D. Malhotra, S. Veerapaneni, and M. Shelley, "A scalable computational platform for particulate stokes suspensions," *Journal of Computational Physics*, vol. 416, p. 109524, 2020.

[139] I. H. Riedel-Kruse, A. Hilfinger, J. Howard, and F. Jülicher, "How molecular motors shape the flagellar beat," *HFSP J.*, vol. 1, pp. 102–208, 2007.

[140] B. Chakrabarti and D. Saintillan, "Spontaneous oscillations, beating patterns, and hydrodynamics of active microfilaments," *Phys. Rev. Fluids*, vol. 4, p. 043102, 2019.

[141] K. J. Verhey, N. Kaul, and V. Soppina, "Kinesin assembly and movement in cells," *Annu. Rev. Biophys.*, vol. 40, pp. 267–288, 2011.

[142] S. L. Reck-Peterson, W. B. Redwine, R. D. Vale, and A. P. Carter, "Conformational properties of active semiflexible polymers," *Nat. Rev. Mol. Cell Biol.*, vol. 19, pp. 382–398, 2018.

[143] R. Alonso-Matilla, S. Thiyagarajan, and B. O'Shaugh-nessy, "Sliding filament and fixed filament mechanisms contribute to ring tension in the cytokinetic contractile ring," *Cytoskeleton*, vol. 76, no. 11-12, pp. 611–625, 2019.

[144] C. Bächer, M. Bender, and S. Gekle, "Flow-accelerated platelet biogenesis is due to an elasto-hydrodynamic instability," *Proc. Natl. Acad. Sci. USA*, vol. 117, p. 18969–18976, 2020.

[145] S. Ganguly, L. S. Williams, I. M. Palacios, and R. E. Goldstein, "Cytoplasmic streaming in drosophila oocytes varies with kinesin activity and correlates with the microtubule cytoskeleton architecture," *Proc. Natl. Acad. Sci. USA*, vol. 109, pp. 15109–15114, 2012.

[146] D. B. Stein, G. De Canio, E. Lauga, M. J. Shelley, and R. E. Goldstein, "Swirling instability of the microtubule cytoskeleton," *Proc. Natl. Acad. Sci. USA*, vol. 126, p. 028103, 2021.

[147] P. G. De Gennes, "Coil-stretch transition of dilute flexible polymers under ultrahigh velocity gradients," *J. Chem. Phys.*, vol. 60, p. 5030, 1974.

[148] E. F. Koslover and A. J. Spakowitz, "Discretizing elastic chains for coarse-grained polymer models," *Soft Matter*, vol. 9, no. 29, pp. 7016–7027, 2013.

[149] O. Hassager, "Kinetic theory and rheology of bead-rod models for macromolecular solutions. I. Equilibrium and steady flow properties," *J. Chem. Phys.*, vol. 60, p. 2111, 1974.

[150] R. B. Bird, C. F. C. Curtiss, R. C. Armstrong, and O. Hassager, *Dynamics of Polymeric Liquids. Volume II. Kinetic Theory.* Wiley, 1987.

[151] E. Plan and D. Vincenzi, "Tumbling of a Brownian particle in an extensional flow," *Proc. R. Soc. A*, vol. 472, p. 20160226, 2016.

[152] C. M. Schroeder, H. P. Babcock, E. S. G. Shaqfeh, and S. Chu, "Observation of polymer conformation hysteresis in extensional flow," *Science*, vol. 301, pp. 1515–1519, 2003.

[153] C.-C. Hsieh and R. G. Larson, "Prediction of coil-stretch hysteresis for dilute polystyrene molecules in extensional flow," *J. Rheol.*, vol. 49, p. 1081, 2005.

[154] W. F. Paxton, P. T. Baker, T. R. Kline, Y. Wang, T. E. Mallouk, and A. Sen, "Catalytically induced electrokinetics for motors and micropumps," *J. Am. Chem. Soc.*, vol. 128, pp. 14881–14888, 2006.

[155] Q. Brosseau, F. Balboa Usabiaga, E. Lushi, Y. Wu, L. Ristroph, J. Zhang, M. Ward, and M. J. Shelley, "Relating rheotaxis and hydrodynamic actuation using asymmetric gold-platinum phoretic rods," *Phys. Rev. Lett.*, vol. 123, p. 178004, 2019.

[156] J. Xu, H. Ma, J. Jin, S. Uttam, R. Fu, Y. Huang, and Y. Liu, "Super-resolution imaging of higher-order chromatin structures at different epigenomic states in single mammalian cells," *Cell Rep.*, vol. 24, no. 4, pp. 873–882, 2018.

[157] D. Amiad-Pavlov, D. Lorber, G. Bajpai, A. Reuveny, F. Roncato, R. Alon, S. Safran, and T. Volk, "Live imaging of chromatin distribution reveals novel principles of nuclear architecture and chromatin compartmentalization," *Sci. Adv.*, vol. 7, no. 23, p. eabf6251, 2021.

[158] D. Saintillan and M. Shelley, "Instabilities and pattern formation in active particle suspensions: Kinetic theory and continuum simulations," *Phys. Rev. Lett.*, vol. 100, p. 178103, 2008.

[159] D. Saintillan and M. J. Shelley, "Instabilities, pattern formation, and mixing in active suspensions," *Phys. Fluids*, vol. 20, p. 123304, 2008.

[160] T. Gao, M. Betterton, A. Jhang, and M. Shelley, "Analytical structure, dynamics, and reduction of a kinetic model of an active fluid," *Phys. Rev. Fluids*, vol. 2, p. 093302, 2017.

[161] A. R. Strom, R. J. Biggs, E. J. Banigan, X. Wang, K. Chiu, C. Herman, J. Collado, F. Yue, J. C. R. Politz, L. J. Tait, D. Scalzo, A. Telling, M. Groudine, C. P. Brangwynne, J. F. Marko, and A. D. Stephens, "HP1α is a chromatin crosslinker that controls nuclear and mitotic chromosome mechanics," *eLife*, vol. 10, p. e63972, 2021.

[162] A. Doostmohammadi, J. Ignés-Mullol, J. M. Yeomans, and F. Sagués, "Active nematics," *Nat. Commun.*, vol. 9, p. 3246, 2018.

[163] Y. Hatwalne, S. Ramaswamy, M. Rao, and R. Aditi Simha, "Rheology of active-particle suspensions," *Phys. Rev. Lett.*, vol. 92, p. 118101, 2004.

[164] D. Saintillan, "Rheology of active fluids," *Annu. Rev. Fluid Mech.*, vol. 50, pp. 563–592, 2018.

[165] J. H. Irving and J. G. Kirkwood, "The statistical mechanical theory of transport processes. IV. The equations of hydrodynamics," *J. Chem. Phys.*, vol. 18, p. 817, 1950.

[166] G. Fudenberg, N. Abdennur, M. Imakaev, A. Golobo-rodko, and L. A. Mirny, "Emerging evidence of chromosome folding by loop extrusion," *Cold Spring Harb. Symp. Quant. Biol.*, vol. 82, pp. 45–55, 2017.

[167] L. A. Mirny, M. Imakaev, and N. Abdennur, "Two major mechanisms of chromosome organization," *Curr. Opin. Cell Biol.*, vol. 58, pp. 142–152, 2019.

[168] H. B. Brandão, Z. Ren, X. Karaboja, L. A. Mirny, and X. Wang, "DNA-loop extruding SMC complexes can traverse one another in vivo," *Nat. Struct. Mol. Biol.*, vol. 28, pp. 642–651, 2021.

[169] J. M. Eeftens, S. Bisht, J. Kerssemakers, M. Kschonsak, C. H. Haering, and C. Dekker, "Real-time detection of condensin-driven dna compaction reveals a multistep binding mechanism," *The EMBO journal*, vol. 36, no. 23, pp. 3448–3457, 2017.

[170] T. Terakawa, S. Bisht, J. M. Eeftens, C. Dekker, C. H. Haering, and E. C. Greene, "The condensin complex is a mechanochemical motor that translocates along dna," *Science*, vol. 358, no. 6363, pp. 672–676, 2017.

[171] S. Golfier, T. Quail, H. Kimura, and J. Brugués, "Cohesin and condensin extrude loops in a cell-cycle dependent manner," *bioRxiv*, p. 821306, 2019.

[172] E. Kim, J. Kerssemakers, I. A. Shaltiel, C. H. Haering, and C. Dekker, "Dna-loop extruding condensin complexes can traverse one another," *Nature*, vol. 579, no. 7799, pp. 438–442, 2020.

[173] J.-K. Ryu, A. J. Katan, E. O. van der Sluis, T. Wisse, R. de Groot, C. Hearing, and C. Dekker, "Afm images of open and collapsed states of yeast condensin suggest a scrunching model for dna loop extrusion," *bioRxiv*, 2019.

[174] A. Riggs, "Dna methylation and late replication probably aid cell memory, and type i dna reeling could aid chromosome folding and enhancer function," *Philosophical Transactions of the Royal Society of London. B, Biological Sciences*, vol. 326, no. 1235, pp. 285–297, 1990.

[175] C. M. Schroeder, E. S. Shaqfeh, and S. Chu, "Effect of hydrodynamic interactions on dna dynamics in extensional flow: Simulation and single molecule experiment," *Macromolecules*, vol. 37, no. 24, pp. 9242–9256, 2004.

[176] R. M. Jendrejack, J. J. de Pablo, and M. D. Graham, "Stochastic simulations of dna in flow: Dynamics and the effects of hydrodynamic interactions," *The Journal of chemical physics*, vol. 116, no. 17, pp. 7752–7759, 2002.

[177] C. M. Schroeder, R. E. Teixeira, E. S. Shaqfeh, and S. Chu, "Dynamics of dna in the flow-gradient plane of steady shear flow: Observations and simulations," *Macromolecules*, vol. 38, no. 5, pp. 1967–1978, 2005.

[178] R. M. Jendrejack, D. C. Schwartz, J. J. De Pablo, and M. D. Graham, "Shear-induced migration in flowing polymer solutions: Simulation of long-chain dna in microchannels," *The Journal of chemical physics*, vol. 120, no. 5, pp. 2513–2529, 2004.

[179] T. Y. Lin, A. Saadat, A. Kushwaha, and E. S. Shaqfeh, "Effect of length on the dynamics of wall tethered polymers in shear flow," *Macromolecules*, vol. 51, no. 1, pp. 254–265, 2017.

[180] N. Hoda and S. Kumar, "Brownian dynamics simulations of polyelectrolyte adsorption in shear flow with hydrodynamic interaction," *The Journal of chemical physics*, vol. 127, no. 23, p. 234902, 2007.

[181] C.-C. Hsieh, L. Li, and R. G. Larson, "Modeling hydrodynamic interaction in brownian dynamics: simulations of extensional flows of dilute solutions of dna and polystyrene," *Journal of Non-Newtonian Fluid Mechanics*, vol. 113, no. 2-3, pp. 147–191, 2003.

[182] J. F. Marko and E. D. Siggia, "Bending and twisting elasticity of dna," *Macromolecules*, vol. 27, no. 4, pp. 981–988, 1994.

[183] E. J. Banigan and L. A. Mirny, "Limits of chromosome compaction by loop-extruding motors," *Physical Review X*, vol. 9, no. 3, p. 031007, 2019.

[184] B. van Steensel and A. S. Belmont, "Lamina-associated domains: Links with chromosome architecture, heterochromatin, and gene repression," *Cell*, vol. 169, pp. 780–191, 2017.

[185] A. Zidovska, "The rich inner life of the cell nucleus: dynamic organization, active flows, and emergent rheology," *Biophysical Reviews*, pp. 1–14, 2020.

[186] I. Eshghi, J. A. Eaton, and A. Zidovska, "Interphase chromatin undergoes a local sol-gel transition upon cell differentiation," *Phys. Rev. Lett.*, vol. 22, p. 228101, 2021.

[187] M. Theillard and D. Saintillan, "Computational mean-field modeling of confined active fluids," *J. Comp. Phys.*, vol. 397, p. 108841, 2019.

[188] M. P. Allen and D. J. Tildesley, *Computer Simulation of Liquids*. Oxford University Press, 1989.

[189] J. P. Hernández-Ortiz, J. J. de Pablo, and M. D. Graham, "Fast computation of many-particle hydrodynamic and electrostatic interactions in a confined geometry," *Phys. Rev. Lett.*, vol. 98, p. 140602, 2007.

[190] E. Nazockdast, A. Rahimian, D. Zorin, and M. Shelley, "A fast platform for simulating semi-flexible fiber suspensions applied to cell mechanics," *J. Comput. Phys.*, vol. 329, pp. 173–209, 2017.

[191] M. Fixman, "Construction of Langevin forces in the simulation of hydrodynamic interaction," *Macromolecules*, vol. 19, pp. 1204–1207, 1986.

[192] N. Sauerwald, S. Zhang, C. Kingsford, and I. Bahar, "Chromosomal dynamics predicted by an elastic network model explains genome-wide accessibility and long-range couplings," *Nucleic Acids Res.*, vol. 45, no. 7, pp. 3663–3673, 2017.